UNIVERSITÄT BASEL

Basel

Neutron- and neutrino-induced reactions: their physical description and influence on r-process calculations

Inauguraldissertation

zur Erlangung der Würde eines Doktors der Philosophie

vorgelegt der

Philosophisch-Naturwissenschaftlichen Fakultät
der Universität Basel

von

Darko Mocelj

aus Deutschland

Basel, 2006

Genehmigt von der Philosophisch-Naturwissenschaftlichen Fakultät
auf Antrag von
Prof. Dr. F.-K. Thielemann und Prof. Dr. T. Rauscher
(Mitglieder des Dissertationskomitees)

Basel, den 02. Mai 2006
(Datum der Fakultätssitzung)

Prof. Dr. Hans-Jakob Wirz
Dekan

To my parents

Contents

Chapter 1

Introduction

When I started this thesis my supervisors F. K. Thielemann and T. Rauscher spoke to me enthusiastically about the exciting and interesting field of nuclear astrophysics at our very first meeting. A field actually consisting of several branches of physics: thermodynamics, quantum mechanics, hydrodynamics, astrophysics, nuclear physics and numerics, just to mention some. During my thesis I had the opportunity to get deeper insights in nuclear physics, and astrophysics. Nuclear astrophysics and nuclear physics are inseparably connected. Astrophysical simulations, such as the modelling of supernova explosions or nucleosynthesis calculations, depend directly on nuclear physics information, like nuclear masses, half-lives, or nuclear reaction rates which can impose some constraints on the astrophysical parameter space. On the other side astrophysical simulations can provide constraints on nuclear models, such as the prediction of nuclear masses. Current accelerator facilities are able to provide this information for stable nuclei and for a broad range of neutron-rich nuclei. However, extremely neutron-rich nuclei still cannot be investigated due to their extremely small half-lives. Experimental information for these nuclei will be available at the earliest from the next generation of accelerators, which are currently under construction and will provide experimental information for such neutron-rich nuclei starting in a couple of years.

The first part of this thesis is dedicated to nuclear physics. The calculation of reaction rates which enter nucleosynthesis calculations in astrophysical simulations is an important ingredient. The way these rates are calculated depends, among other things, on the projectile energy and the mass region where the reaction takes place. For intermediate and heavy masses the reaction rate can be described by the so-called compound nucleus picture. In this model the the projectile and target nucleus form a compound state which de-excites by various particle evaporation modes. The compound nucleus picture describes the reaction mechanisms well if there are enough levels at the energy at which the compound nucleus is formed so that an average over individual resonances can

be performed. This model is called the Hauser Feshbach or statistical model. In the case of absence of the described levels at the formation energy, other reaction mechanisms have to be utilized to calculate the reaction rates, like direct reactions for example. The nuclear level density (NLD) is an important ingredient in the calculation of nuclear cross sections. In Chapter 2 the derivation of the NLD is reviewed. It will be shown that the NLD can be decomposed into three parts: a spin-, an excitation-energy-, and a parity dependent part. It will be assumed that the odd and even parity states are equally distributed. Chapter 3 is devoted to the calculation of the NLD - but this time without the assumption of equally distributed parities. An energy dependent parity-distribution function will be derived.

Nuclei heavier than iron are predominantly made by neutron-capture processes. The solar system abundance pattern of heavy nuclei indicates that two distinct neutron-capture processes occur in nature - one at low neutron density, called s-process, and one at high neutron density, called r-process. The r-process, or rapid neutron-capture process will be discussed in detail in the second part of my thesis. General aspects of nucleosynthesis calculations are reviewed in Chapter 4 including a discussion of the mathematical framework. A discussion of possible r-process sites, observational informations and astrophysical parameters are presented in Chapter 5. In Chapter 6 the focus will be set on the neutrino driven wind as a possible site for the production of elements heavier than iron. For the first time, neutrino-induced, neutron-induced, and beta-delayed fission are included simultaneously in a r-process nucleosynthesis calculation. Possible effects of all fission channels on the final abundance distribution and the discussion of the relevant nuclear physics are presented in Chapter 6, too. The thesis concludes with a short discussion of the results and an outlook on future improvements and investigations.

Chapter 2
Level Densities With Equal Parity Distribution

The nuclear level density is an important ingredient in the prediction of nuclear reaction rates calculated in the framework of a statistical model. Although the method as such is well approved, considerable effort has been put into the improvement of the nuclear input data. The nuclear level density also plays an important role in the determination of cross sections. Therefore, it is highly desirable to have an accurate description. There are several sophisticated theoretical approaches to describe the level density: Monte Carlo shell model calculations [DKL$^+$95],[ABLN00] , combinatorial approaches [Zuk01],[Isa02], combinations of both [ABF03] and many others. All these models have a serious drawback: For large scale astrophysical applications it is necessary to know the level density not only for one nucleus but usually for several thousand nuclei. Therefore, it is necessary to find a model describing the level density on one hand reliably and on the other hand computationally feasible. Such a model is the non interacting Fermi-gas model, which will be discussed in detail in this chapter.

2.1 The Level Density in the Independent Particle Model

Assuming rotational invariance of the nuclear Hamiltonian $\mathcal{H}$, all $(2J+1)$ states

$$|J \ -J\rangle, \ |J \ -J+1\rangle, \ \ldots, |J+J\rangle \ ,$$

differing only in the z-projection of the spin J, are degenerate in energy. As a consequence, the $(2J+1)$ levels cannot be distinguished experimentally by their energies. Therefore, the total level density ρ, for a nucleus with mass number A and energy E, is given by

$$\rho(A, E) = \sum_J \rho(A, E, J) \ , \tag{2.1}$$

where the sum goes over all J values per unit energy interval. Counting the actual number of states, the weighting factor $(2J + 1)$ has to be taken into account in the state density ω:

$$\omega(A, E) = \sum_J (2J + 1)\rho(A, E, J) \; . \tag{2.2}$$

To derive a relation between the level- and state density, we can compute the ratio of both

$$\frac{\omega(A, E)}{\rho(A, E)} = \frac{\sum_J (2J + 1)\rho(A, E, J)}{\sum_J \rho(A, E, J)} \equiv \langle 2J + 1 \rangle \; . \tag{2.3}$$

Equation (2.3) can be interpreted as an average value of the spin at a given energy. This average value is given by

$$\langle 2J + 1 \rangle = \sqrt{2\pi\sigma^2} \; , \tag{2.4}$$

where σ denotes the so-called spin cut-off factor, which will be discussed and derived in detail in section (2.1.2).
Combining equations (2.3) and (2.4) yields

$$\rho(A, E) = \frac{1}{\sqrt{2\pi\sigma^2}}\omega(A, E) \; , \tag{2.5}$$

which describes the relation between the level density ρ and the state density ω.

2.1.1   State density

The state density of a nucleus can be formally written as:

$$\omega(A, E) = \sum_k \sum_\nu \delta(A - A_\nu)\delta(E - \epsilon_k(A_\nu)) \; , \tag{2.6}$$

where ϵ_k denotes the energy of the single particle state k. Although this is an exact definition, the evaluation of the state density defined in this way remains an almost impossible task, as one has to know the full spectrum of energy eigenvalues for a given nucleus. However, an exact knowledge is not always required. If one is only interested in an average behavior, methods from statistical mechanics can be used.
In statistical mechanics the grand partition function

$$Z(\mu, T) = \sum_{n=0}^{\infty} \sum_k e^{(\mu n - \epsilon_k)/k_B T} \; , \tag{2.7}$$

is usually the starting point for calculating thermodynamical properties, where μ denotes the chemical potential, k_B Boltzmann's constant, T the temperature and

n the number of particles in the system. Temperature and chemical potential are only defined for macroscopic objects in equilibrium - on a nuclear scale they have no meaning. Therefore, they are replaced by two new parameters α and β:

$$Z(\alpha, \beta) = \sum_k \sum_\nu e^{\alpha A_\nu - \beta \epsilon_k(A_\nu)} \ . \tag{2.8}$$

The (nuclear) partition function can now be expressed in terms of ω as

$$Z(\alpha, \beta) = \int dE \int dA \, \omega(A, E) e^{\alpha A - \beta E} \ . \tag{2.9}$$

Having replaced the sum in (2.8) by an integral, now the state density can be evaluated by the inverse Laplace transform of the grand partition function

$$\omega(E, A) = \frac{1}{(2\pi i)^2} \int_{-i\infty}^{i\infty} \int_{-i\infty}^{i\infty} e^{\beta E - \alpha A + \ln Z(\alpha, \beta)} d\alpha d\beta \ . \tag{2.10}$$

The integration can be carried out using the so called saddle point approximation, described in Appendix [A], as the exponent of the integrand

$$S(\alpha, \beta) = \beta E - \alpha A + \ln Z(\alpha, \beta) \tag{2.11}$$

is a rapidly varying function of the integration parameters α and β. Application of this approximation (see (A.4)) yields

$$\omega(E, A) = \frac{e^{S(\alpha, \beta)}}{2\pi\sqrt{|D|}} \ . \tag{2.12}$$

In this approximation the state density has to be evaluated at the saddle point (α_0, β_0), which is defined by:

$$\frac{\partial S}{\partial \beta} = E + \frac{\partial \ln Z}{\partial \beta} = 0$$
$$\frac{\partial S}{\partial \alpha} = -A + \frac{\partial \ln Z}{\partial \alpha} = 0 \ .$$

The determinant of the matrix D in (2.12) is given by

$$\begin{vmatrix} \frac{\partial^2 \ln Z}{\partial \beta^2} & \frac{\partial \ln Z}{\partial \beta \partial \alpha} \\ \frac{\partial \ln Z}{\partial \alpha \partial \beta} & \frac{\partial^2 \ln Z}{\partial \alpha^2} \end{vmatrix} \ ,$$

once again evaluated at the saddle point (α_0, β_0).

So far, the derivation is general. To proceed further, a model of the nucleus is needed. In a first approximation the nucleus can be treated as an ensemble of

non-interacting particles moving in an average potential. In such a potential the occupancy of a single particle state k is denoted by f_k, where

$$f_k = \begin{cases} 1 & \text{if the state is occupied,} \\ 0 & \text{otherwise.} \end{cases}$$

In the independent particle model (IPM) the ground state of a nucleus is formed by filling all possible single particle states up to the Fermi energy ϵ_F. The nucleon number A and the ground state energy E_0 are given by

$$A = \sum_k f_k \tag{2.13}$$

$$E_0 = \sum_k \epsilon_k f_k \ . \tag{2.14}$$

Inserting both in (2.8) we arrive at

$$Z = \sum_{\{f_k\}} e^{\sum_k (\alpha_k - \beta_k \epsilon_k) f_k} \ , \tag{2.15}$$

where one has to sum over all possible configurations $\{f_k\}$. Further we get:

$$Z = \Pi_k (1 + e^{\alpha - \beta \epsilon_k}) \ . \tag{2.16}$$

By taking the logarithm on both sides, the product can be replaced by a sum.

$$\ln Z = \sum_k \ln(1 + e^{\alpha - \beta \epsilon_k}) \ . \tag{2.17}$$

Defining the single particle level density $g(\epsilon)$ by

$$g(\epsilon) = \sum_k \delta(\epsilon - \epsilon_k) \ , \tag{2.18}$$

we can write the partition function as

$$\ln Z = \int_0^\infty g(\epsilon) \ln(1 + e^{\alpha - \beta \epsilon_i}) d\epsilon \ . \tag{2.19}$$

Since the logarithmic factor in the integrand approaches zero very quickly for $\epsilon > \alpha/\beta$, the integral may be expanded in a Taylor series around α/β [BM69]:

$$\ln Z = \int_0^\infty g(\epsilon)(\alpha - \beta \epsilon) d\epsilon + \frac{\pi^2}{6\beta} g(\frac{\alpha}{\beta}) + \frac{7\pi^4}{360\beta^3} g''(\frac{\alpha}{\beta}) \dots \tag{2.20}$$

The contribution from the derivatives can be neglected, if one assumes a sufficiently constant single particle level density near the Fermi energy. This leads to:

$$\ln Z = \int_0^{\alpha/\beta} g(\epsilon)d\epsilon + \frac{\pi^2}{6\beta}g(\alpha/\beta) \ . \tag{2.21}$$

In the same way, the summation in (2.13) can be replaced by an integration:

$$A = \int_0^{\epsilon_F} g(\epsilon)d\epsilon \tag{2.22}$$

$$E_0 = \int_0^{\epsilon_F} \epsilon g(\epsilon)d\epsilon \ . \tag{2.23}$$

In statistical mechanics, the average energy E is defined by

$$E = -\frac{\partial \ln Z}{\partial \beta} \ . \tag{2.24}$$

By differentiating equation (2.21) with respect to β and evaluating the expression at the saddle point, the average energy E can be written as:

$$E = \int_0^{\alpha_0/\beta_0} \epsilon g(\epsilon)d\epsilon + \frac{\pi^2}{6\beta_0^2}g(\alpha_0/\beta_0) \ . \tag{2.25}$$

Comparing (2.23) with (2.25), one can identify the Fermi energy as

$$\epsilon_F = \alpha_0/\beta_0 \ .$$

Similarly, one may identify β_0 as the inverse temperature $1/kT$.
Using (2.25), the excitation energy E_x can be introduced in the form

$$E_x = E - E_0 = \frac{\pi^2}{6\beta_0}g(\alpha_0/\beta_0). \tag{2.26}$$

The value of Z and the determinant D in (2.12) can be expressed as functions of E_x. Substituting these results we can find the following expression for the state density:

$$\omega(A, E_x) = \frac{1}{E_x\sqrt{48}}e^{2\sqrt{aE_x}} \ , \tag{2.27}$$

where $a = \frac{\pi^2}{6}g(\epsilon_F)$ is the level density parameter.

Up to this point, only one sort of particles was taken into account. Moreover, two-body residual interactions between these particles have also been neglected. Performing this derivation with two sorts of particles, namely neutrons and protons, and with two-body correlations phenomenologically taken into account [GC65], the well known Bethe formula [Bet36] is recovered

$$\omega(E) = \frac{\sqrt{\pi}}{12a^{1/4}(E - \Delta)^{5/4}}e^{2\sqrt{a(E-\Delta)}} \ , \tag{2.28}$$

where both a and Δ are considered adjustable parameters to be determined from fits to experimental data.

Setting $U = E - \Delta$ and using (2.5), the total level density is given by

$$\rho(E) = \frac{1}{\sqrt{2\pi\sigma^2}} \frac{\sqrt{\pi}}{12 a^{1/4} U^{5/4}} e^{2\sqrt{aU}} \; . \tag{2.29}$$

2.1.2   Distribution of levels with different spin

Often, it is desirable to consider a level density which not only depends on the excitation energy but also on the intrinsic spin J. This dependence can be introduced as a multiplicative factor:

$$\rho(E, J) = \rho(E)\mathcal{F}(J) \; . \tag{2.30}$$

In the following we will derive an expression for $\mathcal{F}$.

For a given spin J, the possible values of the spin projection m range from $-J$ to J in integer steps. As a result the average m is zero. The distribution of the values of m can be taken to be a Gaussian function with mean value $\langle m \rangle = 0$ and variance σ, commonly called spin cut-off , see Figure 2.1.
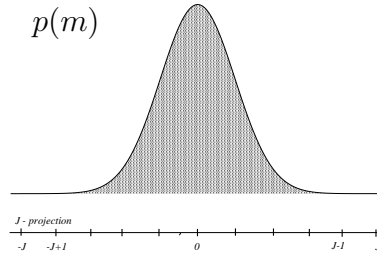
Figure 2.1: *Distribution of the spin-projection*

Thus, the distribution is given by

$$p(m) = \frac{1}{\sqrt{2\pi\sigma^2}} e^{-m^2/2\sigma^2} \; . \tag{2.31}$$

In the previous section we have seen that assuming rotational invariance single particle states with the same spin projection m cannot be distinguished and are therefore degenerate. In particular we can have a closer look at states having the spin projection $m = J$ and $m = J + 1$. The possible states fulfilling this requirement are:

$$m = J \qquad m = J + 1$$

$$|J \ J\rangle$$
$$|J + 1 \ J\rangle \quad |J + 1 \ J + 1\rangle$$
$$|J + 2 \ J\rangle \quad |J + 2 \ J + 1\rangle$$
$$|J + 3 \ J\rangle \quad |J + 3 \ J + 1\rangle$$
$$\cdots \qquad \cdots$$

By taking the difference of $p(m = J)$ and $p(m = J + 1)$, only states of different J will survive, as the others are degenerate and cancel each other.

With (2.31) we can obtain $\mathcal{F}(J)$, the distribution of states as a function of J:

$$\mathcal{F}(J) = p(m = J) - p(m = J + 1) , \tag{2.32}$$

$$\mathcal{F}(J) = \frac{1}{2\pi\sigma^2} \left(e^{-J^2/2\sigma^2} - e^{-(J+1)^2/2\sigma^2} \right) . \tag{2.33}$$

This expression can be approximated by rewriting the difference as a derivative

$$\mathcal{F}(J) \approx \frac{\partial p(m)}{\partial m}\Big|_{J+1/2} , \tag{2.34}$$

and finally

$$\mathcal{F}(J) = \frac{2J + 1}{2\sigma^2} e^{-J(J+1)/2\sigma^2} . \tag{2.35}$$

Knowing the spin distribution, we can calculate the average weighting factor introduced in section (2.1)

$$\langle 2J + 1 \rangle = \frac{\int_0^\infty dJ \mathcal{F}(J)(2J + 1)}{\int_0^\infty dJ \mathcal{F}(J)} . \tag{2.36}$$

Evaluating the integrals leads to the already known result

$$\langle 2J + 1 \rangle = \sqrt{2\pi\sigma^2} . \tag{2.37}$$

2.1.3 Distribution of levels with different parity

A convenient way to introduce parity dependence in the nuclear level density is to use another projection factor $\mathcal{P}(E)$ and writing

$$\rho(E, J, \pi) = \rho(E)\mathcal{F}(J)\mathcal{P}(E) , \tag{2.38}$$

where $\mathcal{P}(E)$ describes the contribution to the level density of single particle levels with either positive or negative parity states. The probability to occupy a single particle level with positive parity is denoted by p_+, to occupy one with a negative parity by p_-. It can be assumed that this distribution is Binomial. The probability to find k out of n nucleons in a negative parity state is therefore given by:

$$P(k) = \binom{n}{k} p_-^k (1 - p_-)^{n-k} \ . \tag{2.39}$$

Without loss of generality, we can assume that the total number of nucleons n is even. With this assumption, an odd number of nucleons in a negative parity state gives a negative parity state to the whole nucleus, an even number of nucleons in a negative parity state gives a positive parity state to the whole nucleus.

The total parity state of the nucleus is then given by:

$$P_-^n = \sum_{odd\,k} P(k) \ , \tag{2.40}$$

$$P_+^n = \sum_{even\,k} P(k) \ . \tag{2.41}$$

Evaluating (2.40) [GC65] yields

$$P_-^n = \frac{1 - (1 - 2p_-)^n}{2} \ . \tag{2.42}$$

If p_- is not very close to 1 or 0 and $n > 20$, $(1 - 2p_-)^n$ will be a very small number. As a consequence P_-^n will be close to $1/2$ and an equal distribution of positive and negative parity states can be assumed:

$$\mathcal{P}(E) = \frac{1}{2} \ ,$$

$$\rho(E, J, \pi) = \frac{1}{2} \rho(E) \mathcal{F}(J) \ . \tag{2.43}$$

2.1.4   Thermodynamical approach

Sometimes it is useful to express the nuclear level density by the entropy. In this section such a relation is derived. As before, the exact level density is given by a summation over the complete set of eigenvalues E_i of the nuclear Hamiltonian $\mathcal{H}$:

$$\rho(E) = \sum_i \delta(E - E_i) \tag{2.44}$$

We can express the partition function Z with help of the level density by:

$$Z = \int_0^\infty dE \rho(E) e^{-\beta E} . \tag{2.45}$$

The level density can be obtained from the partition function by an inverse Laplace transform:

$$\rho(E) = \frac{1}{2\pi i} \int_{-i\infty}^{+i\infty} d\beta Z(\beta) e^{\beta E} . \tag{2.46}$$

As the exponent of the integrand is a rapidly varying function, once more we can perform the saddle point approximation to evaluate the integral. The saddle point is given by the condition:

$$-\frac{\partial}{\partial \beta} \ln Z - E = 0 . \tag{2.47}$$

The integral can then be approximated by:

$$\rho(E) = \frac{e^S}{2\pi \frac{\partial^2 \ln Z}{\partial \beta^2}} , \tag{2.48}$$

where the entropy $S = \ln Z - \beta E$ has been introduced. The denominator of (2.48) is related to the specific heat by

$$\frac{\partial^2 \ln Z}{\partial \beta^2} = \beta^{-2} C . \tag{2.49}$$

Finally leading to

$$\rho(E) = \frac{e^S}{\sqrt{2\pi \beta^{-2} C}} . \tag{2.50}$$

2.2 Short Discussion of the Parameters

Combining the previously discussed dependencies on spin and parity, the total level density can be written as

$$\rho(U, J, \pi) = \frac{1}{2} \frac{1}{\sqrt{2\pi \sigma^2}} \frac{\sqrt{\pi}}{12 a^{1/4} U^{5/4}} e^{2\sqrt{aU}} \frac{(2J+1)}{2\sigma^2} e^{-J(J+1)/2\sigma^2} . \tag{2.51}$$

The parameter describing the level density are

σ^2, the spin cut-off factor,

a, the level density parameter and

U, the back-shifted excitation energy .

In the original derivation of Bethe [Bet36] nucleons were treated as an ensemble of noninteracting particles. However, this assumption is not correct. Especially near the ground state pairing effects are not negligible and have to be taken into account.

Both, protons and neutrons can be described by an independent particle model, after subtracting the energy which is necessary to break a pair from the excitation energy. This pairing energy is called Δ. Therefore, the parameter U in the level density is the excitation energy corrected for the pairing

$$U = E - \Delta \ ,$$

usually called the *back-shift*, with

$$
\begin{aligned}
\Delta_{even-even} &= \frac{12}{\sqrt{A}} \ , \\
\Delta_{odd} &= 0 \ , \\
\Delta_{odd-odd} &= -\frac{12}{\sqrt{A}} \ ,
\end{aligned}
$$

which can be derived from a nuclear mass droplet model.

The spin cut-off factor σ is given by [May94]:

$$\sigma^2 = \frac{\Theta_{rigid}}{\hbar^2}\sqrt{\frac{U}{a}} \quad \text{with} \quad \Theta_{rigid} = \frac{2}{5}m_u A R^2 \ .$$

The level density parameter a is a measure for the level spacing of the single particle levels. For a free Fermi Gas the ratio a/A is constant (A being the nuclear mass). From the nuclear structure point of view it is clear that the level spacings, and thus the level density parameter a, cannot be a constant. For nuclei with closed shells, the level spacing will decrease rapidly, therefore shell corrections $\mathcal{K}$ have also to be taken into account:

$$\frac{a}{A} = c_0 + c_1\mathcal{K}(N, Z) \ . \tag{2.52}$$

With increasing excitation energy this structure effects will be washed out. Such a damping was first introduced by [IIS79]. Taking this damping into account, the excitation-energy dependent level density parameter a can be described by:

$$a(U, Z, N) = \tilde{a}(A)[1 + c(Z, N)]\frac{f(U)}{U} \ , \tag{2.53}$$

where

$$\tilde{a}(A) = \alpha A + \beta A^{2/3} \tag{2.54}$$

and

$$f(U) = 1 - \exp(-\gamma U) \ . \tag{2.55}$$

The shape of the function $f(U)$ has been found by comparison to hydrodynamical calculations [IIS79]. The parameters α, β and γ are determined by fits to experimental data. Rauscher et. al [RTK97] have fitted the data for several thousand nuclei. Their data is the basis for the calculation of parity dependent nuclear level densities presented in chapter 3.

2.3 The Extension of the Level Density to Lower Excitation Energies

The back-shifted Fermi-gas diverges for $U \to 0$ MeV and thus cannot be applied to low excitation energies.
Cameron and Gilbert [GC65] have extracted a low energy dependence from low energy neutron scattering data. For low excitation energies, the data can be described by:

$$\rho_0(E) = \frac{1}{T} e^{\frac{E - E_M}{T}} \ , \tag{2.56}$$

which is called the constant temperature approximation. The parameter T is the nuclear temperature, and is defined by:

$$\frac{1}{T} = \frac{\partial \log \rho}{\partial U} \ .$$

The matching energy E_M separates the regimes in which either (2.56) or (2.51) are valid. The free parameter are determined by requiring that the level density and its first derivative are continuous at E_M.

Chapter 3
Parity-Projected Level Densities

In large scale calculations of the nuclear level density, so far an equal distribution of positive and negative parity states was assumed. This assumption is valid for high excitation energies but certainly not for low excitation energies, where the ground state parity dominates and the assumption of an equal distribution of positive and negative parity states is clearly violated. In this section we will derive an expression for the parity distribution as a function of the excitation energy. This distribution function will be used as a replacement for the factor $\mathcal{P}(E) = 1/2$ in the description of the nuclear level density. Its application is not limited to a level density of a back-shifted Fermi-gas type, the distribution of such can be applied to any available level density description.

3.1 The Big Picture

In the first part of this section, the underlying physical assumptions entering the derivation of the parity-projected level densities will be presented. Some of the details are left out from the discussion for the sake of readability. They will be discussed in full detail after the discussion of the general method itself.

The interacting shell-model is the most general approach to describe nuclear structure effects. Unfortunately, it requires the exact diagonalization of the shell-model Hamiltonian which, due to the exponential increase of the model space as a function of valence particles and orbitals, remains a computationally challenging task. Conventional diagonalization methods are presently limited to nuclei up to the Fe-region with nuclear masses around $A \approx 50$ [MZPC97],[NVL97]. The calculation of averaged properties of nuclei instead of absolute ones can shift the frontier towards heavier nuclei. By introducing auxiliary field Monte Carlo techniques [LJKO93], [ADK$^+$94], known as the Shell-model Monte Carlo Method (SMMC), calculations in much larger model spaces became feasible. The present limitation of SMMC calculations lies in the region of $A \approx 70$.
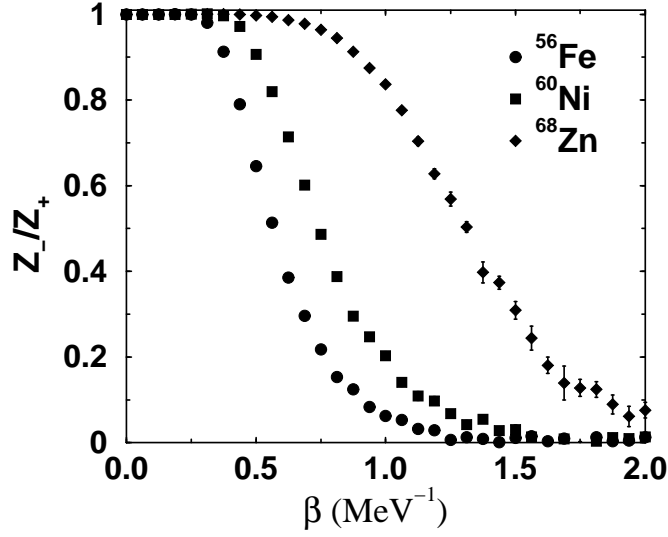
Figure 3.1: *Ratio of the odd- to even parity partition functions for ^{56}Fe, ^{60}Ni and ^{68}Zn as a function of the inverse temperature β [ABLN00].*

In the SMMC framework extensive studies of the nuclear level density were performed by Y. Alhassid and co-workers [ABLN00], covering the iron to germanium region using the complete $(pf + g_{g/2})$ shell. The basic goal of their work was to find a connection between the thermodynamic quantities such as the partition function and the underlying nuclear structure hidden in the calculation of occupation numbers of the individual single particle levels. By using so-called particle re-projection techniques [NA97], nuclear statistical properties of a nucleus could be calculated. Figure 3.1 shows the ratio of the odd- to even parity partition functions as a function of the inverse temperature β. Alhassid et. al. were able to describe this dependence by a simple phenomenological formula which reproduces well the exact SMMC calculations. If the assumption of equally distributed single particle parities is valid, the ratio of the partition functions would be unity, independently of the temperature. As expected, clearly this is not the case. The crossover from low temperatures, where one parity dominates, to higher temperatures where both parities are equal, can be described by a simple model, which will be explained in detail below.

Single particle levels are divided into two groups, according to their individual parities. The group which has the smaller average occupation number is denoted by π. Assuming that particles occupy the single-particle orbitals independently and randomly, the occupancy n of the π-parity orbits is given by a Poisson distribution,

$$P(n) = \frac{f^n}{n!}e^{-f} \,, \tag{3.1}$$

where f is the average occupancy of orbits with parity π. The physical meaning of f and the justification of the assumption of the Poisson distribution, will be discussed later. The ratio of the odd-parity to the even-parity probabilities is then given by

$$\frac{P_-}{P_+} = \frac{Z_-}{Z_+} = \tanh f \ . \tag{3.2}$$

In nuclei, f has to be replaced by the sum of individual contributions from neutrons and protons. The partition function Z is calculated in the spirit of a macroscopic-microscopic nuclear level density described in chapter 2.1. Using $Z_- + Z_+ = Z$ and equation (3.2), we can thus determine the positive and negative partition function individually:

$$Z_+ = \frac{1}{1 + \tanh f},$$
$$Z_- = \frac{1}{1 + \frac{1}{\tanh f}} \ .$$

Thermal energies E, heat capacities C and entropies S are derived from standard thermodynamic relations:

$$E = -\frac{\partial \ln Z}{\partial \beta}$$
$$C = -\beta^2 \frac{\partial^2 \ln Z}{\partial \beta^2}$$
$$S = \beta E + \ln Z.$$

The corresponding level density can be calculated by using the Laplace transform of the partition function, introduced in chapter 2.1.

Single particle levels are filled according to their energy, starting with the lowest energy level available, as long as there are enough particles to populate the remaining levels. After the distribution of the particles, the single particle levels are grouped according to their parity. Therefore the number of individual particles in each group will not be the same. Thus, for the same excitation energy E, the inverse temperature β, which appears in the description of the occupation numbers will be different for the two groups. The inverse temperatures are denoted by β^+ and β^-, respectively. Evaluating the integrals in the saddle point approximation (2.50), we obtain

$$\rho_\pm = \frac{1}{\sqrt{2\pi C^\pm}} \beta^\pm e^{\beta^\pm + \ln Z^\pm} \ , \tag{3.3}$$

and the ratio therefore by

$$\frac{\rho_-}{\rho_+} = \frac{\beta^-}{\beta^+} \frac{Z^-}{Z^+} \sqrt{\frac{C^+}{C^-}} e^{(\beta^- - \beta^+)E} \ . \tag{3.4}$$
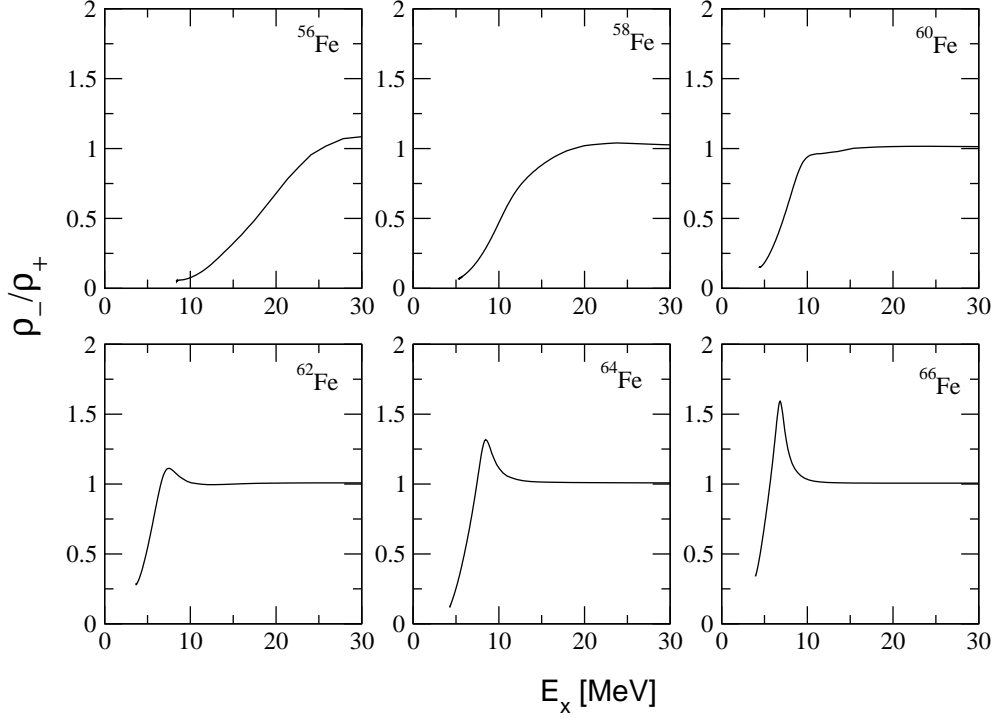
Figure 3.2: *Evolution of odd- to even-parity ratio within the Fe-chain.*

The evolution of the parity ratios within an isotopic chain is shown in figure (3.2). Starting with ^{56}Fe, where the neutron pf-shell is filled only to 50%, and stopping with ^{66}Fe, where the next major shell has started to be populated, one can see that the ratio approaches unity for lower values of the excitation energy as one approaches the $N = 40$ shell closure. As the parity can only be changed by excitations from the pf to the sdg shell, the ratio will equilibrate faster with increasing neutron number as the gap between the last occupied orbit in the pf-shell and the sdg-shell will decrease. For ^{66}Fe, where the pf shell is completely filled, a pronounced peak around 8 MeV shows up, which might be understood as follows: as the pf-shell is completely filled, the parity of the system will be changed by any neutron excitation, resulting in a dominance of negative parity states at the energies for which the peak appears. Such a behavior can be expected not only at the interface between the pf- and the sdg-shell, but everywhere where one major shell is completely filled and the next available shell to populate has the opposite parity.

3.2 The Tedious Details

3.2.1 Justifying the Poisson distribution

So far we have used the term 'parity' several times without defining it in a proper way - this will be done now.

Parity is a quantity that refers to the relationship between a mathematical object and its spatial mirror reflection. Let us consider a quantum mechanical system which can be described by a wave function $|\Psi\rangle$. The properties of such a system should not change under a parity transformation $\mathcal{P}$. Therefore the wavefunction of the system can only differ by an arbitrary constant π after performing the transformation:

$$\mathcal{P}|\Psi\rangle = \pi|\Psi\rangle.$$

A second parity transformation will bring the system back to its initial state:

$$\mathcal{P}^2|\Psi\rangle = \pi^2|\Psi\rangle = |\Psi\rangle.$$

By comparing both sides of the equation it immediately follows that the arbitrary constant, called *parity*, can only take two values: ± 1. In nuclear physics, single particle states can be characterized by a set of quantum mechanical observables, e.g.

$$|\Psi\rangle = |nlj\rangle,$$

where l and n denote the radial and the angular momentum quantum numbers respectively. The sum of the intrinsic spin and the angular momentum is given by j. The parity of such states is given by:

$$\mathcal{P}|nlj\rangle = (-1)^l|nlj\rangle. \tag{3.5}$$

So far we have discussed the parity only for a single particle. For an ensemble of k particles, the total parity of the system is given by the product of the individual parities:

$$\pi_{tot} = (-1)^{l_1}(-1)^{l_2}(-1)^{l_3}\ldots(-1)^{l_k}, \tag{3.6}$$

where l_i denotes the angular momentum of particle i. From equation (3.6) it is clear that the overall parity is always positive if k is even. It can be positive or negative if k is odd.

A typical level scheme for nuclei in the iron region is shown in Figure 3.3. The single particle levels are labeled in the so-called spectroscopic notation, where each character is a shortcut for an angular momentum l,

$$
\begin{array}{ccccc}
s & p & d & f & \ldots \\
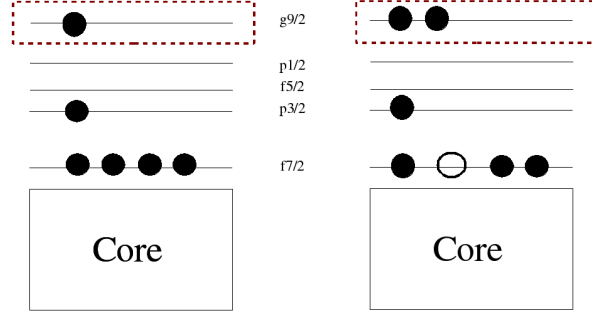0 & 1 & 2 & 3 & \ldots
\end{array}
$$

Figure 3.3: *Typical single particle level scheme for nuclei in the Fe-region.*

and the subscript represents the value of the total spin j. As an example, $f_{7/2}$ labels a single particle level with orbital momentum $l = 3$, hence the parity of this level is negative. The same is true for the remaining levels; as all of them have an odd orbital momentum, their parity is negative too. The set of levels mentioned so far is often called pf-shell. The remaining single particle level with label $g_{9/2}$ is the only one with a positive parity. The total parity of the system of six nucleons on the left hand side is given by

$$\pi_{tot} = \underbrace{(-1)^3 \times (-1)^1 \times (-1)^3 \times (-1)^1}_{pf-shell} \times \underbrace{(-1)^4}_{g_{9/2}}. \tag{3.7}$$

For large systems it is sometimes easier to avoid the determination of the individual parities. Instead one can take advantage of the multiplicative structure of the total parity and build two groups of single particle levels with parity $+1$, called π^+ and -1 called π^- respectively. The system shown in Figure 3.3 consists of an even number of particles. Therefore, the number of particles in the π^+ and in the π^- group both have to be either even or odd. Knowing the number of particles in one of the two groups is sufficient to know the total parity of the system. This can be understood as follows: If the number of particles in the π^+ group is odd, as on the left hand side of the picture, the number of particles in the π^- group is odd too. The parity of an odd number of particles with negative parity is negative. Similarly, if the number of particles in the π^+ group is even, the π^- group also contains an even number of particles, therefore the total parity is positive. By grouping levels with different parity into two distinct groups, one can avoid the multiplication of individual parities and simply count the number of particles in one of the groups instead. In principle it does not matter whether one counts the particles in the π^+ or in the π^- group, both yield the same results.

A single particle level can either be occupied or not - the probability distribution for the occupation of single particle levels can be assumed to be Binomial. The probability to occupy s out of r levels is therefore given by:

$$B(r; s) = \binom{r}{s} p^s (1-p)^{r-s}, \tag{3.8}$$

where the probability of occupying a level is denoted by p. If the number of levels r is large and the probability p is small, with the product rp finite, then the Poisson distribution $P(s)$ is a good approximation to the Binomial distribution. This can always be achieved by clustering the single particles into two groups according to their parity and counting only particles in the group having the opposite parity to the last occupied level. The probability to find s particles in the π^+ group in Figure 3.3 is then

$$P(s) = \frac{f^s}{s!} e^{-f}, \tag{3.9}$$

where the average number of particles in the group π^+ is given by f. For an even number of nucleons the probability to find the whole system in a positive parity state is therefore given by

$$P^+ = \sum_{s \in \pi_+}^{even} \frac{f^s}{s!} e^{-f} = \cosh f e^{-f}, \tag{3.10}$$

and to find the system in a negative parity state by

$$P^- = \sum_{s \in \pi_+}^{odd} \frac{f^s}{s!} e^{-f} = \sinh f e^{-f}. \tag{3.11}$$

The probabilities can be related to the total partition function by

$$P^+ = \frac{Z^+}{Z_{tot}}, \quad \text{and} \tag{3.12}$$

$$P^- = \frac{Z^-}{Z_{tot}}. \tag{3.13}$$

By taking the ratio of P^- to P^+ and substituting equations (3.10) and (3.11) into (3.12) and (3.13) we recover the known expression for the ratio of the negative to positive partition function:

$$\frac{Z^-}{Z^+} = \tanh f. \tag{3.14}$$

GS Parity	s.p. configuration	Parity of last occupied orbit	Configuration No.
+	(even,even)	$(+,+)$	1
		$(+,-)$	2
		$(-,+)$	3
		$(-,-)$	4
	(odd,odd)	$(+,+)$	5
		$(-,-)$	6
$-$	(odd,odd)	$(+,-)$	7
		$(-,+)$	8

Table 3.1: *Single Particle Configurations for an even A nucleus.*

So far we have only treated an even number of particles. If the total number of particles is odd, our equations derived so far still remain valid, we only have to take care of the correct counting of particles in the corresponding parity group. The generalized equations are:

Total number of particles is even: Total number of particles is odd:

$$P^+ = \begin{cases} \sum_{n\in\pi^+}^{even} \frac{f^n}{n!} e^{-f} & = \cosh f e^{-f} \\[2ex] \sum_{n\in\pi^-}^{even} \frac{f^n}{n!} e^{-f} & = \cosh f e^{-f} \end{cases} \qquad P^+ = \begin{cases} \sum_{n\in\pi^+}^{odd} \frac{f^n}{n!} e^{-f} & = \sinh f e^{-f} \\[2ex] \sum_{n\in\pi^-}^{even} \frac{f^n}{n!} e^{-f} & = \cosh f e^{-f} \end{cases}$$

$$P^- = \begin{cases} \sum_{n\in\pi^+}^{odd} \frac{f^n}{n!} e^{-f} & = \sinh f e^{-f} \\[2ex] \sum_{n\in\pi^-}^{odd} \frac{f^n}{n!} e^{-f} & = \sinh f e^{-f} \end{cases} \qquad P^- = \begin{cases} \sum_{n\in\pi^+}^{even} \frac{f^n}{n!} e^{-f} & = \cosh f e^{-f} \\[2ex] \sum_{n\in\pi^-}^{odd} \frac{f^n}{n!} e^{-f} & = \sinh f e^{-f} \end{cases}$$

Another important thing to be considered here, is the fact that nuclei consist of two sort of particles, namely protons and neutrons. The overall parity is then given by the product of the individual neutron and proton parities

$$\pi_{tot} = \pi_n \times \pi_p,$$

where π_n and π_p are calculated as described above.
Tables 3.1 and 3.2 show the all possible configurations for an even A and odd A nucleus. We will not discuss all possible configurations in detail. Instead we will consider two of them and show that equation (3.14), with some minor changes, is still valid. So far we have always evaluated the ratio P^- to P^+.

It is clear that expression (3.14) is incorrect for an odd A nucleus. As the ground state parity of the nucleus is negative the ratio P^-/P^+ should diverge for

GS Parity	s.p. configuration	Parity of last occupied orbit	Configuration No.
+	(even,odd)	(+,+)	9
		(−,+)	10
	(odd,even)	(+,+)	11
		(+,−)	12
−	(even,odd)	(+,−)	13
		(−,−)	14
	(odd,even)	(−,+)	15
		(−,−)	16

Table 3.2: *Single Particle Configurations for an odd A nucleus.*

small excitation energies. Figure (3.1) clearly shows that this is not the case. In such a situation we have to evaluate the ratio P^+/P^- to reproduce the $\tanh f$ dependency correctly. For simplicity, we will denote the ground state parity of the whole nucleus by π_g, the parity opposite to the ground state π_g by π_s. This way, we are independent of the actual configuration of the nucleus. Expression (3.14) remains valid for the ratio of P^s/P^g:

$$\frac{P^s}{P^g} = \tanh f. \tag{3.15}$$

Proof:

Consider configuration (1) from Table 3.1 for an even A nucleus. A many-particle even-parity state results if protons and neutrons have overall parities $(+,+)$ or $(−,−)$, respectively, i. e.

$$\begin{aligned} P^+ &= P_p^+ P_n^+ + P_p^- P_n^-, \\ &= e^{-f_n}\cosh f_n e^{-f_p}\cosh f_p + e^{-f_n}\sinh f_n e^{-f_p}\sinh f_p, \\ &= e^{-(f_n+f_p)}\cosh(f_n+f_p), \end{aligned}$$

where the average occupation number of protons and neutrons are given by f_n and f_p. A many-particle odd-parity state results if the overall parities are given by $(+,−)$ or $(−,+)$. The probability for an odd-parity state is given by

$$\begin{aligned} P^- &= P_p^+ P_n^+ + P_p^- P_n^-, \\ &= e^{-f_n}\cosh f_n e^{-f_p}\sinh f_p + e^{-f_n}\sinh f_n e^{-f_p}\cosh f_p, \\ &= e^{-(f_n+f_p)}\sinh(f_n+f_p). \end{aligned}$$

The ratio P^s/P^g can then be written as:

$$\frac{P^s}{P^g} = \frac{P^-}{P^+} = \tanh f,$$

where the occupation number f is the sum of f_n and f_p.

We can repeat the calculation for an odd-A nucleus. Let us consider configuration (15) from Table 3.2. The probability for an even-parity state is given by

$$
\begin{aligned}
P^+ &= e^{-f_n} \sinh f_n e^{-f_p} \cosh f_p + e^{-f_n} \cosh f_n e^{-f_p} \sinh f_p, \\
&= e^{-(f_n+f_p)} \sinh(f_n + f_p).
\end{aligned}
$$

The probability to find an odd-parity state is given by

$$
\begin{aligned}
P^- &= e^{-f_n} \sinh f_n e^{-f_p} \sinh f_p + e^{-f_n} \cosh f_n e^{-f_p} \cosh f_p, \\
&= e^{-(f_n+f_p)} \cosh(f_n + f_p).
\end{aligned}
$$

The ratio can again be expressed as

$$
\frac{P^s}{P^g} = \frac{P^+}{P^-} = \tanh f.
$$

Such a calculation can be performed for all configurations. All of them will reproduce equation (3.15).

3.2.2   Pairing effects

In the previous section we have shown that the number of particles in a set of levels with equal parity is Poisson distributed, with mean value f. Before one can calculate the parity-projected ratio, given by equation (3.15), the mean value has to be discussed.

   We have seen that particles are always counted in the parity group opposite to that of the last filled single particle level. In the most simple case, we can assume that the particles are Fermi-Dirac distributed, where the occupancy of each single particle level is given by

$$
f_k = \frac{1}{1 + e^{\beta(\epsilon_k - \mu)}} \ .
$$

The average number of particles is therefore defined by

$$
\langle n \rangle = \sum_k f_k, \tag{3.16}
$$

which can be used to identify the single particle levels which are occupied and those which are empty. By knowing how many particles one can distribute, and specifying the inverse temperature β, equation (3.16) can be used to determine the chemical potential μ of the system. In the independent particle picture the chemical potential indicates the position of the last occupied level: all levels below the chemical potential will be occupied, all levels above the chemical potential
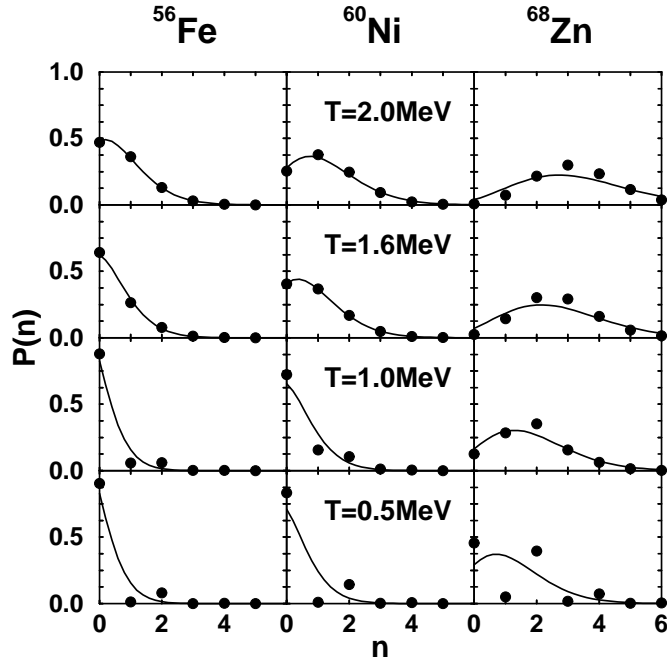
Figure 3.4: *Distribution $P(s)$ of the number of particles in the π_s group. The solid circles are SMMC results, solid lines represent Poisson distributions (3.9). [ABLN00]*

will be empty. Thus the parity of the last occupied single particle state can be determined. We can cluster the single particle levels into a group having the same parity as the last occupied sate, called π_g and in a group with parity opposite to π_g, called π_s. The mean value f in the Poisson distribution is then given by

$$f = \sum_{k \in \pi^s} f_k^{FD} = \sum_{k \in \pi^s} \frac{1}{1 + e^{\beta(\epsilon_k - \mu)}} \ . \tag{3.17}$$

With decreasing temperature pairing interactions will become more and more important, hence the Fermi-Dirac distribution will not be able to describe the occupation of single particle levels. In Figure 3.4 a comparison of the Poisson assumption with the results of a SMMC calculation is shown. At high temperatures the microscopic distributions are well described by the Poisson distribution but for lower temperatures deviations start to appear. Compared to the SMMC result, the probability to find an even number of particles in the π_s parity group is clearly enhanced, odd numbers of particles are suppressed. This is an indication that pairing effects should be taken into account. For low temperatures the mean occupation number f should be treated in the Bardeen, Cooper and Schrieffer (BCS) formalism [BCS57], see appendix [B.1] for details. In the BCS treatment, the occupation probabilities for condensed pairs are given by v_k^2 and

for quasi-particles by $f_k = 1/(1 + \exp(\beta E_k))$, where the quasi-particle energy E_k is given by $\sqrt{(\epsilon_k - \mu)^2 + \Delta^2}$. The chemical potential μ and the pairing gap Δ are determined for each temperature by solving the non-linear system of equations:

$$n = \frac{1}{2} \sum_k \left(1 - \frac{\epsilon_k - \mu}{E_k} \tanh\left(\frac{\beta}{2} E_k \right) \right) \tag{3.18}$$

$$\frac{2}{\Delta} = g_0 \sum_k \frac{\Delta}{E_k} \tanh\left(\frac{\beta}{2} E_k \right) .$$

For the calculation of the mean occupation in the π^s parity group, it is sufficient to consider only contributions from quasi-particles, as condensed pairs do not contribute to any parity change of the system. Equation (3.17) remains still valid, f_k has only to be replaced by the quasi-particle occupation number:

$$f = \sum_{k \in \pi^s} f_k^{BCS} = \sum_{k \in \pi^s} \frac{1}{1 + \exp(\beta E_k)} . \tag{3.19}$$

Numerical treatment of the BCS regime

In order to evaluate the occupation number f of the π^s parity-group, the chemical potential μ and the pairing gap Δ should be known as a function of β. The system of equations (3.18) can be solved by the Newton-Raphson method iteratively, until convergence is achieved:

$$\vec{x}_{new} = \vec{x}_{old} - \mathbf{J}^{-1} \vec{\Phi}, \tag{3.20}$$

with

$$\vec{x} = \begin{pmatrix} \mu \\ \Delta \end{pmatrix}, \quad \vec{\Phi} = \begin{pmatrix} \tilde{n} \\ \tilde{g} \end{pmatrix} \quad \text{and}$$

$$\mathbf{J} = \begin{pmatrix} \frac{\partial \tilde{g}}{\partial \mu} & \frac{\partial \tilde{g}}{\partial \Delta} \\ \frac{\partial \tilde{n}}{\partial \mu} & \frac{\partial \tilde{n}}{\partial \mu} \end{pmatrix} .$$

The guess value of the pairing gap Δ is extracted from odd-even mass differences [RT00], the guess for the chemical potential μ is determined by the solution of the $T = 0$ particle number equation:

In the temperature-independent case, the particle number equation is given by

$$n = \sum_k \left(1 - \frac{\epsilon_k - \mu}{E_k} \right) ,$$

which can be written as

$$\underbrace{\sum_k 1}_{=n_{level}} - \sum_k \epsilon_k / E_k + \sum_k \mu / E_k = n .$$

We can define

$$C_1 = n - n_{level} \ , \quad C_2 = \sum_k \epsilon_k / E_k \quad \text{and} \quad C_3 = \sum_k 1/E_k \ .$$

The chemical potential is then given by

$$\mu = \frac{C_1 + C_2}{C_3} \ , \tag{3.21}$$

which can be solved by iteration.

Numerical treatment of the Fermi regime

The chemical potential is once more the starting point of the calculation of the occupation number f. In the Fermi-Dirac regime, where pairing interaction can be neglected, the chemical potential is determined by the particle number equation

$$n = \sum_k \frac{1}{1 + e^{\beta(\epsilon_k - \mu)}} \ ,$$

or

$$\Phi(\mu) = \frac{1}{1 + e^{\beta(\epsilon_k - \mu)}} - n \ .$$

In order to solve this equation by an iterative procedure, we have to distinguish between two cases: the last occupied single particle level is either completely or partially filled. The two possible approaches are discussed now.

Partially filled Fermi-level

We can rewrite the particle number equation as:

$$\begin{aligned}
\Phi(\mu) &= \sum_k d_k \frac{1}{1 + e^{\beta(\epsilon_k - \lambda)}} - n \\
&= \sum_k d_k \frac{1}{1 + e^{\beta(\epsilon_k - \lambda)}} - \sum_k n_k \\
&= \sum_k d_k \left(\frac{1}{1 + e^{\beta(\epsilon_k - \lambda)}} - f_k \right) \ ,
\end{aligned}$$

where the fractional occupation of the single particle level ϵ_k is given by f_k, the degeneracy of the level by d_k. According to the relative position of the single particle levels to the Fermi level, the sum can be split into three parts:

$$\Phi(\mu) = \underbrace{\sum_{k=1}^{k_F - 1} d_k \left(\frac{1}{1 + e^{\beta(\epsilon_k - \lambda)}} - f_k \right)}_{A_1} + \underbrace{\sum_{k=k_F + 1}^{N} d_k \left(\frac{1}{1 + e^{\beta(\epsilon_k - \lambda)}} - f_k \right)}_{A_2} + d_{k_F} \left(\frac{1}{1 + e^{\beta(\epsilon_{k_F} - \mu)}} \right) \ ,$$

or

$$\Phi(\mu) = A_1 + A_2 + d_{k_F} \left(\frac{1}{1 + e^{\beta(\epsilon_{k_F} - \mu)}} \right) \ ,$$

respectively. The factors A_1 and A_2 can be written as

$$A_1 = \sum_{k=1}^{k_F - 1} d_k \left(\frac{1}{1 + e^{\beta(\epsilon_k - \lambda)}} - f_k \right) = - \sum_{k=1}^{k_F - 1} d_k e^{\beta(\epsilon_k - \mu)} \ ,$$

and

$$A_2 = \sum_{k=k_F + 1}^{N} d_k \left(\frac{1}{1 + e^{\beta(\epsilon_k - \lambda)}} - f_k \right) = \sum_{k=k_F + 1}^{N} d_k e^{-\beta(\epsilon_k - \mu)} \ .$$

The chemical potential is given by the root of $\Phi(\mu)$:

$$\Phi(\mu) = 0 \Rightarrow A_1 + A_2 + d_{k_F} \left(\frac{1}{1 + e^{\beta(\epsilon_{k_F} - \mu)}} \right) = 0.$$

This equation can be solved for the chemical potential:

$$\mu = \epsilon_{k_F} - \frac{1}{\beta} \ln \left(\frac{1}{f_{k_F} - (C_1 + C_2)} - 1 \right) \ . \tag{3.22}$$

One has to mention, that C_1 and C_2 intrinsically depend on the chemical potential μ. Therefore equation (3.22) has to be solved iteratively until the desired convergence tolerance has been achieved. A good starting value for μ is the single particle energy of the last filled level.

Completely filled Fermi-level

In principle the derivation proceeds along the same line as above, but taking into account that in the case of a completely filled Fermi-level $\mu \to \frac{\epsilon_{k_F} + \epsilon_{k_F+1}}{2}$ for $\beta \to \infty$. For low temperatures the chemical potential can be written in the following form:

$$\mu = \frac{\epsilon_{k_F} + \epsilon_{k_F+1}}{2} + \Delta\mu \ . \tag{3.23}$$

Again the starting point is

$$\Phi(\mu) = \sum_k d_k \frac{1}{1 + e^{\beta(\epsilon_k - \lambda)}} - n \ ,$$

which we can be rewritten as

$$\Phi(\mu) = - \sum_{k=1}^{k_F} d_k \frac{e^{\beta(\epsilon_k - \mu)}}{1 + e^{\beta(\epsilon_k - \mu)}} + \sum_{k=k_F + 1}^{N} d_k \frac{e^{-\beta(\epsilon_k - \mu)}}{1 + e^{-\beta(\epsilon_k - \mu)}}.$$

Using (3.23) for μ, we obtain

$$\Phi(\mu) = -e^{-\Delta\mu\beta} \underbrace{\sum_{k=1}^{k_F} d_k \frac{e^{\beta(\epsilon_k - \frac{\epsilon_{k_F} + \epsilon_{k_F+1}}{2})}}{1 + e^{\beta(\epsilon_k - \mu)}}}_{B_1} + e^{\Delta\mu\beta} \underbrace{\sum_{k=k_F+1}^{N} d_k \frac{e^{-\beta(\epsilon_k - \frac{\epsilon_{k_F} + \epsilon_{k_F+1}}{2})}}{1 + e^{-\beta(\epsilon_k - \mu)}}}_{B_2} \; ,$$

or

$$\Phi(\mu) = -e^{\Delta\mu\beta} B_1(\mu) + e^{\Delta\mu\beta} B_2(\mu) \; .$$

Again, the chemical potential is given by the root of the particle number equation:

$$\Phi(\mu) = 0 \Rightarrow e^{\Delta\mu\beta} B_1(\mu) = e^{\Delta\mu\beta} B_2(\mu) \; ,$$

and thus

$$\Delta\mu = \frac{1}{2\beta} \ln \frac{B_1}{B_2} \; . \tag{3.24}$$

Combining equations (3.23) and (3.24) yields

$$\mu = \frac{\epsilon_{k_F} + \epsilon_{k_F+1}}{2} + \frac{1}{2\beta} \ln \frac{B_1}{B_2} \tag{3.25}$$

which again intrinsically depends on the chemical potential.

Transition from the BCS- to the Fermi regime

So far we have discussed the low temperature regime, where pairing effects have to be taken into account and the high temperature regime, where the pairing effects are washed out, separately. The transition from one regime to the other is not trivial, as the temperature dependent pairing gap $\Delta(T)$ appearing in equations (3.18) cannot be calculated for temperatures above the critical temperature T_C. We could ignore this fact and simply connect the two regimes at $T = T_C$. In Figure 3.5 the result of such a calculation is shown. It should be noted that on the x-axis the inverse temperature β is plotted instead of the temperature T, as β is the independent variable in our calculations. By using β as the independent variable, the reader should be aware that the Fermi-regime is reached for small values of β, the BCS-regime is reached for large values of β.

As one can see, the transition from the Fermi-regime to the BCS-regime is not smooth. Due to the *kink* at the critical temperature β_C, the first and all higher derivatives of the occupation number f will not be continuous. As we will see, the derivatives of the occupation number are needed to calculate the parity-projected thermodynamical quantities. We have tried several strategies to smooth the transition from one regime to the other, e. g.

I) Spline interpolation of the occupation number in a region around the critical temperature. This produced some artificial over-shootings in the ratio of odd to even level densities and was therefore abandoned.
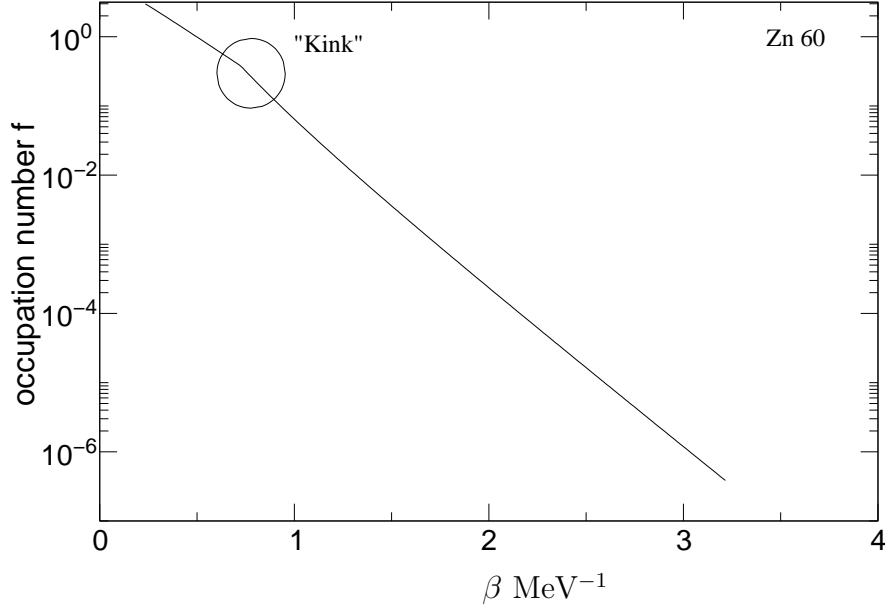
Figure 3.5: *Occupation number f as a function of the inverse temperature. The kink around the critical temperature β_c comes from a sudden transition from the Fermi- to the BCS-regime.*

II) Description of the occupation number f by a superposition of the following form:

$$f = f_{BCS} + (f_{fermi} - f_{BCS}) \times \Phi(\beta) \, ,$$

where $\Phi(\beta)$ was chosen in such a way that in the high and low temperature regime the correct distribution was recovered. For example: $\tanh(1/\beta)$ fulfills this requirement as

$$\lim_{\beta \to \infty} \Phi(\beta) = 0 \text{ , hence } f \to f_{BCS}$$
$$\lim_{\beta \to 0} \Phi(\beta) = 1 \text{ , hence } f \to f_{fermi}$$

Unfortunately, this attempt was not successful, as it generated oscillations in the projected heat capacities.

III) Use of only one description for the whole regime, hoping to avoid numerical problems in the calculation of the derivatives. It was decided to use the BCS description even in the high temperature regime. This is possible, if one can find a way to suppress the pairing gap contribution. We rewrote the quasi-particle occupation number in the following form:

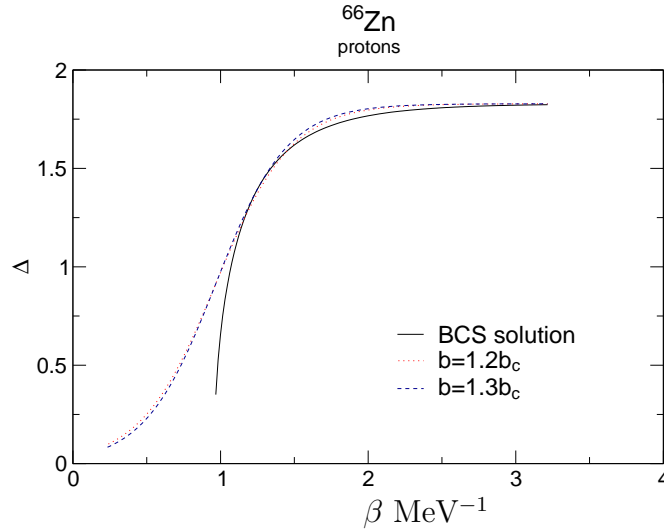$$f_{BCS} = \frac{1}{1 + e^{\beta E_k}} = \frac{1}{1 + e^{\beta(\epsilon_k - \mu)\tilde{E}_k}} \, ,$$

Figure 3.6: *Dependence of the pairing-gap fit on the choice of the critical temperature.*

with $\tilde{E}_k = \sqrt{1 + \Phi(\beta)(\frac{\Delta}{\epsilon_k - \mu})^2}$. The function Φ was chosen in such a way that the logarithmic derivative at the critical temperature is smooth. Unfortunately this approach again generated oscillations in the projected heat capacities.

Unfortunately, all the described attempts so far failed to describe a smooth transition between the two regimes. Inspired by the last unsuccessful attempt, we finally were able to solve the problem.

The key to the solution of the problem was simply to extrapolate the pairing gap itself to higher temperatures. As the pairing effects are washed out for higher temperatures the gap itself should vanish and the Fermi-Dirac distribution will be recovered. We chose a Fermi-type dependence of the pairing gap as a function of the inverse temperature:

$$\Delta(\beta) = \frac{\Delta_0}{1 + \exp(-(\beta - \beta_c)/a)} \ ,$$

where Δ_0 denotes the pairing gap for $T = 0$. The critical temperature at which the transition occurs is denoted by β_c, the diffuseness parameter is given by a. Requiring that the extrapolated value for the gap equals the exact value of the BCS solution at the critical temperature, which we define by $\beta_c = c\beta_c$, we can write the diffuseness parameter as:

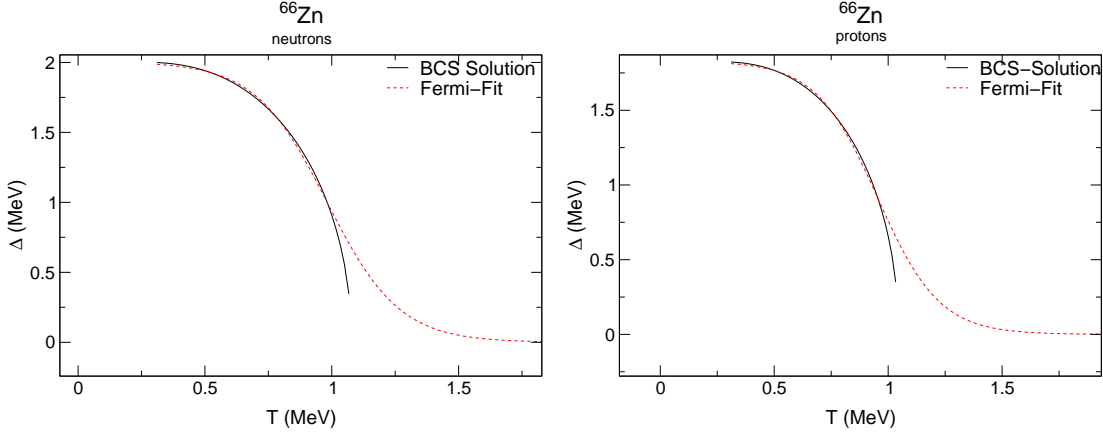$$a = \frac{\beta_c - \beta}{\ln(\frac{\Delta_0}{\Delta_\beta} - 1)} \ . \tag{3.26}$$

Figure 3.7: *Pairing Gap Δ fitted by a Fermi-type function.*

In Figure 3.6 the extrapolated pairing gap is shown for two values of c. We have chosen the critical temperature in such a way to obtain a smooth transition to zero over a range of 1 MeV [LDRK96]. A value of $c = 1.2$ was chosen for all nuclei. Figure 3.7 shows nicely the smooth transition from the BCS to the Fermi regime as a function of temperature.

Short summary

The occupation number f is calculated in the following way:

1.) Solve the gap equations until break-down of the solution:

$$\tilde{n} = \frac{1}{2} \sum_k \left(1 - \frac{\epsilon_k - \mu}{E_k} \tanh\left(\frac{\beta}{2} E_k \right) \right) - n \qquad (3.27)$$

$$\tilde{G} = \frac{1}{2} \sum_k \left(\tanh\left(\frac{\beta}{2} E_k \right) / E_k \right) - \frac{2}{G} \ . \qquad (3.28)$$

2.) Fit the energy gap Δ as a function of the temperature:

$$\Delta(\beta) = \frac{\Delta_0}{1 + \exp(-(\beta - \beta_c)/a)} \ .$$

3.) Recalculate the chemical potential using the BCS equations and the extrapolated value for Δ.

4.) From the pairing gap and the chemical potential known for all temperatures, we can now calculate the occupation number of the π^s parity group

$$f = \sum_{k \in \pi^s} \frac{1}{1 + e^{\beta \sqrt{(\epsilon_k - \mu)^2 + \Delta^2}}} \ . \qquad (3.29)$$
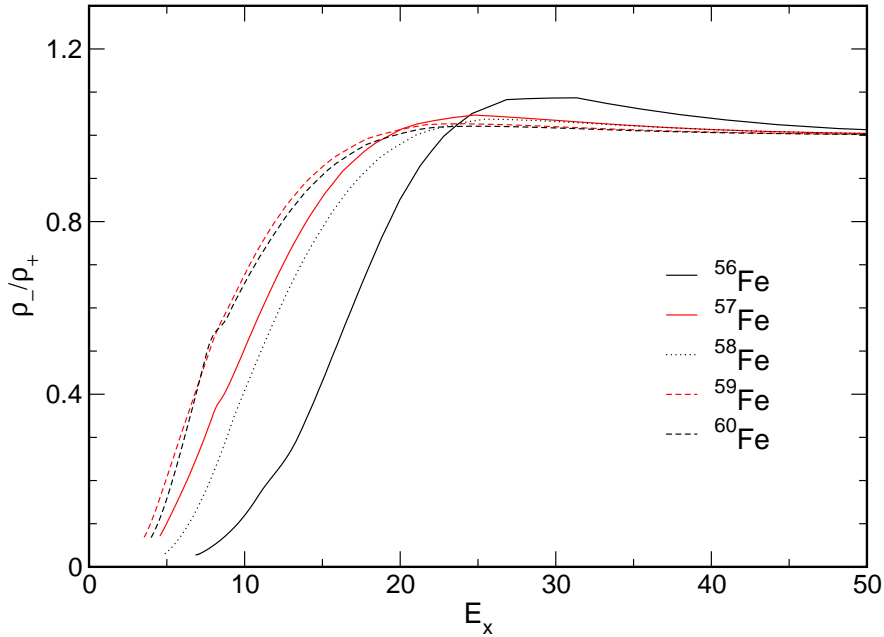
Figure 3.8: *Evolution of the odd- to even parity ratio in the Fe-chain.*

The influence of pairing on the odd- to even-parity ratio is shown in Figure 3.8. Starting with 30 neutrons in ^{56}Fe, the pf-shell of the neutrons is getting more and more populated while approaching ^{60}Fe. The energy necessary to induce an overall parity change by an excitation from the pf to the $g_{9/2}$ shell, is gradually decreased. One can clearly see that the ratio for odd-A nuclei equilibrates for lower excitation energies compared to the even-A neighbors. This is a clear manifestation of the pairing effect, as one has to break a pair first, which costs about 1 MeV. After the pair has been broken, the individual neutrons then can contribute to a parity changing excitation.

3.2.3 Single particle energies

The detailed knowledge of the single particle energies is a crucial ingredient in the calculation of the parity projected nuclear level densities, as the total parity of the whole system can only be changed by excitations of nucleons between shells with opposite parity, see Figure 3.10a.

However, the knowledge of the single particle energies alone is not sufficient to describe the correct crossover behavior of the odd- to even parity ratio from lower to higher excitation energies. The size of the model space, that means the amount of considered single particle levels, is as important as the relative distance between the levels itself. In Figure 3.9 the dependence of the parity projected ratio for ^{56}Fe is shown for different sizes of the model space. Starting with the $pf + g_{9/2}$
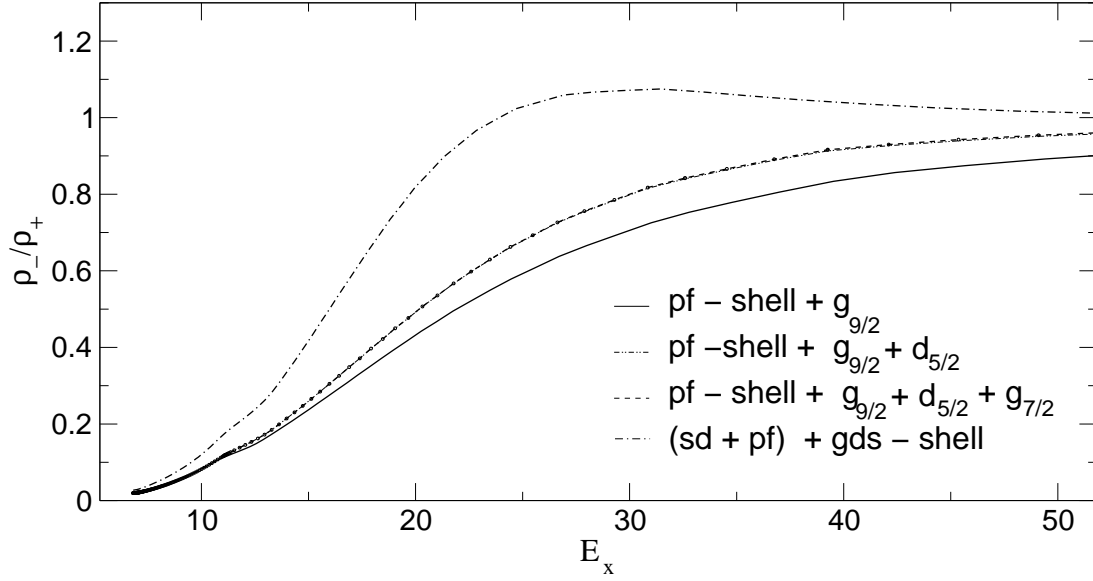
Figure 3.9: *Parity ratio as function of excitation energy E_x (MeV) for different sizes of the model space.*

configuration, where the parity can only be changed by excitations to the $g_{9/2}$-shell, and stopping with the full inclusion of the gds-shell, where excitations from the sd- to the pf-shell are taken into account, we can see that the previously performed calculations by Alhassid e.a. [ABLN00] have not converged yet. All major shells up to $11\hbar\omega$ were included which allows us to extend our calculations way beyond the previously studied $pf + g_{9/2}$-shell.

The single particle levels were calculated in a deformed Saxon-Woods potential [DPPS69] with parameters from [TOPS79] which reproduce experimental data well [NFS$^+$93] and [SMNF93].

It is very important for the calculation of the single particle energies to take deformation effects into account, as the single particle levels will be shifted towards higher or lower energies depending on the value of deformation. In figure (3.10b) the parity ratio for ^{64}Fe is plotted, once with deformation and once with deformation set to zero. One can see that the peak position and the strength of the peak depends on deformation.

3.2.4   Thermodynamical relations

The ratio of the parity-projected nuclear level densities can be calculated by applying the inverse Laplace transform on the parity-projected partition functions. The parity-projected partition functions are related to each other by
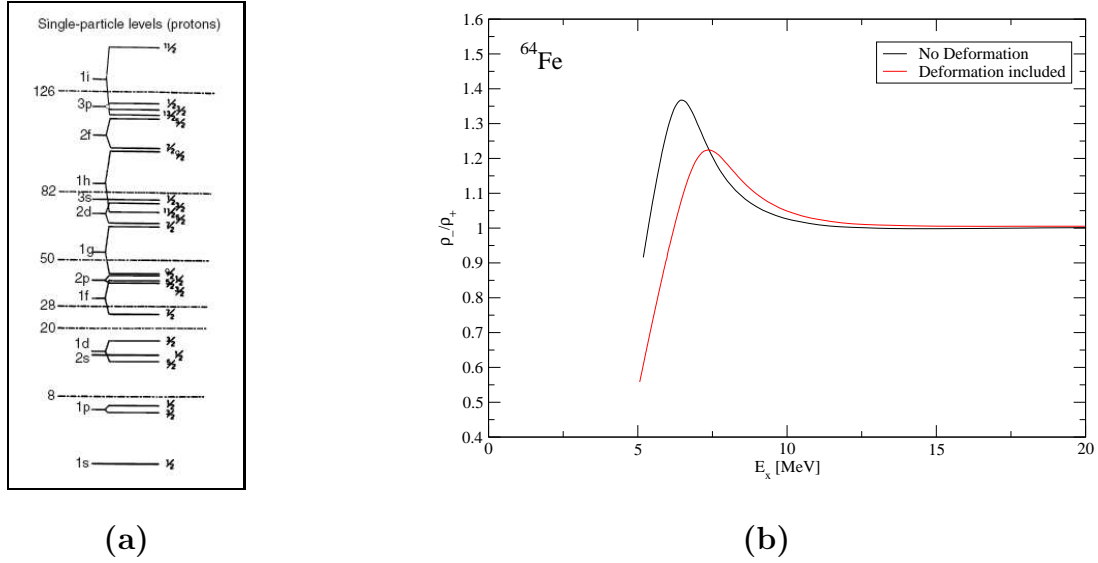
$$\frac{Z_-}{Z_+} = \tanh f \tag{3.30}$$

Figure 3.10: *(a): Single particle levels for protons taken from [Kli52]. (b): Influence of deformation on the projected parity ratio.*

and

$$Z_- + Z_+ = Z \ ,$$

if a positive ground state parity of the nucleus is assumed. For the rest of this section we will stick to this assumption. In order to evaluate the expression for the saddle point approximation, the knowledge of the parity-projected heat capacities, entropies and average energies are needed, which are indirectly linked to the unprojected ones through equation (3.30).

Thermodynamic quantities

The total partition function Z is given by:

$$Z(\beta) = e^{-\beta E_{g.s.}} \int \rho(E_x) e^{-\beta E_x} dE_x \ , \tag{3.31}$$

where E_x denotes the excitation energy and $E_{g.s.}$ the ground state energy of the nucleus. The nuclear level density $\rho(E_x)$ is calculated in a back-shifted Fermi-gas approach.

The thermal energy is defined by $E = -\frac{\partial \ln Z}{\partial \beta}$:

$$E = E_{g.s.} + \frac{\int dE_x E_x \rho(E_x) e^{-\beta E_x}}{\int dE_x \rho(E_x) e^{-\beta E_x}} \ , \tag{3.32}$$

where the last part can be identified as the average excitation energy

$$\langle E_x \rangle = \frac{\int dE_x E_x \rho(E_x) e^{-\beta E_x}}{\int dE_x \rho(E_x) e^{-\beta E_x}} \ . \tag{3.33}$$

In a similar way, the heat capacity is defined by $C = -\beta^2 \frac{\partial^2 \ln Z}{\partial \beta^2}$:

$$C = -\beta^2 \left[\langle E_x^2 \rangle - \langle E_x \rangle^2 \right] \ , \tag{3.34}$$

with

$$\langle E_x^2 \rangle = \frac{\int dE_x E_x^2 \rho(E_x) e^{-\beta E_x}}{\int dE_x \rho(E_x) e^{-\beta E_x}} \ . \tag{3.35}$$

Projected quantities

We can calculate the parity projected thermodynamical quantities in the same way as described above - we have only to replace the total partition function by the projected ones. The parity projected partition functions are given by:

$$
\begin{aligned}
Z^+ &= \frac{Z}{1 + \tanh f} \\
Z^- &= Z \left(1 - \frac{1}{1 + \tanh f} \right)
\end{aligned}
\tag{3.36}
$$

or expressed via the logarithms

$$
\begin{aligned}
\ln Z^+ &= \ln Z - \ln(1 + \tanh f) \\
\ln Z^- &= \ln Z + \ln(1 - (1 + \tanh f)^{-1}) \ .
\end{aligned}
\tag{3.37}
$$

The projected energies are given by

$$
\begin{aligned}
E_+ &= E + \frac{1}{\sinh f + \cosh f} \frac{1}{\cosh f} \frac{df}{d\beta} \\
&= E + \frac{2}{1 + e^{2f}} \frac{df}{d\beta} \\
E_- &= E - \frac{1}{\sinh f + \cosh f} \frac{1}{\sinh f} \frac{df}{d\beta} \ , \\
&= E - \frac{2}{1 - e^{2f}} \frac{df}{d\beta} \ ,
\end{aligned}
\tag{3.38}
$$

and the heat capacities by

$$
\begin{aligned}
C_+ &= C - \beta^2 \frac{2}{1 + e^{2f}} \left(\frac{d^2 f}{d\beta^2} - \frac{2}{1 + e^{-2f}} \left(\frac{df}{d\beta} \right)^2 \right) \\
C_- &= C + \beta^2 \frac{2}{e^{2f} - 1} \left(\frac{d^2 f}{d\beta^2} - \frac{2}{1 - e^{-2f}} \left(\frac{df}{d\beta} \right)^2 \right) \ .
\end{aligned}
\tag{3.39}
$$

Numerical treatment of the integrals

The integrals which appear in the calculation of the thermodynamical quantities are all of a similar form. Due to the exponential suppression of the integrand, the integrals can be computed numerically by the so-called *Gauss-Laguerre* integration scheme, where the integration can be approximated by the sum of its functional values at a set of points, multiplied by certain aptly chosen weighting coefficients:

$$\int_0^\infty dx f(x) x^\alpha e^{-x} = \sum_{i=1}^N w_i f(x_i) \,, \tag{3.40}$$

where the coefficients w_i are called weights. The weights can be calculated by the formula

$$w_i = \frac{\langle L_{N-1} | L_{N-1} \rangle}{L_{N-1}(x_i) L'_N(x_i)} \,.$$

Details can be found in [PTVF96], where the *Laguerre*-Polynomials are denoted by L. The abscissas x_i, at which the function has to be evaluated, are given by the roots of the *Laguerre* polynomials.

The integrals in equations (3.32) - (3.34) are not yet in the right form to apply equation (3.40), we have to rewrite them slightly.
Having chapter (3.3) in mind, the lower integration border is set to E_0, an arbitrary energy shift. The partition function can be written as:

$$
\begin{aligned}
Z &= \int_{E_0}^\infty dE\, e^{-\beta E} \rho(E) \\
&= \int_0^\infty dE'\, e^{-\beta(E'+E_0)} \rho(E' + E_0) \\
Z &= \frac{1}{\beta} e^{-\beta E_0} \int_0^\infty dE_x \rho(\frac{1}{\beta} E_x + E_0) e^{-E_x} \,.
\end{aligned}
$$

After the transformation, we can approximate the integral by equation (3.40):

$$Z = \frac{1}{\beta} e^{-\beta E_0} \sum_i w_i \rho(\frac{1}{\beta} E_i + E_0) \,. \tag{3.41}$$

The thermal energy is given by

$$E = -\frac{\partial \ln Z}{\partial \beta} = \frac{1}{Z} \frac{\partial Z}{\partial \beta} = \frac{1}{Z} \underbrace{\int_{E_0}^\infty dE\, \rho(E) E e^{-\beta E}}_{I} \,.$$

In the same way we can approximate the integral I by:

$$I = \int_0^\infty dE' \rho(E' + E_0)(E' + E_0) e^{-\beta(E'+E_0)}$$

$$= e^{-\beta E_0} \int_0^\infty dE' \rho(E' + E_0) e^{-\beta E'} + E_0 e^{-\beta E_0} \int_0^\infty dE' \rho(E' + E_0) e^{-\beta E'}$$

$$= e^{-\beta E_0} \frac{1}{\beta^2} \int_0^\infty dE_x \rho(\frac{1}{\beta} E_x + E_0) E_x e^{-E_x} + E_0 \underbrace{e^{-\beta E_0} \frac{1}{\beta} \int_0^\infty dE_x \rho(\frac{1}{\beta} E_x + E_0) e^{-E_x}}_{=Z}$$

$$I = \tilde{E} + E_0 Z \ ,$$

with

$$\tilde{E} = \sum_i w_i \rho(\frac{1}{\beta} E_i + E_0) E_i \ .$$

Without derivation, we can approximate the heat capacity by:

$$C = \tilde{C} + 2 E_0 \tilde{E} + E_0^2 Z \ , \tag{3.42}$$

where $\tilde{C}$ is given by

$$\tilde{C} = \frac{1}{\beta^3} e^{-\beta E_0} \sum_i w_i E_i^2 \rho(\frac{1}{\beta} E_i + E_0) \ .$$

3.3   Make Everything Consistent

There are two essential inputs to our calculations: the total level density ρ which is used to calculate the total partition function (and indirectly all other thermodynamical quantities) and the single particle levels from the deformed Saxon-Woods potential needed to compute the average occupancy f. Both inputs are prone to possible uncertainties due to the models employed to generate them.

In a fully consistent model, single particle levels determine the level density assuming all effects have been properly accounted for and that the level density can be computed, e. g. in a shell model, for all nuclei at all relevant excitation energies. This is not possible because of the afore mentioned limitations of the shell model approaches. For all practical purposes it is therefore advantageous to include level densities derived in other approaches, such as the shifted Fermi-gas. Proceeding in this manner, however, great care has to be put into achieving consistency between the single particle structure from the Saxon-Woods model and the Fermi-gas level density. Both inputs should actually be made convergent by simultaneously adapting the Saxon-Woods potential and varying the level density parameter. Here we assume that the single particle levels given in the Saxon-Woods potential are correct. Therefore we developed an interation method to achieve consistency of the Fermi-gas level density by varying the level density parameter only.

Figure 3.11 shows the impact of varying the level density parameter a in the range of $7.5 \leq a \leq 14$ MeV^{-1}. This corresponds to a ± 40 % variation of the standard parameter a and implies a change in ρ up to a factor 5 at an excitation energy of 3.5 MeV. It has to be emphasized once more that this large variation of

Figure 3.11: *Influence of the input level density parameter a on the peak strength in ^{70}Zn. The black curve is obtained by using the standard level density parameter. The dashed (dotted) curve corresponds to a variation of the level-density parameter a which translates to a variation of the input level density by a factor 2 or 5, respectively.*
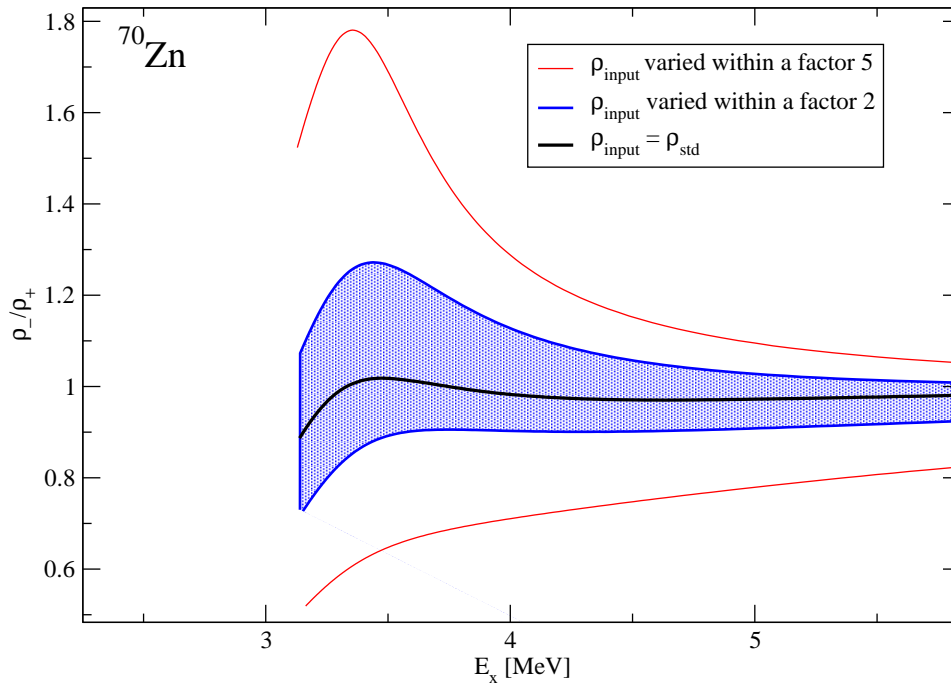
the level density is not due to the uncertainty of ρ alone but rather is supposed to contain the combined uncertainties in ρ *and* the single particle levels. Figure 3.11 clearly shows the need for improved consistency within inputs, especially at shell closures.

Starting with the back-shifted Fermi-gas for the input level density, an iteration scheme is carried out until convergence between the input level density and the extracted level density from the projected quantities is achieved. A schematic overview of the whole iteration procedure is shown in Figure 3.12.
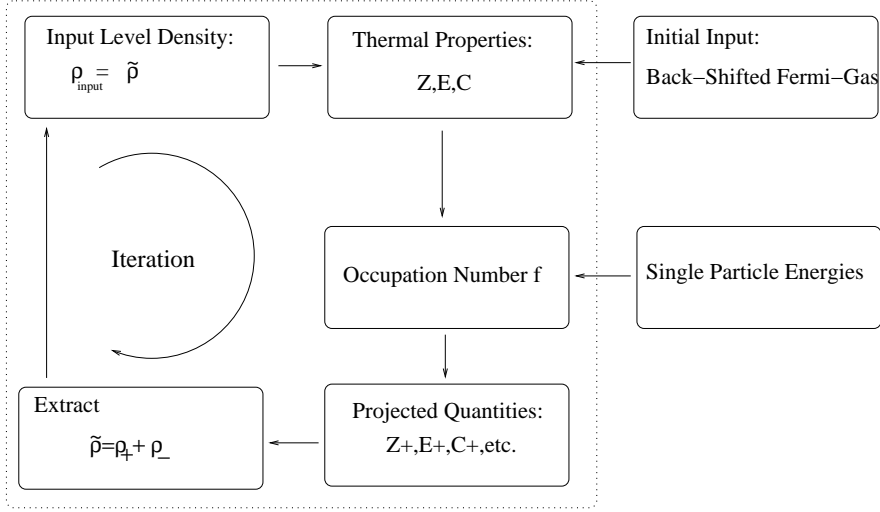
Figure 3.12: *Overview of the iteration procedure: The iteration is performed until convergence between the input level density and the extracted level density from the projected quantities is achieved.*

In the first iteration step the parity projected level-density

$$\rho_+(E) = \frac{1}{\sqrt{2\pi C_+}}\beta^+ \exp(\beta^+ E + \ln Z^+) \; ,$$

$$\rho_-(E) = \frac{1}{\sqrt{2\pi C_-}}\beta^- \exp(\beta^- E + \ln Z^-)$$

is calculated as described in chapter 3.1. The total level density after the first iteration process is then given by the sum of the parity projections:

$$\rho^{(\mathrm{it})} = \rho_+ + \rho_- \; .$$

As we use the inverse temperature β as the independent variable in our calculations, where the grid spanned a range between $\beta_{\min} = 1.25 \times 10^{-1}$ MeV^{-1} and $\beta_{\max} = 6.2$ MeV^{-1}, the energy range of the iterated total level density was limited to an excitation energy range between 2 and 50 MeV, depending on the specific nucleus. Within this energy range the iterated level density $\rho^{(\mathrm{it})}$ was compared to the level density with which the iteration cycle was started. We used the averaged ratio as a quantitative overall estimate of the agreement between the two level densities

$$g = \left\langle \frac{\rho^{\mathrm{it}}}{\rho^{\mathrm{input}}} \right\rangle = \exp\left[\frac{1}{n}\sum_{i=1}^{n}\left(\ln \frac{\rho_i^{\mathrm{it}}}{\rho_i^{\mathrm{input}}}\right)^2 \right]^{1/2} \; , \qquad (3.43)$$

with n being the number of excitation energies within the calculated energy range. The iteration scheme was considered to be converged for $|1 - g| < 0.05$.
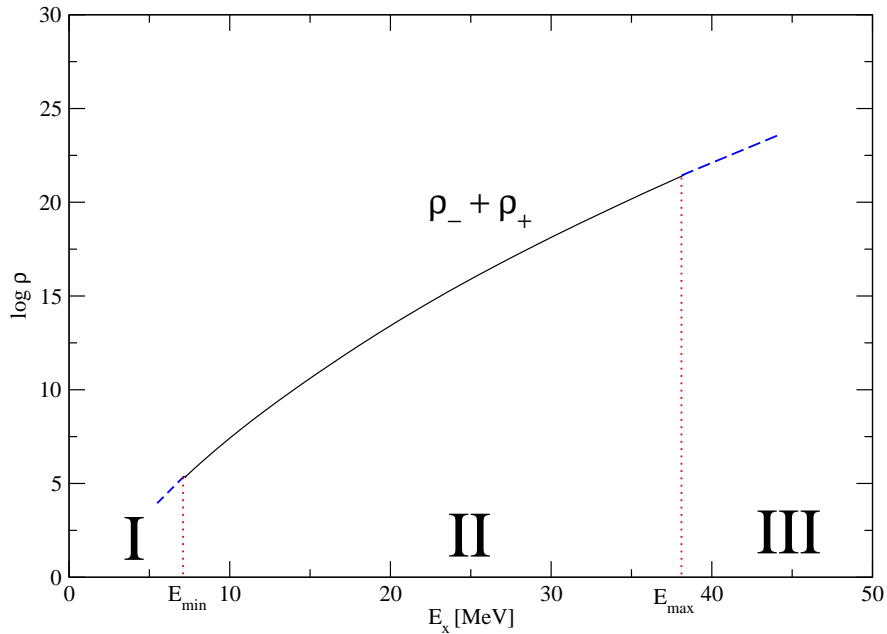
Figure 3.13: *Nuclear level density after the first iteration step. The level density is only known in the energy range II, it has to be extrapolated in the regimes I and III.*

Figure 3.13 illustrates the problem of the limited energy range II for which the level density is known after the iteration step. Thermodynamical quantities such as the partition function for instance, require an integration over the excitation energy from zero to infinity. Therefore, we have to extrapolate the known level density to the energy ranges I and III, respectively. In chapter 2 it was shown that the low energy regime of the level density can be described by the constant-temperature formula. For this reason we have chosen a similar ansatz for the extrapolation into range I:

$$\rho_\mathrm{I}(E) = N\frac{e^{E/T}}{T} \ , \tag{3.44}$$

where the unknown parameters N and T are determined by a tangential fit at the matching energy $E = E_\mathrm{min}$. The high energy range III can be described by a back-shift ansatz for the level density:

$$\rho_\mathrm{III}(E) = N\frac{1}{E^{5/4}}e^{2\sqrt{aE}} \ , \tag{3.45}$$

where again the unknown parameters a and N are determined by a tangential fit at the matching energy $E = E_\mathrm{max}$.

A typical result for this iteration procedure is shown in Figure 3.14 for ^{90}Zr. Convergence in the sense of (3.43) is already achieved in the third iteration step.
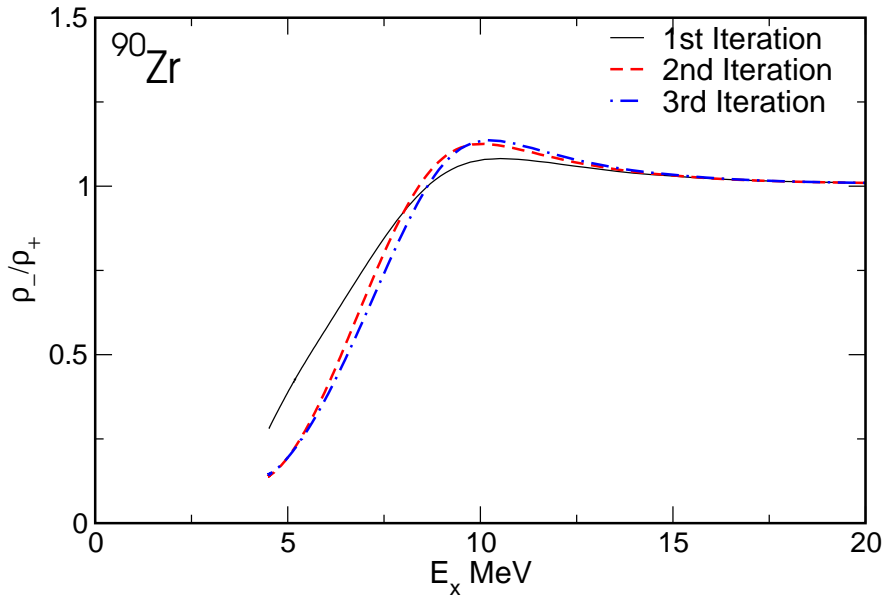
Figure 3.14: *Odd to even parity ratio for ^{90}Zr as a function of the excitation energy for three differnet iteration steps. Convergence is already reached in the 3rd iteration step.*

3.4   Results

We have already seen in section 3.1 that parity can only be changed by excitations between single particle levels of different parity. Such changes are of maximal amplitude where a major shell is completelly filled and the next available shell to populate has the opposite parity. The results for three different isotopic chains are shown in Figures 3.15 - 3.17. The evolution of the odd- to even-parity ratio at the interface of the $sdg-$ to pf-shell is shown in Figure 3.15 for four different Ni-isotopes. The sd-shell is filled completely in neutrons for ^{48}Ni. Every excitation of ^{48}Ni populates a single particle level of opposite parity leading to a maximal parity change. The formation of the peak can already be seen for ^{47}Ni. The position of the peak is shifted towards smaller excitation energies. This energy-shift is about 1 MeV, reflecting the energy that is needed to break a neutron pair prior to excitation. ^{49}Ni and ^{50}Ni, which both already populate the pf-shell in neutrons, equilibrate at much higher excitation energies. This is not suprising, as the next possible parity change can only be achieved by excitations to the $g_{9/2}$ shell. The evolution of the parity ratio for Ni isotopes at the interface of the pf and gds shell is shown in Figure 3.16a. Again, a similar behavior can be observed. The $N = 40$ neutron shell is completely filled for ^{68}Ni. Each excitation from the last occupied $2p_{1/2}$ level with negative parity will populate levels from the gds shell with positve parity resulting in a parity-change of maximal amplitude. The formation of the peak can already be seen for ^{66}Ni. The position of the peak is
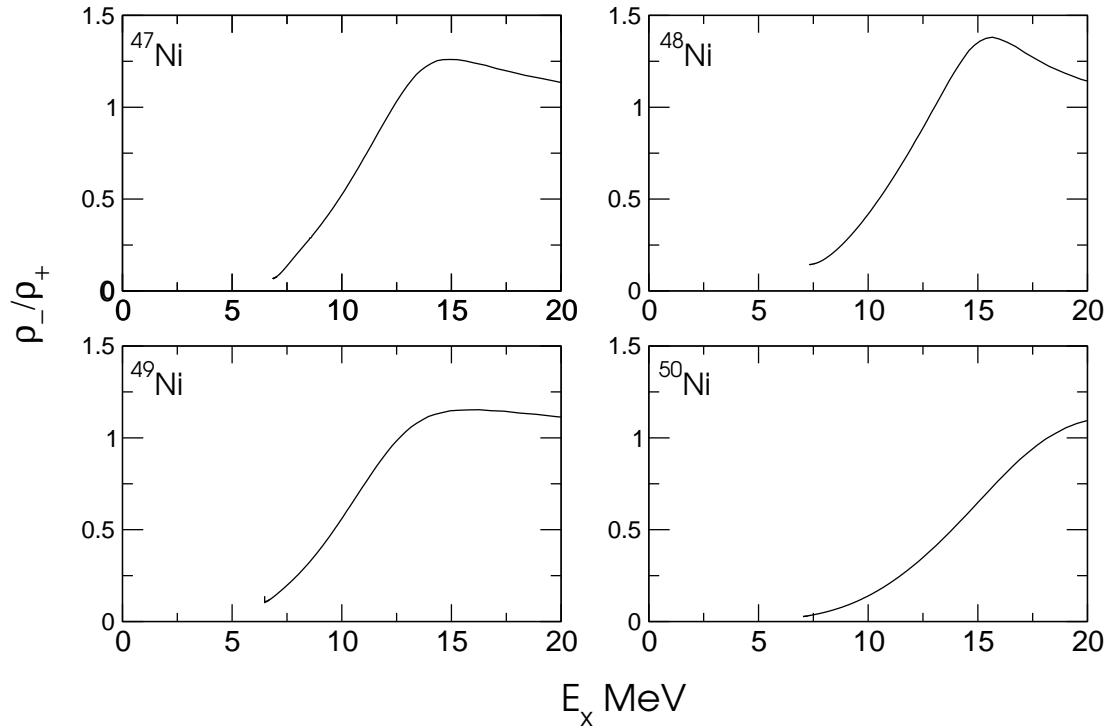
Figure 3.15: *Evolution of the odd- to even-parity ratio within the Ni-chain in the vicinity of the interface of the sdg- to pf-shell for neutrons.*

shifted to higher energies as a larger gap between the $2f_{5/2}$ level and the $g_{9/2}$-level has to be bridged. A similar behaviour can be observed in Figure 3.16b where the evolution of the parity-ratio for Sr isotopes at the pf and gds interface is shown. The pf neutron shell is completely filled for ^{78}Sr where again, every excitation leads to a parity change and thus leads to a formation of a peak in the odd- to even-parity ratio. In Figure 3.17a the evolution of the parity ratio in the vicinity of the gds- and pfh-shell is shown. Every excitation of even parity levels within the gds-shell to odd-parity levels within the pfh-shell lead to a parity change. This change is maximal for ^{120}Sn where the gds-shell is completely filled with neutrons.

So far we have discussed the evolution of the parity ratio only for isotopic chains, where each parity change results in an excitation of a neutron only. In Figure 3.17b the evolution of the $N = 50$ isotone parity ratios are shown. The proton numbers for the four shown nuclei (Y, Zr, Nb and Mo) are 39, 40, 41, and 42. Again a pronounced peak for ^{90}Zr can be observed as the pf-proton shell is completely filled with protons. Every excitation of the protons lead to a parity change.
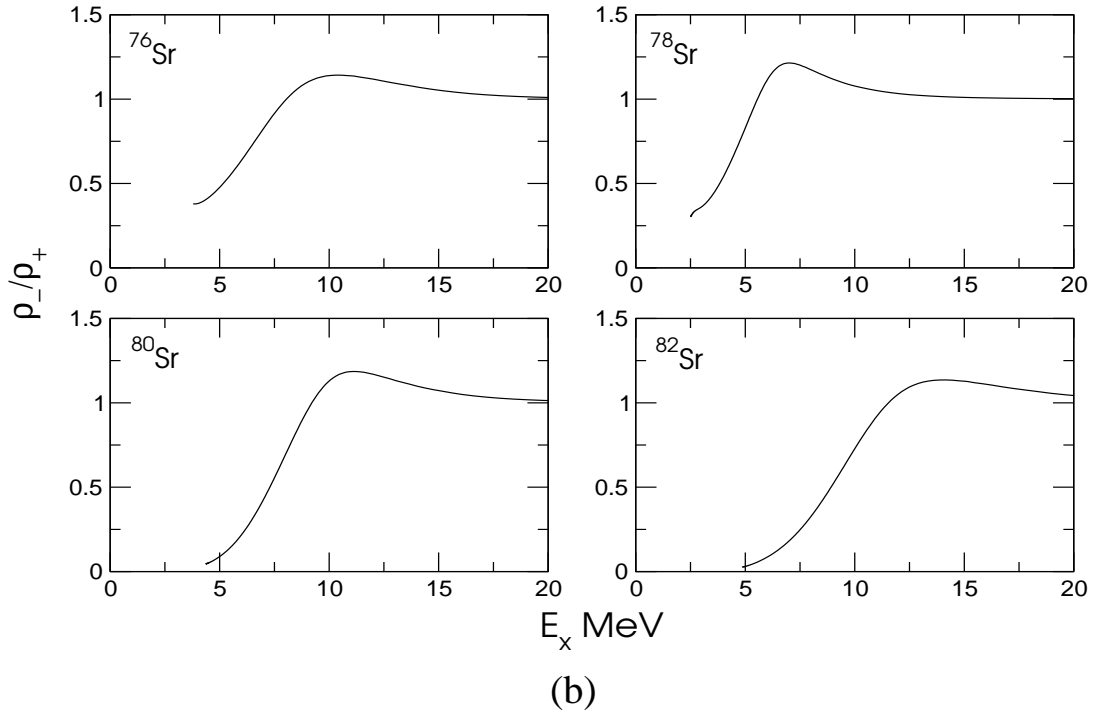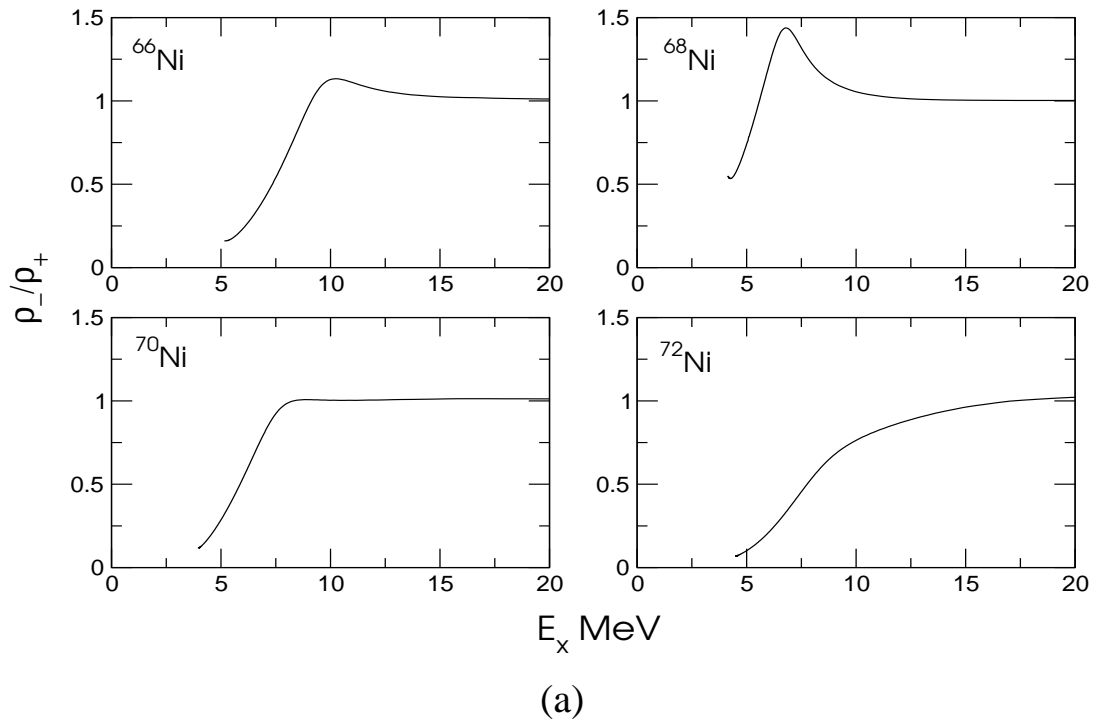
(a)

(b)

Figure 3.16: *(a): Evolution of the odd- to even-parity ratio within the Ni-chain in the vicinity of the interface of the pf- to gds-shell for neutrons. (b): Evolution of the odd- to even-parity ratio within the Sr-chain in the vicinity of the interface of the pf- to gds-shell for neutrons.*
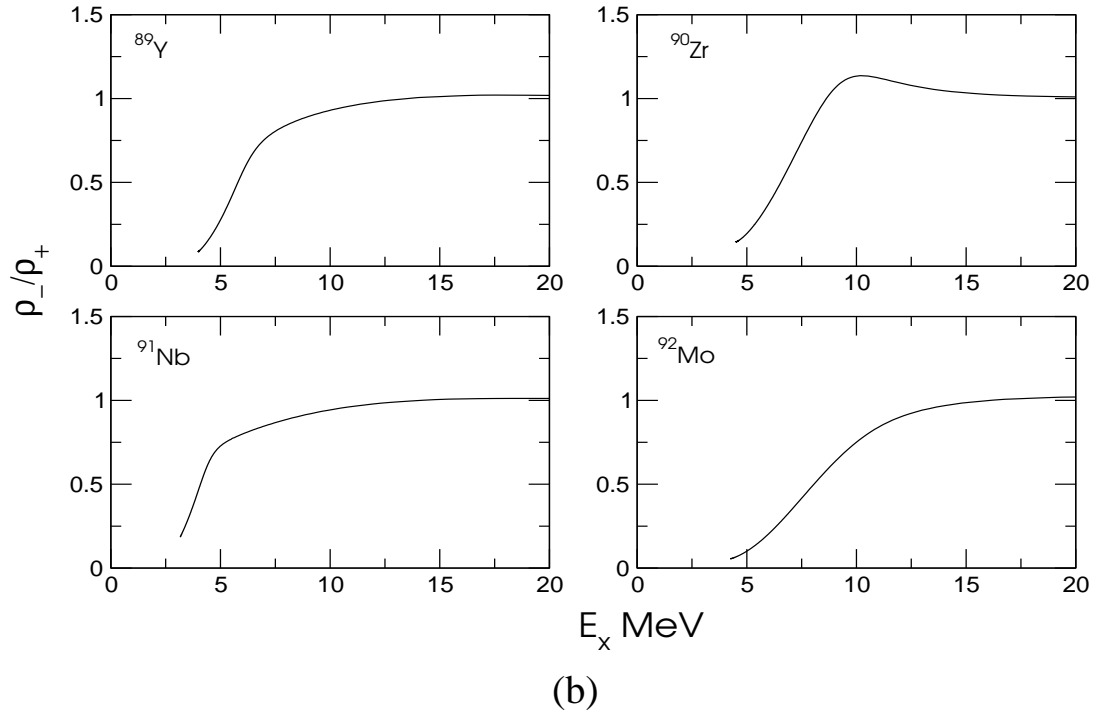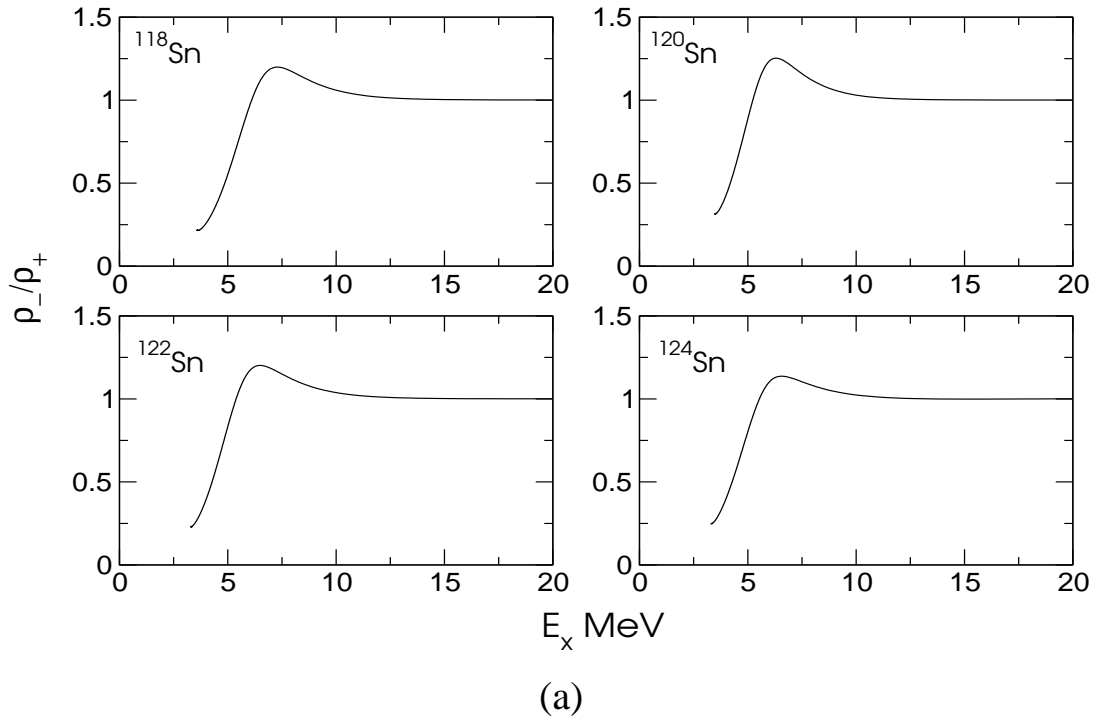
(a)

(b)

Figure 3.17: *(a): Evolution of the odd- to even-parity ratio within the Sn-chain in the vicinity of the interface of the gds- to pfh-shell for neutrons. (b): Evolution of the odd- to even-parity ratio within the N=50 isotone in the vicinity of the interface of the pf- to gds-shell for protons.*

Chapter 4
Formation of Heavy Elements

4.1 Introduction

One of the key questions in astrophysics is the origin of the elements which can
be found in the solar system. There are roughly one hundred chemical elements
and several hundred observable stable isotopes. The answer to this questions still
remains open, although in the last decades a lot of effort was put into unvovering
this prevailing mystery.

   The solar abundance distribution, shown in Figure 4.1, collected from stellar
spectra, cosmic rays, and meteorites found on Earth and on the Moon, describes
our most accurate knowledge of the element abundance distribution. Starting
with low mass elements, such as hydrogen and helium, which together form 98%
of the observed elements, and stopping with high mass elements, such as uranium
or gold, twelve orders-of-magnitude are spanned in the abundance distribution.
The structure of the distribution, an almost flat distribution up to iron, a peak
near iron, and an exponential decrease beyond iron, is an indicator that not all
elements were formed in the same astrophysical scenario. It is possible to group
the elements according to their production mechanism: big bang nucleosynthesis
(BBN), stellar burning and neutron capture processes. Big Bang nucleosynthesis
begins about one minute after the Big Bang when the universe has cooled enough
to form stable protons and neutrons. During the further expansion hydrogen,
helium, traces of deuterium and lithium were formed. All other elements were
formed later. The second group of elements from H to the iron group nuclei,
was formed through thermonuclear fusion of lighter elements during hydrostatic
evolution of massive stars. Stellar structure and evolution is controlled by two
forces: Gravity, which drives the collapse, and the internal pressure which is
responsible for the expansion of the stellar material. The starting point of star
formation is a pressure disbalance which enables the gravitational collapse to set
in. Due to the gravitational contraction the internal temperature of the star
increases until the central temperature is high enough to ignite the fusion of
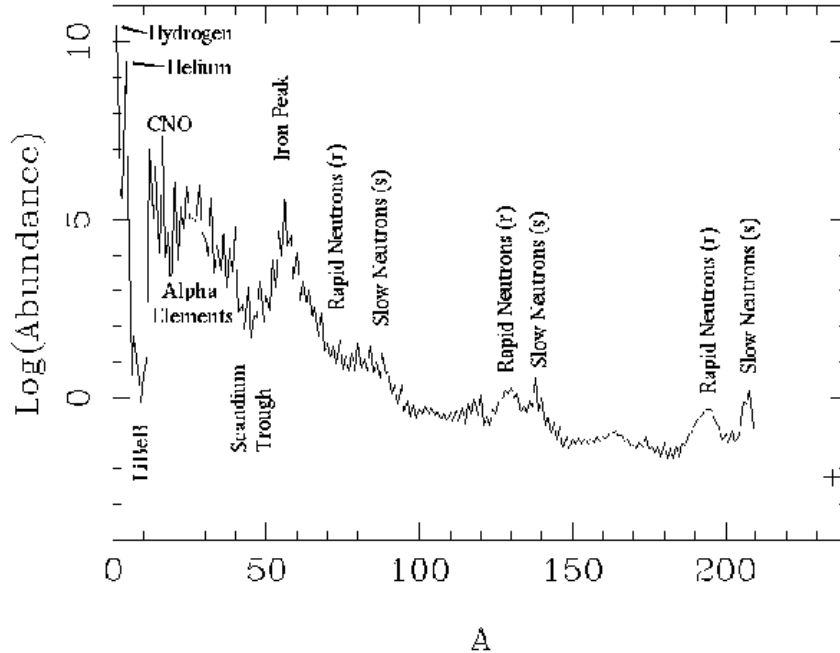
Figure 4.1: *The solar system abundance distribution of the elements relative to Si with abundance 10^6 .*

hydrogen to helium. This fusion process releases energy which increases the thermal pressure and counterbalances the gravitational contraction as long as there is enough hydrogen to be burnt. When the thermal pressure is not able to counterbalance the gravitational collapse the star will contract further. The central temperature increases and once again the innermost material, which is the ashes of the previous burning phase, is ignited resulting in an onion like structure of burnt material (H, He, C, O and Si, see Figure 4.2). The cycle of gravitational contraction, followed by an increase of the central temperature and the ignition of nuclear burning in the center cannot be maintained forever. Due to the Coulomb repulsion for nuclei beyond the iron group fusion processes become endothermic. At this point the gravitational collapse cannot be stopped and depending on the initial mass the star will be destroyed in violent explosion, called supernova, leaving a neutron star or black hole as remnant.

4.2 The s- and r-process

In the previous section we have discussed the formation of nuclei through fusion processes up to iron. Nuclei heavier than iron cannot be produced by thermonu-
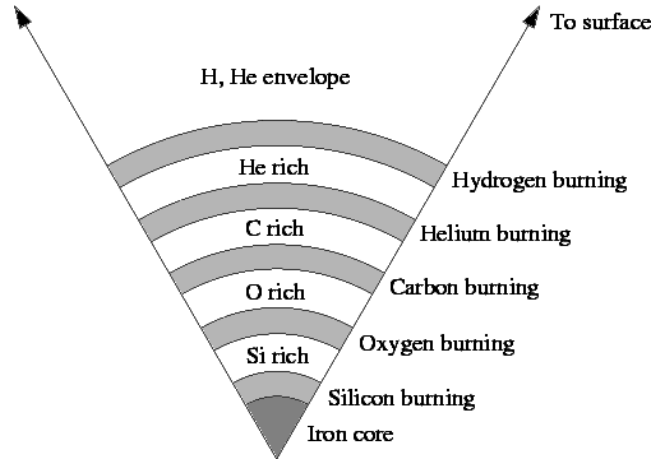
Figure 4.2: *Onion-Structure of the star after several burning phases*

clear charged particle reactions in hydrostatic burning due to the presence of the Coulomb barrier. The temperatures needed to overcome this barrier are so high that the synthesized nuclei will be photo-disintegrated immediately. However, the capture of neutrons is possible as these uncharched particles do not feel a Coulomb barrier. Elements heavier than iron can be synthesized by subsequent neutron captures and beta-decays occuring when the iron group nuclei are exposed to a flux of neutrons, as first suggested by [BBFH57]. Let us consider a sequence of reactions in such a scenario. There are two possibilities:

a.) The nucleus captures aneutron. The timescale of this reaction is determined by the averaged reaction rate $\lambda_{(n,\gamma)}$; or

b.) The nucleus beta-decays. The timescale of this reaction is given by the beta-decay constant λ_β.

Depending on the ratio of the two reaction rates the first or the second reaction will dominate.

First suppose $\lambda_\beta \gg \lambda_{(n,\gamma)}$. In this case, neutron capture is much slower than beta decay. Thus, stable nuclei will capture neutrons until a radioactive isotope is reached. At that point, β-decay will occur. The capture chain will then resume through the isotopes of the element with $Z + 1$ again until the next radioactive nucleus is produced. This type of neutron capture chain is called the slow neutron capture process, or s-process, as the neutron-capture rates are much smaller than the beta-decay rates. The s-process path proceeds along the valley of stability until ^{209}Bi is reached. Beyond this point, nuclei which capture a neutron immediately decay back by α-emission to lower masses.
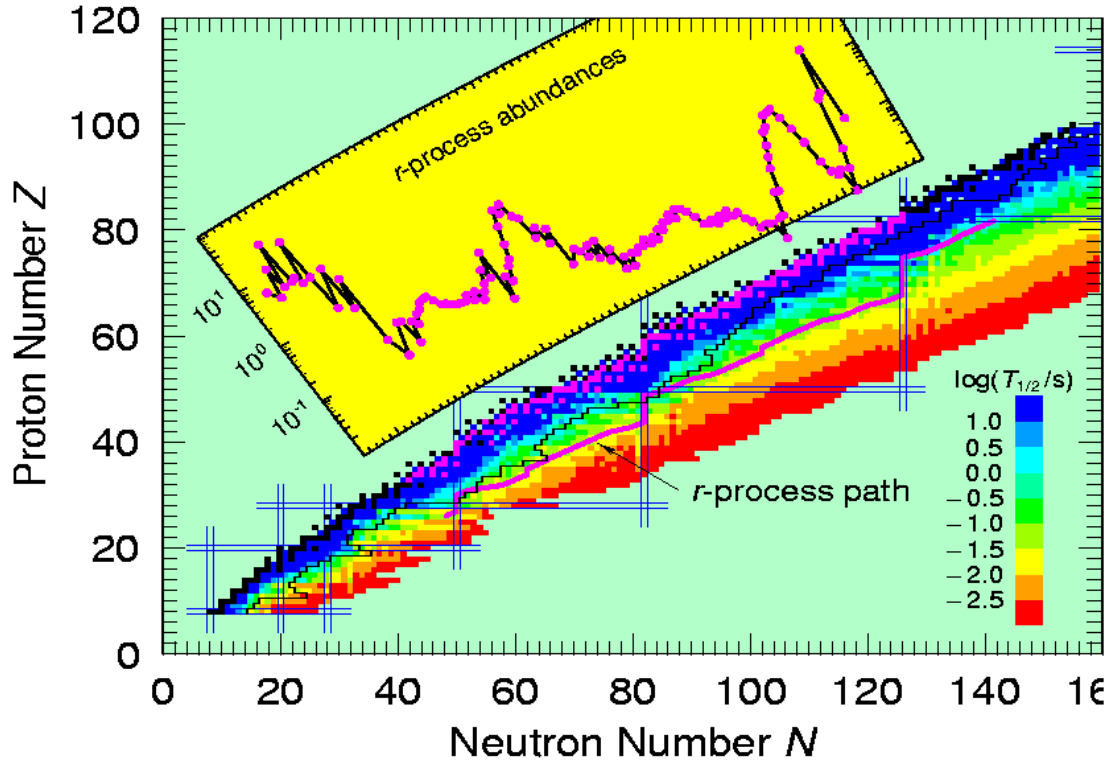
Figure 4.3: *Neutron capture paths for the s-process and the r-process. The zigzag path near the valley of stability is the r-process path, the violet path on the neutron rich side is the r-process path. Color-coded are the beta-decay half-lives calculated from FRDM theory with decreasing values while reaching the neutron drip-line.*

The s-process imposes certain features on the abundance distribution. At closed neutron shells - namely for N = 28,50,82, and 126 - the neutron capture cross-sections are much smaller than for neighboring neutron numbers. This means that each time one of these *magic* numbers is reached, it becomes significantly less likely for the nucleus to capture more neutrons. Elements corresponding to these magic numbers of neutrons will thus be especially abundant. These abundance peaks can be seen around ^{88}Sr, ^{138}Ba and ^{208}Pb, see Figure 4.1.

Next consider the extreme case of $\lambda_\beta \ll \lambda_{(n,\gamma)}$ for all nuclei in an isotopic chain. Because of the fast neutron captures, this is called rapid neutron-capture process or r-process. In this case, the neutron density and temperature have to be sufficiently high so that an $(n,\gamma) - (\gamma,n)$ equilibrium is established (5.3.2).

The neutron separation energy decreases with the increase of the neutron excess. The more neutrons a nucleus has captured, the easier the newly formed isotope can be photo-disintegrated by $\gamma + (Z, A + 1) \rightarrow (Z, A) + n$. Within

such an isotopic chain in equilibrium there are usually one or two nuclei which dominate the abundance distribution. These nuclei are called *waiting point* nuclei as the processing has to wait until these waiting points beta-decay to the next isotopic chain. The r-process path is defined by connecting the waiting-points for all elements. Due to the fast neutron captures, the r-process path is located far off stability, at nuclei with neutron separation energies of about 2-3 MeV. Waiting point nuclei with closed neutron shells are a bottle-neck in climbing the r-process path, due to the slow beta-decay rates. Once the neutrons disappear, all very neutron rich isotopes beta-decay towards the valley of stability. In particular, the elements concentrated at the three neutron magic numbers beta-decay to form three abundance peaks on the valley of stability. The mass numbers of these peaks are smaller than the mass numbers of the corresponding s-process magic number peaks, since they originated from elements with the same magic neutron numbers but smaller proton numbers. These abundance peaks are fingerprints of the r-process conditions.

Again, the magic neutron numbers operate, serving as bottlenecks to nuclei climbing the r-process path. However, this time the magic nuclei are of an exotic, highly neutron-rich type.

4.3 Numerical Treatment

4.3.1 Nuclear Reaction Networks

In an astrophysical plasma a whole variety of different reactions can occur simultaneously, producing and destroying nucleus i which can be described by [HT99]

$$\left(\frac{\partial n_i}{\partial t} \right)_{\rho=\text{const}} = \sum_j N_j^i r_j + \sum_{j,k} N_{j,k}^i r_{jk} \; , \tag{4.1}$$

where one-body reactions such as decays, photo-disintegrations, electron and positron captures and neutrino-induced reactions are described by $r_j = \lambda_j n_j$. Two body reactions are described by $r_{jk} = \frac{1}{1+\delta_{jk}} \langle \sigma v \rangle_{jk} n_j n_k$. The individual N^i's are positive or negative numbers specifying how many particles of species i are destroyed or created in a reaction. To avoid changes which are just due to density changes we make use of the so-called abundances Y^i which are defined by

$$Y^i = \frac{n_i}{\rho N_A} \; , \tag{4.2}$$

where N_A is Avogadro's number, ρ the matter density and n_i the number density of species i. In terms of nuclear abundances Y^i the nuclear reaction network (4.1) is then described by the following set of differential equations

$$\dot{Y}^i = \sum_j N_j^i \lambda_j Y_j + \sum_{j,k} \frac{N_{j,k}^i}{1+\delta_{jk}} \rho N_A \langle \sigma v \rangle_{jk} Y_j Y_k \; . \tag{4.3}$$

4.3.2 The Waiting Point Approximation

In order to describe the r-process nucleosynthesis in detail we have to consider the following reactions:

- neutron captures

- neutron-induced fission

- photodisintegration

- β-decays

- β-delayed neutron emission / fission

- neutrino-induced reactions

As all charged-particle reactions can be neglected in an r-process calculation, equation (4.3) reduces to

$$\dot{Y}(Z,A) = \underbrace{\sum_{Z',A'} \lambda_{Z',A'} Y(Z',A')}_{I} + \underbrace{\sum_{Z',A'} \rho N_A \langle \sigma v \rangle Y_n Y_{Z',A'}}_{II} \qquad (4.4)$$

where $Y(Z,A)$ is the nuclear abundance of isotope (Z,A) defined as $Y(Z,A) = X_i/A$, where A is the nucleon mass number and X_i is the so-called mass-fraction of the isotope (Z,A); we also have $\sum_i X_i = 1$. One-body reactions, such as beta-decays (with all possible emission channels), spontaneous fission, photodisintegration and neutrino-induced reactions are described by the first term (I) in equation (4.4). Neutron-induced reactions are described by the second term (II). Including only neutron-capture reactions, photo-disintegrations, beta-decay, beta-decay followed by one neutron emission (Figure 4.4) equation (4.4) can be written as:

$$\begin{aligned}
\dot{Y}(Z,A) &= n_n Y_{Z,A-1} \langle \sigma v \rangle_{(n,\gamma)} + Y_{Z,A+1} \lambda_{Z,A+1} - Y_{Z,A} \\
&\times \left(n_n \langle \sigma v \rangle_{(n,\gamma)} + \lambda_{Z,A} + \lambda^{\beta}_{Z,A} + \lambda^{\beta n}_{Z,A} \right) + Y_{Z-1,A} \lambda^{\beta}_{Z-1,A} \\
&+ Y_{Z-1,A+1} \lambda^{\beta n}_{Z-1,A+1}
\end{aligned} \qquad (4.5)$$

Provided there are a high neutron densities, $n_n > 10^{20}$ cm^{-3}, and high temperatures, $T > 10^9$K, neutron captures and photo-disintegrations occur on a much faster time scale than beta-decays (for these thermodynamic conditions the typical timescales of neutron-captures are of the order of 10^{-4} s, whereas beta-decays of the most abundant nuclei act on time-scales of $10^{-1} - 10^{-3}$ s). Due to this large difference, small beta-decay rates can be neglected in the time evolution of the abundances. For such conditions, equation (4.5) reduces to:

$$\dot{Y}(Z,A) = \lambda_{Z,A+1} Y(Z,A+1) - \langle \sigma v \rangle^{Z,A}_{(n,\gamma)} Y(Z,A) n_n . \qquad (4.6)$$
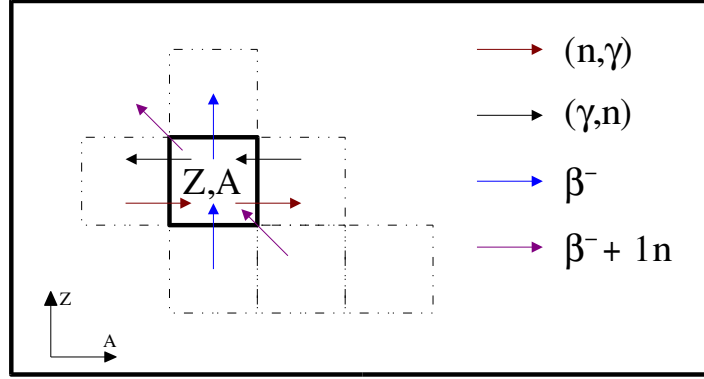
Figure 4.4: *Schematic view of reactions which can change the abundance of an isotope* (Z, A) *in the r-process*

Since nuclear reactions occur much faster than the hydrodynamic process timescales, an equilibrium is established within an isotopich chain, with

$$\dot{Y}(Z, A) = 0 \ ,$$

and therefore ,

$$\frac{Y(Z, A+1)}{Y(Z, A)} = \frac{\langle \sigma v \rangle^{Z,A}_{(n,\gamma)}}{\lambda_{Z,A+1}} n_n \ . \tag{4.7}$$

This approximation is known as the $(n,\gamma)-(\gamma,n)$ equilibrium or sometimes called the *waiting point approximation*. The reaction rates for the neutron-capture and photodisintegration in equation (4.6) are related by the detailed balance relation, introduced in chapter 4:

$$\lambda_{Z,A+1} = \frac{2g(Z,A)}{g(Z,A+1)} \left(\frac{A}{A+1}\right)^{3/2} \left(\frac{m_u kT}{2\pi\hbar^2}\right)^{3/2} \langle \sigma v \rangle_{(n,\gamma)} \exp\left(\frac{-B_n(Z,A+1)}{kT}\right) \ ,$$

where B_n denotes the neutron separation energy. We can insert this expression for the photodisintegration rate into equation (4.7) which allows us to write the abundance ratio of two neighboring isotopes within one isotopic chain as:

$$\frac{Y(Z, A+1)}{Y(Z, A)} = n_n \frac{g(Z,A+1)}{2g(Z,A)} \left(\frac{A+1}{A}\right)^{3/2} \left(\frac{2\pi\hbar^2}{\mu kT}\right)^{3/2} \exp\left(\frac{B_n(Z,A+1)}{kT}\right) \ . \tag{4.8}$$

In the waiting-point approximation no detailed knowledge of capture or photo-disintegration rates. The only nuclear input required to calculate the abundance ratio are the nuclear masses which enter in equation (4.8) through the neutron separation energy B_n. The abundance maxima (waiting points) within an isotopic chain depend on the B_n in the exponential. The astrophysical conditions, i. e. the neutron number density n_n and the temperature T, scale the abundances.

Up to this point we have only described the time-evolution within one isotopic chain, neglected the matter flow by beta-decays from one to the next isotopic chain. In order to illustrate this flow, we introduce the total abundance for each chain by

$$Y(Z) = \sum_A Y(Z, A) \;, \tag{4.9}$$

where the individual abundances of a nucleus can be expressed through so-called population coefficients $P(Z, A)$,

$$Y(Z, A) = P(Z, A)Y(Z) \;. \tag{4.10}$$

This population coefficients can be calculated by equation (4.8), and are normalized to one. In the waiting point approximation equation (4.6) can be finally written as

$$\dot{Y}(Z) = Y(Z-1) \sum_A P(Z-1, A)\lambda^\beta_{Z-1,A} - Y(Z) \sum_A P(Z, A)\lambda^\beta_{Z,A} \;, \tag{4.11}$$

or

$$\dot{Y}(Z) = \lambda^{\text{eff}}_{Z-1} Y(Z-1) - \lambda^{\text{eff}}_Z Y(Z) \;, \tag{4.12}$$

where the effective beta-decay rates

$$\lambda^{\text{eff}}_Z = \sum_A P(Z, A)\lambda^\beta_{Z,A}$$

have been introduced. For a full network calculation including thousands of nuclei a system of several thousand coupled differential equations has to be solved. The main advantage of the waiting point approximation is that the abundance distribution within an isotopic chain can be calculated from (4.8) and does not require the solution of a reaction network. Therefore the size of the system decreases to the number of different elements and not isotopes. Hence, one has to solve only $60 - 100$ coupled equations.

Numerical solution of the differential equation

In general, the differential equations describing the time evolution of the individual abundances have to be solved by numerical integration techniques. Equation (4.12), which describes the time evolution of the system in the waiting-point approximation, is an exception: there is an analytical solution. Differential equations of the type

$$\dot{Y}(Z) = \lambda(Z-1)Y(Z-1) - \lambda(Z)Y(Z) \;, \tag{4.13}$$

are called Bateman equations, named after the British mathematician Harry Bateman. Their analytical solution (4.13) is given by

$$Y(Z, t) = Y_0 \sum_{i=Z_0}^Z \left\{ \frac{\lambda_i}{\lambda_Z} \left(\Pi^Z_{j=Z_0} \frac{\lambda_j}{\lambda_j - \lambda_i} \right) e^{-\lambda_i t} \right\} \;, \tag{4.14}$$

where Z_0 denotes the first isotopic chain with abundance Y_0. The abundances can be computed by this analytical formula as long as the waiting point approximation remains valid and as long as the material flow from one isotopic chain to the other can be described by beta-decays. With increasing nuclear mass, new transmutation channels open. In addition to the already treated neutron-capture, photo-disintegration and beta-decay process, fission has to be taken into account. Such processes are not described by the Bateman-equation, therefore the analytical solution cannot be applied anymore.

One way to take fission into account is to solve the Bateman equation numerically. As the abundances $Y(Z)$ can rapidly change by many orders of magnitude within the integration interval, equation (4.13) is mathematically called a *stiff* differential equation. Stiff differential equations are mathematically well known but cause stability problems for explicit methods. Implicit methods are the most practical method for solving stiff systems. The disadvantage of having to solve a nonlinear system at each step is outweighed by the advantage of being able to take reasonably sized steps.

The simplest of all implicit numerical integration schemes is the so-called *backward* Euler scheme, which connects the solution at the time t with the solution at the time $t + \Delta t$ by

$$Y_{n+1} = Y_n + \Delta t Y'_{n+1} , \tag{4.15}$$

where Y_n and Y_{n+1} denote the solutions at time t and $t + \Delta t$, respectively. The derivative in equation (4.15) can be discretized as

$$\frac{Y(t + \Delta t) - Y(t)}{\Delta t} = Y'(t + \Delta t) = f(Y(t + \Delta t)) . \tag{4.16}$$

The abundances at the new time-step are given by

$$Y(t + \Delta t) = Y(t) + \Delta Y ,$$

where the abundance change ΔY, in the case of the Bateman equation, is given by:

$$\Delta Y = \lambda(Z - 1)\left(Y(Z - 1) + \Delta Y(Z - 1)\right) - \lambda(Z)\left(Y(Z) + \Delta Y(Z)\right)\Delta t . \tag{4.17}$$

Up to this point we have followed only the abundance change in one isotopic chain. The generalization of equation (4.17) for a system of differential equations yields:

$$\mathbf{A}\overrightarrow{\Delta Y} = \vec{B} , \tag{4.18}$$

which can be explicitly written as:

$$
\begin{pmatrix}
b_1 & & & & \\
a_1 & b_2 & & & \\
& a_2 & b_3 & & \\
& & \ddots & \ddots & \\
& & & a_{n-1} & b_n
\end{pmatrix}
\begin{pmatrix}
\Delta Y_1 \\
\Delta Y_2 \\
\vdots \\
\\
\Delta Y_n
\end{pmatrix}
=
\begin{pmatrix}
d_1 \\
d_2 \\
\vdots \\
\\
d_n
\end{pmatrix} .
$$

The coefficients are given by:

$$b_i = (\frac{1}{\Delta t} + \lambda_i) \, ,$$
$$a_i = -\lambda_i$$

and

$$d_i = \begin{cases} \lambda_{i-1}\Delta t Y_{i-1} - \lambda_i \Delta t Y_i & \text{if } i \neq 1 \\ -\lambda_1 \Delta t Y_1 & \text{otherwise .} \end{cases}$$

This system of equations can be solved easily for ΔY_i. The time-step Δt is chosen in such a way that $\sum_i |\dot{Y}_i/Y_i| < 10^{-4}$ is always fulfilled.

Some Results

In the previous section we have seen that the population coefficients can be determined by knowledge of the neutron number density n_n, the stellar temperature T, and the neutron separation energies B_n only. This fact can be used to constrain the astrophysical conditions at which the r-process can occur. From figure 4.5 one can clearly see that at least three components are needed to reproduce the observed solar r-process abundances. In this calculation we have assumed a constant value for the temperature and neutron density during the whole process, where the time-duration is given by τ_{exp}. This values are in reality time-dependent, but as long as both values are large enough, the $(n, \gamma) - (\gamma, n)$ equilibrium will redistribute the abundances within an isotopic chain instantaneously and a new equilibrium configuration will be established. After the duration time τ_{exp}, neutron-captures and photo-disintegrations are instantaneously turned off and the nuclei beta-decay back to stability. The first abundance peak located at $A = 80$, shown in Figure 4.5(a) can be reproduced with a neutron number density $n_n = 10^{20}$ cm^{-3} and a duration time $\tau_{\text{exp}} = 1.2$s. The second abundance peak located at $A = 130$ can be reproduced by $n_n = 10^{22}$ cm^{-3}, shown in the upper right panel of Figure 4.5. The third abundance peak at $A = 195$ can be reproduced by $n_n = 10^{24}$ cm^{-3} and $\tau_{\text{exp}} = 2.1$s Figure (4.5(c)). A constant temperature of $T = 1.35 \times 10^9$K was assumed for all three components. A superposition of the three components is shown in Figure 4.5(d). The superposition was performed following the procedure introduced in [KBT$^+$93]. The waiting point approximation cannot only be used to constrain the astrophysical parameters for a successful r-process. It can also be used to constrain the nuclear physics input, such as mass-models and beta-decay half-lives. A detailed discussion of the input physics is found in [FRR$^+$99].

4.3.3 A Dynamical Approach

The waiting point approximation described in the previous sections is only valid as long as neutron captures and photodisintegrations occur on much faster time-scales then beta decays. As soon as the neutron density falls below 10^{20} g/cm^3
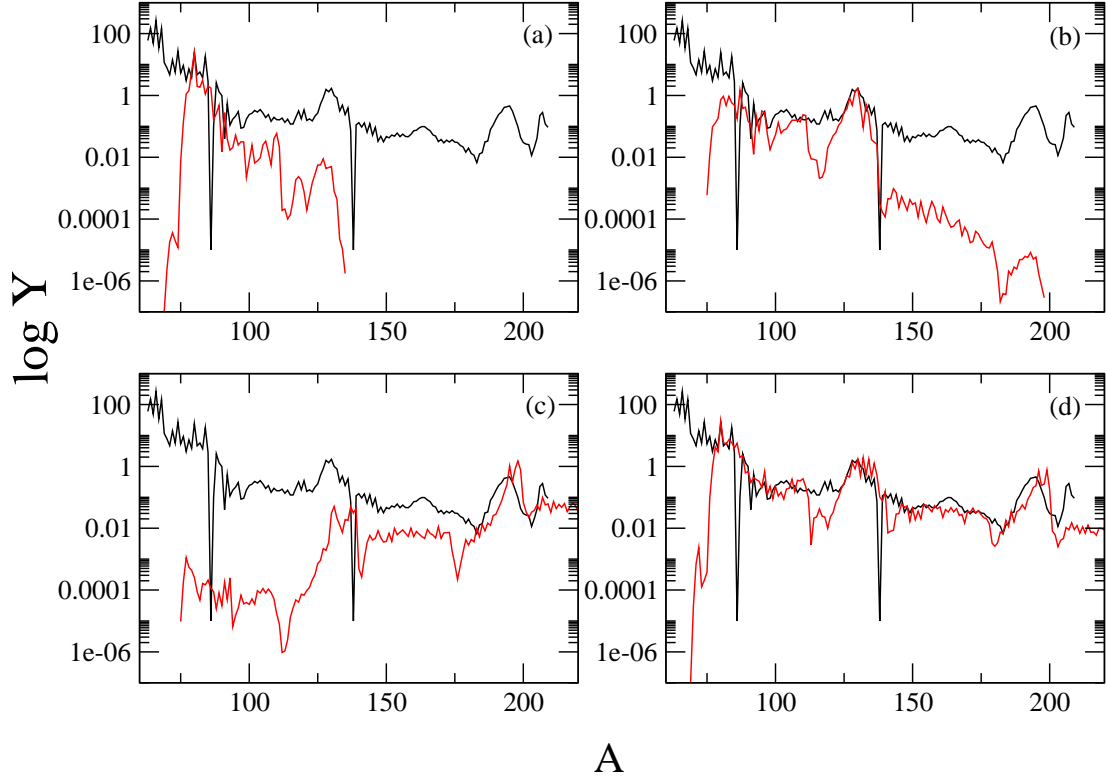
Figure 4.5: *(a)-(c): Reproduction of the A=80,130 and 195 for three different neutron number densities and exposure times, see text for details. (d) Superposition of the three components to reproduce the solar-system r-process abundances.*

the reaction rates of all three process are of the same order. Therefore all possible reactions have to be treated explicitly in the description of the nuclear network. Taking into account β-delayed neutron emission and alpha decay in additon to the reactions described in equation (4.5), the abundance change for a specific nucleus is given by

$$
\begin{aligned}
\dot{Y}(Z,A) &= n_n Y_{Z,A-1} \langle \sigma v \rangle_{Z,A-1}^{(n,\gamma)} + Y_{Z,A+1} \lambda_{Z,A+1}^{(\gamma,n)} \\
&- Y_{Z,A} \left(n_n \langle \sigma v \rangle_{Z,A}^{(n,\gamma)} + \lambda_{Z,A}^{(\gamma,n)} + \lambda_{Z,A}^{\beta} + \lambda_{Z,A}^{\beta n} + \lambda_{Z,A}^{\beta 2n} + \lambda_{Z,A}^{\beta 3n} \right) \\
&+ Y_{Z-1,A} \lambda_{Z-1,A}^{\beta} + Y_{Z-1,A+1} \lambda_{Z-1,A+1}^{\beta n} \\
&+ Y_{Z-1,A+2} \lambda_{Z-1,A+2}^{\beta 2n} + Y_{Z-1,A+3} \lambda_{Z-1,A+1}^{\beta 3n} \\
&+ Y_{Z+2,A+4} \lambda_{Z,A+4}^{\alpha} - Y_{Z,A} \lambda_{Z,A}^{\alpha} \;,
\end{aligned}
\tag{4.19}
$$

where $\lambda_{Z,A}^{\alpha}$ denotes the alpha decay rate of the nucleus (Z,A). This set of differential equations can be integrated again by the *backward* Euler scheme introduced in equation (4.15). The (linearized) abundance change per time step Δt for equation

(4.19) is then given by

$$
\begin{aligned}
\frac{\Delta Y}{\Delta t} \;=\;& n_n \langle \sigma v \rangle^{(n,\gamma)}_{Z,A-1} [Y_{Z,A-1} + \Delta Y_{Z,A-1}] + \lambda^{(\gamma,n)}_{Z,A+1} [Y_{Z,A+1} + \Delta Y_{Z,A+1}] \\
&- [Y_{Z,A} + \Delta Y_{Z,A}] \left(n_n \langle \sigma v \rangle^{(n,\gamma)}_{Z,A} + \lambda^{(\gamma,n)}_{Z,A} + \lambda^{\beta}_{Z,A} + \lambda^{\beta n}_{Z,A} + \lambda^{\beta 2n}_{Z,A} + \lambda^{\beta 3n}_{Z,A} \right) \\
&+ [Y_{Z-1,A} + \Delta Y_{Z-1,A}] \lambda^{\beta}_{Z-1,A} + [Y_{Z-1,A+1} + \Delta Y_{Z-1,A+1}] \lambda^{\beta n}_{Z-1,A+1} \\
&+ [Y_{Z-1,A+2} + \Delta Y_{Z-1,A+2}] \lambda^{\beta 2n}_{Z-1,A+2} + [Y_{Z-1,A+3} + \Delta Y_{Z-1,A+3}] \lambda^{\beta 3n}_{Z-1,A+3} \\
&+ [Y_{Z+2,A+4} + \Delta Y_{Z+2,A+4}] \lambda^{\alpha}_{Z+1,A+4} - [Y_{Z,A} + \Delta Y_{Z,A}] \lambda^{\alpha}_{Z,A} \; . \qquad (4.20)
\end{aligned}
$$

Generally, the neutron number density n_n is not constant during a time step Δt. In this case, n_n has to be treated like an independent variable. Therefore the system of non-linear differential equations has to be solved by a multi-dimensional Newton-Raphson iteration scheme, which involves an inversion of a 6000×6000 matrix at each time step. This can be avoided, by choosing the time step Δt sufficiently small to assure a constant neutron number density over the whole time step. In this case the differential equations are linear and can be written in matrix notation as:

$$
\mathbf{A} \overrightarrow{\Delta Y} = \vec{B} \; , \qquad (4.21)
$$

The matrices are given by:

$$
\begin{pmatrix}
b_1 & c_1 & & & & \\
a_1 & b_2 & c_2 & & & \\
 & a_2 & b_3 & c_3 & & \\
 & & \ddots & \ddots & \ddots & \\
 & & & a_{n-2} & b_{n-1} & c_{n-1} \\
 & & & & a_{n-1} & b_n
\end{pmatrix}
\begin{pmatrix}
\Delta Y_1 \\
\Delta Y_2 \\
\vdots \\
\\
\Delta Y_n
\end{pmatrix}
=
\begin{pmatrix}
d_1 \\
d_2 \\
\vdots \\
\\
d_n
\end{pmatrix} ,
$$

with coefficients:

$$
\begin{aligned}
a_i \;=\;& -n_n \langle \sigma v \rangle^{i}_{Z,A-1} \; , \\
b_i \;=\;& \left(\frac{1}{\Delta t} + n_n \langle \sigma v \rangle^{(n,\gamma)_i}_{Z,A} + \lambda^{(\gamma,n)_i}_{Z,A} + \lambda^{\beta_i}_{Z,A} + \lambda^{\beta n_i}_{Z,A} + \lambda^{\beta 2n_i}_{Z,A} + \lambda^{\beta 3n_i}_{Z,A} + \lambda^{\alpha_i}_{Z,A} \right) \; , \\
c_i \;=\;& -\lambda^{(\gamma,n)_i}_{Z,A+1} \; ,
\end{aligned}
$$

and

$$
\begin{aligned}
d_i \;=\;& n_n \langle \sigma v \rangle^{(n,\gamma)_i}_{Z,A-1} Y^{i}_{Z,A-1} + \lambda^{(\gamma,n)_i}_{Z,A+1} Y^{i}_{Z,A+1} \\
&- Y^{i}_{Z,A} \left(n_n \langle \sigma v \rangle^{(n,\gamma)_i}_{Z,A} + \lambda^{(\gamma,n)_i}_{Z,A} + \lambda^{\beta_i}_{Z,A} + \lambda^{\beta n_i}_{Z,A} + \lambda^{\beta 2n_i}_{Z,A} + \lambda^{\beta 3n_i}_{Z,A} \right) \\
&+ \left[Y^{i}_{Z-1,A} + \Delta Y^{i}_{Z-1,A} \right] \lambda^{\beta_i}_{Z-1,A} + \left[Y^{i}_{Z-1,A+1} + \Delta Y^{i}_{Z-1,A+1} \right] \lambda^{\beta n_i}_{Z-1,A+1} \\
&+ \left[Y^{i}_{Z-1,A+2} + \Delta Y^{i}_{Z-1,A+2} \right] \lambda^{\beta 2n_i}_{Z-1,A+2} + \left[Y^{i}_{Z-1,A+3} + \Delta Y^{i}_{Z-1,A+3} \right] \lambda^{\beta 3n_i}_{Z-1,A+3} \\
&+ \left[Y^{i}_{Z+2,A+4} + \Delta Y^{i}_{Z+2,A+4} \right] \lambda^{\alpha_i}_{Z+1,A+4} \; .
\end{aligned}
$$

The size of the matrix of the system of linear equations reduces to approximately 100×100 - essentially the number of different isotopic chains. This system can be solved relatively easy as the matrix is tridiagonal.

As the neutron abundance is considered to be constant over one timestep, it has to be recalculated explicitly after each time step utilizing the mass conservation law

$$\sum_{i,j} A_j Y(Z_i, A_j) + Y_n + X_{\text{light}} = 1 \ , \tag{4.22}$$

where X_{light} denotes the mass fraction sitting in nuclei with $Z < Z_{\text{rprocess}}^{\text{min}}$, not participating in the r-process. The neutron abundance is then given by

$$Y_n = 1 - \sum_{i,j} A_j Y(Z_i, A_j) - X_{\text{light}} \ . \tag{4.23}$$

Chapter 5

<div align="right">

The neutrino driven wind

</div>

5.1 Requirements for the r-process

Regardless of the astrophysical site, there a two provisions needed for the r-process (1) a flux of free neutrons, and (2) an abundance of seed-nuclei (typically iron-group nuclei) to capture them. A full r-process requires temperatures of about $1 - 3 \times 10^9$ K, free neutron number densities of $\geq 10^{20}$ cm^{-3}, and time scales around 1s. In addition, because the r-process builds up actinide nuclei ($A \approx 240$) from initial iron-group seed nuclei, it is necessary to have about 100 free neutrons per seed nucleus which can be converted to a neutron-to-proton ratio of up to $n/p \approx 7 - 8$. These relatively short time-scales and high temperatures and densities point towards explosive environments.

Stars heavier than about 8 M$_\odot$ live only a few million years. They are thought to end up as core-collapse (type II) supernovae when their thermonuclear fusion fuel is exhausted. Supernovae have long been the prime suspects of being the site of the r-process but it has been difficult to identify where exactly in supernovae the r-process takes place.

Because of the large neutron-to-proton ratio required, a primary site deep in the exploding star, near the mass cut, was suggested. The mass cut is the boundary that separates the matter ejected by the explosion from the matter left behind in a gravitationally bound remnant, such as a neutron star or a black hole. The r-process occurs in expanding material close to the mass cut. Early in the expansion, the nuclear reactions producing nuclei from free protons and neutrons are much faster than the expansion rate. The system reaches nuclear statistical equilibrium (NSE) under such conditions, that means all nuclear reactions, except for weak interactions, are in equilibrium. NSE is the generalized case of the previously discussed $(n, \gamma) - (\gamma - n)$ equilibrium. It is then a simple matter to compute the abundance of the nuclear species of atomic number Z and mass number A by a Saha equation. This equation gives the abundance per baryon, $Y(Z, A)$, in terms of the free neutron and proton abundances:

$$Y(Z, A) = G(Z, A) \left(\rho N_A\right)^{A-1} \frac{A^{3/2}}{2^A} \left(\frac{2\pi\hbar^2}{m_u kT}\right)^{\frac{3}{2}(A-1)} e^{B(Z,A)/kT} Y_p^Z Y_n^{A-Z} , \quad (5.1)$$

where $G(Z, A)$ is the nuclear partition function, T is the temperature, m_u is the mass of a single baryon, Y_p is the abundance of free protons per baryon, Y_n is the abundance of free neutrons per baryon, $B(Z, A)$ is the binding energy of a nucleus with atomic mass A and nuclear charge Z, N_A is Avogadro's number, and ρ is the baryon mass density. In order to determine the NSE abundances, two additional equations for the determination of the free neutron and proton abundances Y_n and Y_p are needed. These are the total mass conservation and the relation for Y_e

$$\sum_i A_i Y_i = 1 \qquad (5.2)$$

$$\sum_i Z_i Y_i = Y_e . \qquad (5.3)$$

The nuclei that dominate the abundance distribution in NSE depend on the temperature, the density of the material, and on the binding energies: (i) high densities favor large nuclei due to the ρ^{A-1} dependence in equation (5.1). High temperatures favor light nuclei, since the Planck distritution contains high energy photons which photodisintegrate heavy nuclei. This is reflected by the $kT^{-3/2(A-1)}$ dependence in equation (5.1). Intermediate conditions favor tightly bound nuclei with the highest binding energies.

Here we will introduce two generic scenarios for producing an r-process in expanding and cooling matter, originating from some explosive event such as a supernova. Initially, the matter is assumed to be hot and dense enough to be in NSE, where the subsequent freeze-out is dependent upon the entropy S and the net electron fraction of matter Y_e. For matter at high entropy ($S \geq 20 k_B$), the entropy is dominated by radiation and is proportional to

$$S \propto \frac{T^3}{\rho} . \qquad (5.4)$$

Thus, for a given temperature, the density of the expanding matter is related inversely to its entropy. The NSE abundance distribution shifts to heavy nuclei when the temperature falls to T_{rec}, which is called the recombination temperature. The value of T_{rec} is only weakly dependent on the density (see equations (5.1) and (5.4)) and is ≈ 0.5 MeV. The density at which this recombination temperature is reached depends on the entropy of the material. Nucleons expanding at low entropy will tend to combine to form nuclei already at high densities, whereas nucleons expanding at high entropy will tend to combine to form nuclei at low densities. This is the key difference leading to two very different r-process scenarios.

In the first scenario, sometimes called the low entropy scenario, all protons are bound into iron-group nuclei by the time the charged-particle reactions freeze out. If the neutron to proton ratio is small ($Y_e \geq 0.3$), the neutrons are also bound into nuclei. Some neutron rich nuclei such as ^{48}Ca, ^{58}Fe, etc. may be produced in this way, but no r-process occurs. If the neutron to proton ratio is large, however, free neutrons will be available for capture on iron-group NSE seed nuclei even after the charged particle reactions have ceased, so an r-process can occur. We have seen that to make actinide nuclei about 100 free neutrons per seed nucleus are needed, resulting in a neutron to proton ratio of up to 7-8 which yields an electron fraction of $Y_e = 0.1$.

Where is such material to be found, and what kinds of explosive events would cause this material to expand? As mentioned earlier, one such site is just outside the mass cut of a core collapse supernova. Matter near but outside the mass cut of a core collapse supernova would experience hot, dense and low entropy conditions during the initial core collapse and then undergo rapid expansion during the supernova explosion. Detailed calculations of this scenario were made by [HKT76].

A problem with r-process sites occuring near the mass cut is that they predict the synthesis of too much r-process material. At least the outer 0.1 M$_\odot$ of the neutron-rich core material must be ejected in order to have Y_e as small as 0.1. Most of this material would become r-process material. Consider the mass of r-process nuclei in the Galaxy. Using abundances extracted from meteorites and from the Sun, we can infer that the mass of r-processed nuclei in the Galaxy is 2×10^{-7} M$_\odot$ (from the data in Anders & Grevesse, [AG89]). If the mass of our Galaxy is 1.5×10^{11} M$_\odot$, the mass of r-process material in our Galaxy is about 10^4 M$_\odot$. For the event rate, assume that the astrophysical site is a core collapse supernova. The rate of core collapse supernovae in our Galaxy is between $0.1 - 0.01$ per year [Tam82] and the Galaxy if about 10^{10} years old. Therefore, there have been some 10^8 to 10^9 supernovae in our Galaxy's history. If each of these supernovae produces r-process material, we expect each supernova to make 10^{-5} to 10^{-4} M$_\odot$ of r-process nuclei - which is clearly in contradiction with the r-process calculations of [HKT76]

Another possibility is that only certain rare supernovae eject neutron-rich matter into the interstellar medium. For example, it may be that only a small fraction of supernovae have sufficiently high rotational rates and magnetic fields so that magnetohydrodynamical instabilities allow ejection of r-process matter [LW70], [SS82]. Yet another possibility is that the r-process results from rare interacting binary systems such as the tidal disruption of a neutron star by a black hole companion or binary neutron star coalescence [Mey89], [FRT99], [ORT02]. However, the presence of short-lived radioactive r-process nuclei such as ^{129}I ($\tau_{1/2} = 1.7 \times 10^7$ yr) in the early solar system indicates that the site which produces the r-process may not be that rare. Thus, all low entropy sites for the r-process pose problems.

The second scenario, sometimes referred to as the high entropy scenario, be-

gins with matter at a high enough temperature to be in NSE, but at a low enough density for Y_e to differ only little from 0.5. We have seen before that NSE assumes that all nuclear reactions via strong and electromagnetic interactions are very fast when compared with dynamical timescales. The bottlenecks leading from α-particles to heavier nuclei are the reactions

$$3\alpha \rightarrow^{12} C + \gamma \tag{5.5}$$

or

$$\alpha + \alpha + n \rightarrow^{9} Be \ , \tag{5.6}$$

followed by

$$^{9}Be + \alpha \rightarrow^{12} C + n \ . \tag{5.7}$$

Heavier elements are formed from α particles via the above reactions, followed by $^{12}C(n,\gamma)^{13}C(\alpha,n)^{16}O(\alpha,\gamma)^{20}$Ne, and so on. At low densities the the three-body reactions (5.5) and (5.6) are slow. A breakdown of NSE occurs when a temperature of $\approx (5-7) \times 10^9$K and densities of $10^4 - 10^5$ g/cm^3 are reached, i.e. when the cooling time-scale becomes shorter than the time-scale for NSE to be maintained. The consequence of this breakdown is that many α particles survive the expansion, resulting in an α-rich freeze-out, because the triple-α as the $2\alpha + n$ reaction is not fast enough to convert all α particles to heavier nuclei. As temperature and density decrease, charged particle reactions cease, whereas neutron-capture reactions continue. At this time only a small number of intermediate mass seed nuclei has been produced. Because the number of seed nuclei produced is small, only a moderate number of free neutrons are needed to drive an r-process. For a high entropy r-process, however, we have two problems. Again, the first concern is, how to get 10^{-4} M$_\odot$ per supernova. The second problem is where in the supernova to find sufficiently large entropies. It is crucial for the whole process that the entropy is large. If the entropy is too small, too many α particles can recombine resulting in too many seed nuclei per neutron and preventing an r-process. Large entropy implies a high temperature and low baryon density. Generally in supernovae, high temperatures are associated with high density, so it is difficult to find a region where, the temperature is high but the density is comparatively low. In the next section we will describe a scenario which involves the rapid expansion of high-entropy material and quite naturally satisfies the constraint that only 10^{-5} to 10^{-4} M$_\odot$ the r-process material are produced per core collapse supernova.

5.2   Clues from abundance observations

A lot of knowledge regarding the formation of the heaviest elements has been gained from high-resolution spectroscopic observations of stars in our Galaxy,
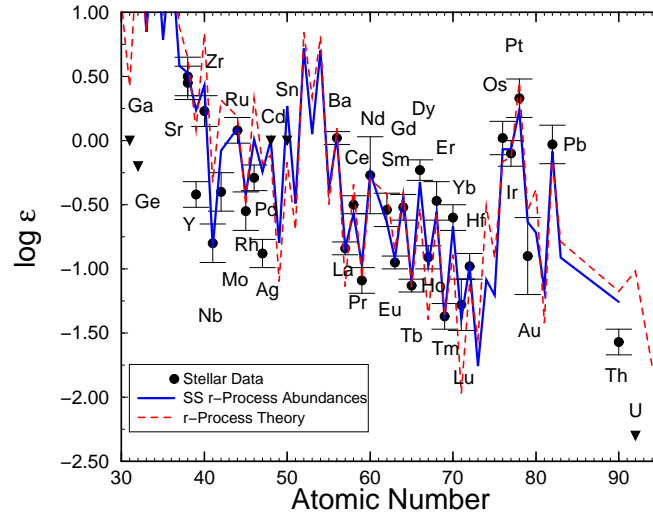
Figure 5.1: *Elemental abundances in the halo star CS22892-052 compared with scaled solar system r-process abundances [SCL].*

especially in so-called halo stars. A star's surface abundance of the various elements reflects the interstellar matter from which the star is formed. The halo stars circling in the galaxy in highly eccentric orbits are among the oldest stars. By comparison with the Sun, they have very low Fe abundances.

The s-process elements are produced by low-mass stars that live for billions of years before they end their lives as white dwarfs. Significant s-process material had not yet been ejected into the interstellar medium when the halo stars were born. On the other hand, clear signatures of r-process elements are found in halo stars. This indicated that r-processing predates the s-process. Therefore, the first generation of high-mass stars that ended their short lives as supernovae would be the producers of r-process material.

One of the best studied halo stars is called CS22892-052. Its ratio of iron to hydrogen is less than a thousandth of the Sun. The most recent abundance data for CS22892-052 [SCL] are shown in Figure 5.1. Fifty-seven elements have been observed in this star 15 000 light years from us. No other star, except the Sun, had had so many of its elements identified.

For comparison, a scaled curve of r-process elemental abundances in the solar system is superposed on the CS22892-052 data in Figure 5.1. One deduces the r-process contributions by subtracting the calculated s-process component from the observed total abundances. The solar system curve shown in Figure 5.1 is scaled to compensate for the Sun's enormously greater metallicity. It is normalized to Mo. For elements heavier than Ba, there is a striking agreement between the r-abundance ratios in the halo star and the scaled solar system r-process distribution. This fact allows to draw some conclusions. First of all, the presence
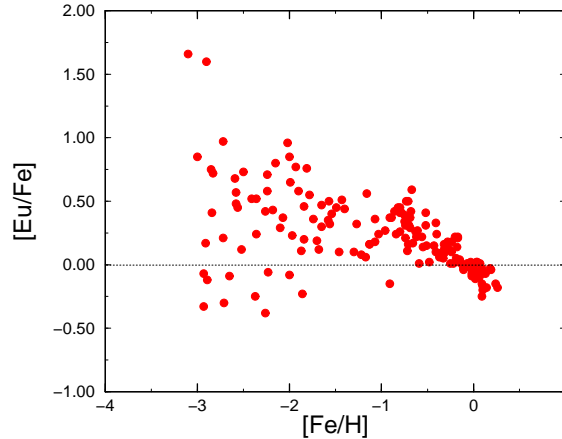
Figure 5.2: *The ratio [Eu/Fe] is plotted as a function of the metallicity from various surveys of halo and disk stars. The dotted line represents the solar value. Adopted from [SCL].*

of these elements in the halo stars demonstrates the operation of the r-process during the earliest epochs of Galactic history, presumably in massive stars that ended their lives as supernovae. The agreement in the abundance ratios demonstrates the robustness of the r-process. The process has clearly been operating in much the same manner over many billions of years. Wherever and however the r-process operates, it appears to be uniform and well confined in astrophysical parameter space.

Figure 5.1 also shows that the abundances of the light neutron capture elements, from Z=40-50, generally fall below the r-process curve that fits the heavier elements so well. This difference might be telling us that the r-process sites for elements above and below Ba are somehow different. As mentioned above, possible alternative sites for the r-process include neutron-star binaries as well as supernovae, or perhaps just different astrophysical conditions in different regions of a single core-collapse supernova.

Neutron star mergers are much rarer than type II supernovae. The two processes eject different amounts of r-process material into the galaxy. The differences between them enter into the enrichment pattern of r-process elements during galactic chemical evolution. Additional clues to the nature of the r-process and the identification of its primary sites have come from recent studies of chemical evolution [ASTQ04], typically shown as elemental abundance trends as a function of metallicity. Stellar iron abundances very roughly can be seen as a time-line but at very early times mixing of ejected matter with the interstellar medium is not efficient yet and a (large) scatter can occur. This scatter diminished dramatically at higher metallicities. The amount of scatter at a given metallicity could also be interpreted as a measure for the frequency of the responsible nu-

cleosynthesis events. Observations indicate that for the r-process production of (Ge), Zr, and Eu we might be witnessing decreasing event statistics, i.e., a smaller number of sites which create these elements. Figure 5.2 shows a least-square fit to the [Eu/Fe] abundance data. The solid line has several interesting features. First, there is a downward trend at higher metallicities, being mostly a result of increasing amounts of iron being deposited in the Galaxy at late times by Type Ia supernovae. The average Eu/Fe ratio behaves very similarly to other elements from SNe II explosions (like O,Si,Ca, etc.) but the scatter implies a much lower r-process frequency than typical for those elements.

A reproduction of the Eu/Fe abundance data has been attempted by a number of research groups. Neutron star mergers (with a much lower frequency that SNe II) would produce a larger scatter in [Eu/Fe] like the observed one but only enter at too high metallicities when already too much Fe is produced by SNe II. Therefore, while not necessarily excluding other sites, the [Eu/Fe] data has been satisfactorily reproduced by chemical evolution models that assume core-collapse supernovae to be the primary r-process sites, but with a smaller frequency (possibly limited progenitor mass range) for the supernovae contributing to the r-process production.

In this work, SNe II are assumed as a possible site for the r-process. The nucleosynthesis details are discussed in the next section.

5.3   The model

Woosley and Hoffman [WH92] first proposed that the r-process occurs in winds from nascent neutron stars. The death of a massive star is a spectacular event - one of the most powerful explosions known to occur in the universe, a supernova. The physics of events leading to and immediately following the core collapse of a massive star has been under investigation for the last 30 years.

During the final stages of the thermonuclear evolution of a massive (8-50 $M_\odot$) star an iron core forms in its central region (see chapter 5 for details).

Matter is added to the core by silicon burning in the surrounding layer. Once the core exceeds the Chandrasekhar mass of $1.44(2Y_e)$ $M_\odot$, it becomes hydrodynamically unstable and starts contracting since additional energy is lost by fusion of heavy nuclei and neutrino radiation, the contraction turns into a collapse. When the central density exceeds nuclear matter density, the pressure rises rapidly and the inner part of the core decelerates abruptly and rebounds. A hydrodynamic shock wave is created at the outer edge of the rebounding inner core and begins to propagate outward though the outer part of the iron core. The rising temperature in the shock leads to photodisintegration of nuclei into nucleons. This disintegration, starting from nuclei near ^{56}Fe, consumes 8.8 MeV per nucleon and therefore decreases the energy available to drive the shock. As a result of this energy loss, the shock stalls at a radius about 200 km.

At lower densities neutrinos are free to stream away. At high matter density $(10^{11}\text{g/cm}^3\text{-}10^{12}\text{g/cm}^3)$, neutrinos are trapped. A neutrino-sphere separates the region where neutrinos are trapped from the region where they stream freely for a given neutrino flavor. Radius and density of the neutrino-sphere depend very strongly on the neutrino energy because of the energy dependence of the neutrino interaction cross sections. The neutrino-sphere is at larger radius (lower density) for higher-energy neutrinos. Since neutrinos are represented by some spectral distribution, a suitable average must be take to define a unique neutrino-sphere. During the collapse protons capture electrons producing neutrons and electron-neutrinos. Because of the short mean-free path of the neutrinos in high-density matter they remain trapped within the radius of the neutrino-sphere. Similar to the photo-sphere in stars neutrinos can escape only after they reach the radius of the neutrino-sphere. After the neutrinos are trapped and the neutrino-spheres established electron-capture on protons and neutrino-captures on neutrons are in equilibrium. The collapsing inner iron core forms a hot proto-neutron star because of the released gravitational binding energy of several 10^{53} ergs. This energy is radiated in the form of neutrinos because at this temperatures electron pairs transform to neutrino pairs,

$$e^+ + e^- \rightarrow \nu + \bar{\nu} \ . \tag{5.8}$$

All types of neutrinos are produced in this process. To an observer from the outside they are emitted from the respective neutrino-spheres. When the hydro-dynamic shock-wave from the core-bounce traverses the neutrino-sphere a second neutrino-pulse arises due to the increased temperature. In the shock heated material of the core behind the shock front, the temperature is very high, of the order of 10 MeV or more. Again, electron pairs transform into neutrino pairs producing all types of neutrinos. The net production stops when the neutrino density has become high enough to drive the inverse process to equation (**??**), balancing the direct process. About 50-100 milliseconds after shock stagnation, a generic thermodynamic profile is established inbetween the neutrino-sphere and the shock. ν_e and $\bar{\nu}_e$ absorption in matter dominates near the shock and cooling by the inverse process dominates near the neutrino-spheres. The radius at which heating and cooling balance is called the gain radius [BW85]. Between the gain radius and the shock, neutrino heating establishes an unstable entropy gradient that invokes convection. This is referred to as neutrino-driven convection, bringing high-entropy matter to the shock front and thereby replenishing its energy. Moreover, because of the structure of the pre-supernova star, the density of the accreted material decreases with time and the post-shock pressure eventually becomes radiation dominated. Given sufficient neutrino heating, the position of the shock destabilizes and begins to move out. A critical neutrino heating rate, depending on the mass accretion rate, is necessary to generate an explosion. On a time-scale from several tens of milliseconds to about half a second, it is believed that the neutrinos streaming out from the newborn neutron star can deposit sufficient energy (0.2

M$_\odot$ of energy are released by the core in about 10 seconds) to revive the shock and initiate the final explosion of the star. This is the neutrino-driven delayed explosion mechanism, originally suggested by [CW66], rediscovered [BW85], and developed since then by many others, e.g. [LMT$^+$01]. It has yet to be confirmed by detailed simulations. Neutrino heating of material behind the shock operates predominately by absorption of electron neutrinos on neutrons

$$\nu_e + n \rightarrow p + e^- ~, \tag{5.9}$$

electron anti-neutrinos on protons

$$\bar{\nu}_e + p \rightarrow n + e^+ ~, \tag{5.10}$$

and, at very high entropy, by neutrino-electron scattering

$$\nu_e + n \rightarrow \nu_e + n ~, \tag{5.11}$$

and neutrino-anti-neutrino annihilations

$$\nu_e + \bar{\nu}_e \rightarrow e^+ + e^- ~. \tag{5.12}$$

Behind the outgoing shock an extended, rapidly expanding region of low density and relatively high temperature develops, which separates the compact central remnant from the exploding stellar envelope. This neutrino-heated region is sometimes referred to as the hot bubble. After the explosion, the persistent (about 10 seconds) heating of the matter near the neutron star's surface by neutrino fluxes (reactions (5.9) - (5.12)) from deeper layers drive a continuous mass flow or wind into the hot-bubble region. This wind is analogous to the solar wind and is referred to as a neutrino-driven wind. It is in this neutrino driven wind that the r-process may occur.

The neutrino-driven wind site for the r-process may have some deficiencies, especially the need for very high entropies that might be hard to obtain [WJT94], [TWJ94], [QW96], [HWQ97] and [WKMO01]. On the other hand, it has several attractive features. For example, the amount of r-process material blown off by the wind, assuming that an r-process does indeed occur, is consistent with the $10^{-5} - 10^{-4}$ M$_\odot$ expected from each supernova [WWMH94]. It is also a natural site for the high-entropy α-rich freeze-out described above.

5.4   Nucleosynthesis in the Wind

As we have seen above the neutrino-driven wind from a protoneutron star naturally provides the required high entropy condition of the hydrodynamically expanding environment. The next step is to determine whether or not an r-process can actually occur there.
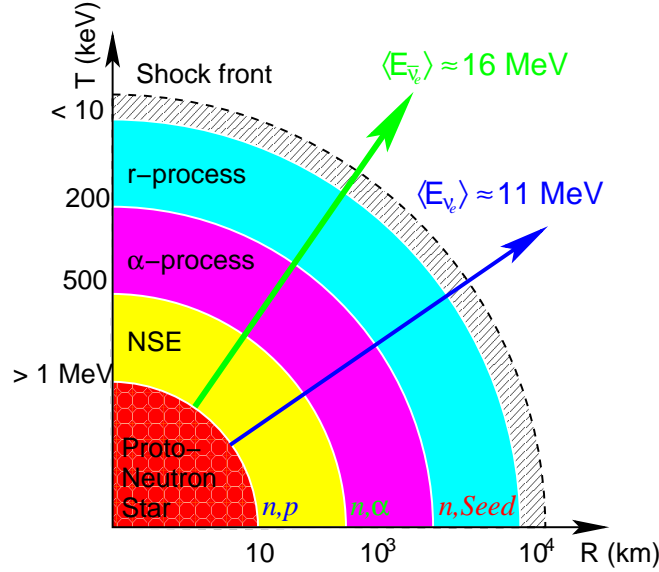
Figure 5.3: *Sketch of the different nucleosynthesis processes occurring in the neutrino driven wind scenario. Courtesy of G. Martinez-Pinedo.*

Neutrinos from the cooling neutron star play a very important role in the determination of the electron fraction Y_e and dynamics of the wind. First, the neutrinos set the neutron richness of the wind material. The matter in the surface layer of the protoneutron star is in reactive equilibrium with the neutrino fluxes emerging from below. The net electron fraction is low near the neutron star surface ($\rho \approx 4 \times 10^{11}$ g/cm^3). This is because the material is in weak equilibrium with the degenerate electrons via reaction (5.9) and (5.10) and their inverses. As the wind expands, it can be shown [QW96] that the rates of reactions (5.9) and (5.10) decrease proportionally to $1/r^2$, where r is the distance of a fluid element of the wind from the center of the neutron star. On the other hand, their reverse rates decrease proportionally to $1/r^4$. Consequently, these reverse reactions die out rapidly as the material flows outward and quickly cease to influence the readjustment of Y_e. If the fluxes and energies of the ν_e's and $\bar{\nu}_e$'s are equal, the value of the net electron fraction Y_e would be slightly larger than 0.5 because the mass of the proton is slightly less than that of the neutron, favoring reaction (5.9). But the $\bar{\nu}_e$'s have a longer mean free path and decouple from the matter deeper in the neutron star where it is hotter. The result is that they are more energetic than the ν_e's and reaction (5.10) is favored. This necessarily makes the material neutron rich.

The net neutrino heating of the wind raises its entropy. As stated above, the change of temperature with density as the material expands is well characterized in terms of the entropy of the material, which also serves as a good measure of the nucleosynthesis. The net heating of a fluid element in the wind as it lifts

off the surface of the neutron star is governed by the heating due to neutrino absorption, (5.9) and (5.10), and cooling due to the inverse of these reactions, as has been shown above. The initial net heating is slow because the matter temperature is nearly the same as the temperature of the neutrinos and heating and cooling approximately balance. As the mass element moves out and expands the temperature of the matter tends to decrease adiabatically. Since the cooling rate is a sensitive function of the matter temperature, the cooling rate falls off more rapidly than the heating rate. The matter begins to heat. The entropy therefore rises and can reach values of 200 k_B per baryon or more before neutrino interactions with the wind material freeze out. These are the values required for a high-entropy r-process.

5.5 Thermodynamics in the high entropy wind

In the previous discussion we have seen that the neutrino-driven wind might be a possible site for the r-process. In this work we will use the so-called hot-bubble approximation, where the material expands with constant entropy and expansion velocity, instead of calculating the nucleosynthesis in a detailed core collapse simulation. There are two reasons why we chose this approach: (1) Present day core collapse SN simulations can follow the time-evolution of the expansion only up to a limited time; (2) The late-time entropy profiles in realistic simulations become constant and the system performs an adiabatic expansion. Therefore, the material blown off from the protoneutron star by the neutrino wind can be approximated by a hot bubble expanding with a constant velocity.

The entropy S in a low density and high temperature environment is radiation dominated. At such conditions the radiation entropy is given by

$$S_\gamma = \frac{4}{3} a \frac{T^3}{\rho} \; , \tag{5.13}$$

where T denotes the temperature, a the Stefan-Boltzmann constant, and ρ the density of the environment. Electron and positron pairs have to be taken into account in the calculation of the total entropy of the system at such high temperatures. Their entropy is given by

$$S_{e^+e^-} = \frac{7}{4} S_\gamma = \frac{7}{3} a \frac{T^3}{\rho} \; , \tag{5.14}$$

which leads to the total entropy

$$S = S_\gamma + S_{e^+e^-} = \frac{11}{3} a \frac{T^3}{\rho} \; . \tag{5.15}$$

As mentioned above, this expression is only valid in the high temperature regime. The matter temperature will decrease as it expands. For low temperatures (temperatures where the corresponding energies are comparable to the rest-masses

of the electrons and positrons), the electron and positron contributions become negligible. In this case the entropy cannot be described by equation (5.15) and therefore has to be replaced by an expression which takes into account the transition from the radiation- to the matter-dominated regime:

$$S = \frac{4}{3}a\frac{T^3}{\rho}\left[1 + \frac{7}{4}f(T_9)\right] , \qquad (5.16)$$

where the fit-function f is given by [TWJ94]

$$f(T_9) = \frac{T_9^2}{T_9^2 + 5.3} . \qquad (5.17)$$

Evaluating all constants and expressing the baryon density in units of 10^5 g/cm^3, leads to

$$S = 1.21\frac{T_9^3}{\rho_5}\left[1 + \frac{7}{4}f(T_9)\right] , \qquad (5.18)$$

which can be solved for the baryon density:

$$\rho_5(t) = 1.21\frac{T_9^3}{S}\left[1 + \frac{7}{4}f(T_9)\right] . \qquad (5.19)$$

The temperature of the system can be derived by relating the volume of the expanding bubble to its radius. The relation is given by

$$V(t) = \frac{4}{3}\pi R(t)^3 = \frac{4}{3}\pi(R_0 + \dot{R}t)^3 , \qquad (5.20)$$

which, assuming an adiabatic expansion of the bubble, can be used to derive a relation between the temperature T and the volume:

$$T(t) = T_0\left(\frac{V_0}{V(t)}\right)^{\gamma-1} , \qquad (5.21)$$

where the adiabatic index for radiation dominated matter is given by $\gamma = \frac{4}{3}$. Inserting equation (5.20) in (5.21) yields

$$T(t) = T_0\frac{R_0}{R_0 + \dot{R}t} . \qquad (5.22)$$

Chapter 6

Results

6.1 Standard Calculation

As described in the previous chapter, we consider the high-entropy bubble as a generic model for the r-process. To summarize shortly, neutron-rich material initially composed of free nucleons at high temperatures ($T_9 \approx 9$) adiabatically expands and cools. After, for $Y_e < 0.5$, nearly all the protons are assembled into α-particles at $T_9 \approx 5$, an α-process occurs to burn the α-particles into heavy nuclei. The α-process stops when charged-particle reactions freeze-out at $T_9 \approx 2.5$. The heavy nuclei produced at the end of the α-process then become seed nuclei for the subsequent r-process with the remaining neutrons.

We do not intend to account for the full detail of the r-process, such as the final abundance distribution, which becomes meaningful only in the context of a consistent astrophysical model. The goal of this work is to investigate if and to which extend neutrino-induced, neutron-induced, and beta-delayed fission influence the final abundance pattern.

In order to study the various fission modes, we have used the seed distributions for various entropies of [Far05]. These entropies were chosen in such a way to reproduce the solar r-process abundances, in particular, every entropy component (given in units of k_B) was responsible for the production of a certain mass-range of the observed distribution:

- $S_1 = 20$, contributes mostly to the mass range $A = 63 \ldots 99$.

- $S_2 = 165$, contributes mostly to the mass range $A = 100 \ldots 120$.

- $S_3 = 190$, contributes mostly to the mass range $A = 121 \ldots 140$.

- $S_4 = 230$, contributes mostly to the mass range $A = 141 \ldots 180$.

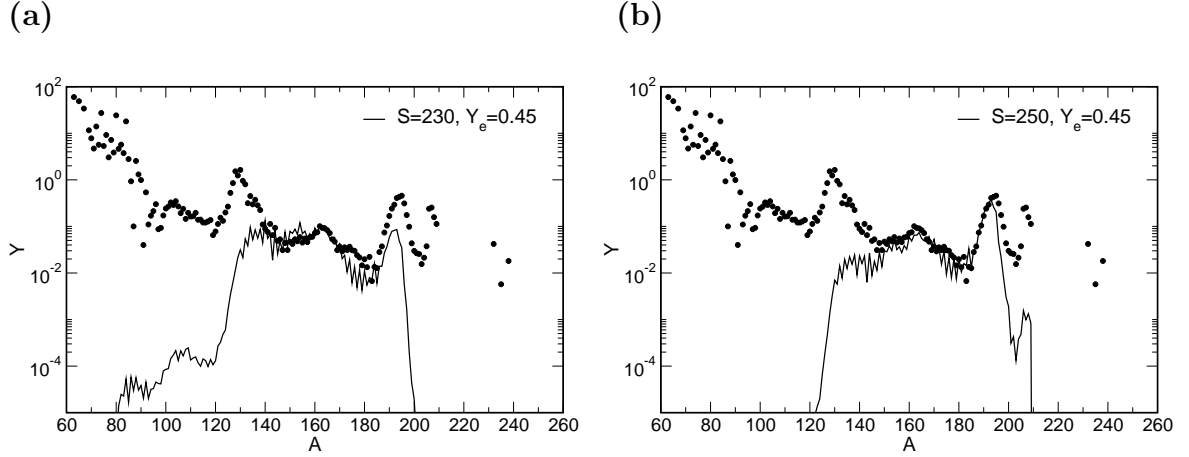- $S_5 = 260$, contributes mostly to the mass range $A = 181 \ldots 200$.

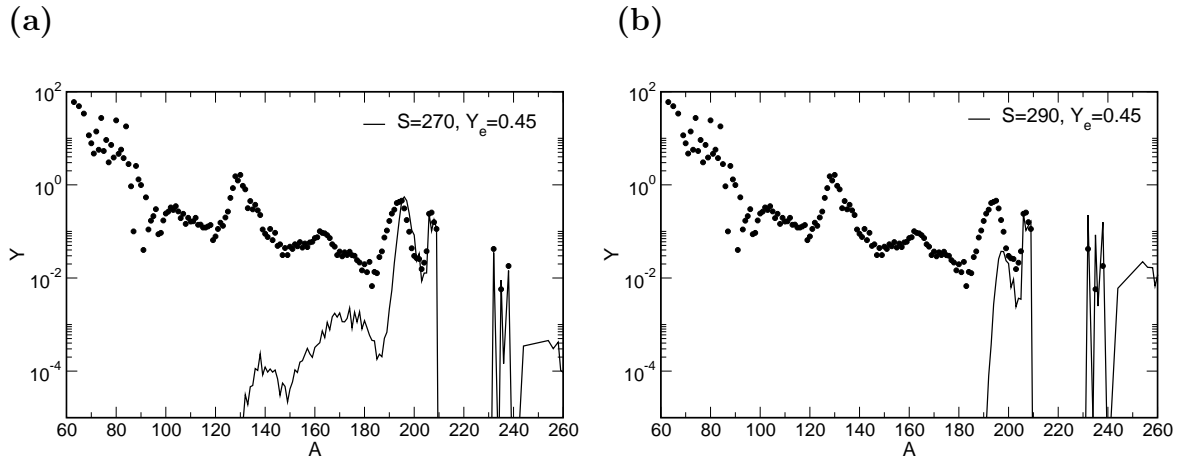**(a)**   **(b)**

Figure 6.1: *Abundance pattern of r-process nucleosynthesis for two different entropies after decay of unstable nuclei: (a) $S_1 = 230$ (b) $S_2 = 250$. Both curves are scaled to match the solar abundance distribution for $A = 162$ and $A = 180$, respectively.*

- $S_6 = 290$, contributes mostly to the mass range $A = 201 \ldots 238$.

Here, for an expansion velocity of v_{exp}, we have focused in this work only on entropies $S \geq 230$ as they only contribute to masses heavier than $A \geq 200$ - the mass regime where fission, independent of the particular mode, becomes important. Finally, we have chosen four entropies ($S_1 = 230, S_2 = 250, S_3 = 270$ and $S_4 = 290$) to study the influence of fission.

The input files of our calculations were essentially the same as in [Far05]. Neutron-capture rates were calculated in the framework of a statistical model with the so-call NON-SMOKER code of [RT01]. The theoretical beta-decay half-lives and the probabilities for beta-delayed one, two, or tree neutron emission were calculated by [MPK03], using a QRPA code including the Gamow-Teller and first-forbidden transitions. Experimental half-lives [Kra] were added where available, and finally the masses were taken from a microscopic-macroscopic approach [AP95]. Photo-disintegration rates were calculated by applying the detailed balance relation derived in chapter 4.

One important point to note while discussing the input files is that the theoretical neutron capture rates of [RT01] were only calculated up to $Z = 83$. The neutron capture rates for nuclei with $Z > 83$ were set to zero. While this does not effect much the calculations of [Far05] (in their calculations, nuclei with $A \geq 250$ spontaneously fissioned with 100% efficiency), it has a severe impact on our calculations as we are interested in fission which operates just in that mass regime. The rates up to $Z = 83$ were taken from [RT01] and for $Z > 83$ we applied the newly calculated neutron-capture rates of [PKP$^+$05] which also include the (n, f) channel.

(a) **(b)**

Figure 6.2: *Abundance pattern of r-process nucleosynthesis for two different entropies after decay of unstable nuclei: (a) $S_1 = 270$ (b) $S_2 = 290$. Both curves are scaled to match the solar abundance distribution for $A = 195$ and $A = 206$, respectively.*

The above sequence of entropies was used as a set of benchmark calculations to study the effect of different fission modes. The following sections will discuss each fission mode channel separately and compare the results to these benchmark calculations.

Standard expansion parameters

In order to study the new effects of fission reactions in the r-process, we have used the same expansion parameters as described in [FRR$^+$99] in order to separate dynamical effects from the new physical input. We values which were used in all calculations were:

Y_e	R_0	$\dot{R} = v_{exp}$
0.45	130km	7500 km/s

6.2 The influence of neutrino-induced fission

Recently, [Qia02] suggested that the neutrino-induced fission might be the origin of the patterns observed in the r-process abundances in low metallicity, old galactical halo stars [CHB01]. As can be seen from Figure (6.3, the observed abundances in CS31082-001 and CS22892-052 [SCL] follow approximately the same pattern except for Zr, Ba and Os which clearly differ for the two halo stars. The mass numbers for those r-process elements are A=92 for Zr, A=132 for Ba and A=192 for Os. [Qia02] proposed that fission, induced by charged-current neutrino reactions, occurs after the r-process freeze-out while the decay of progenitor
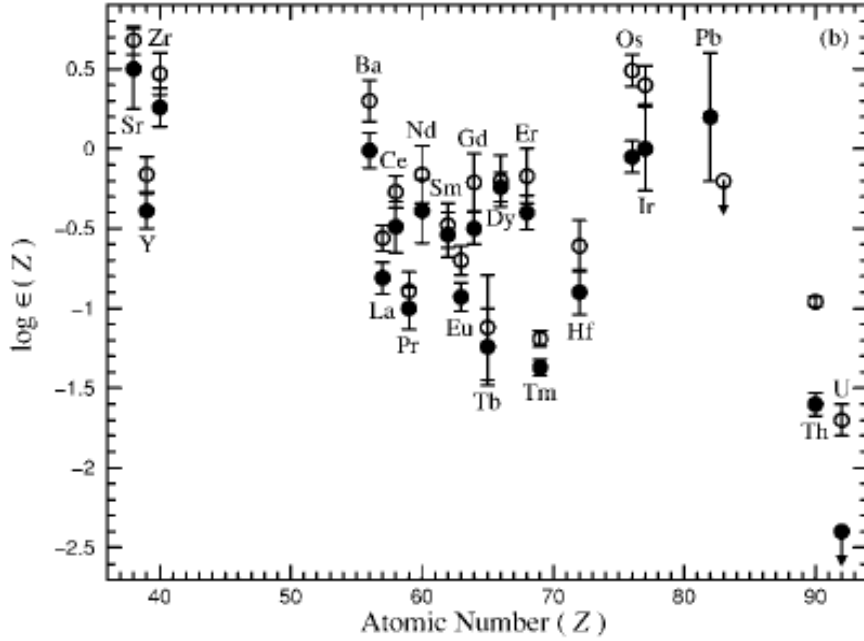
Figure 6.3: *Data for CS 31082-001 (open circles) compared with data for CS 22892-052 (filled circles) adopted from [Qia02].*

nuclei back to the valley of stability might be responsible for the enhancement of the observed abundances. Therefore, neutrino-induced reaction rates and mass and charge distributions have to be calculated to prove this assumption. First calculations of neutrino-induced fission cross sections have been performed by [KLF04] and have been extended and improved by [KZK+05]. In this thesis the updated reaction rates of [KZK+05] are used and incorporated in the r-process code.

The approach of [KZK+05] is based on a two-step description of neutrino-induced fission. The initial step of the process, i.e. the excitation of daughter levels by the (ν_e, e^-) reaction is described within the Random Phase Approximation (RPA). This is reasonable as for supernovae ν_e neutrinos the (ν_e, e^-) cross sections are dominated by Fermi and Gamow-Teller (GT) transitions, whose total strengths and multipols are quite well reproduced by the RPA. Compared to [KLF04], the improvement of [KZK+05] lies in the treatment of the decay of excited levels in the daughter nucleus. [KZK+05] have used the statistical code ABLA [GS91] which is adopted especially for the description of fission and particle decays at energies that are of interest in neutrino-induced fission.

The ABLA code is a de-excitation code that describes the competition between particle evaporation and fission, and (in case of fission) calculates the mass and charge distributions of the fission fragments, for details see [KZK+05], [GS91].
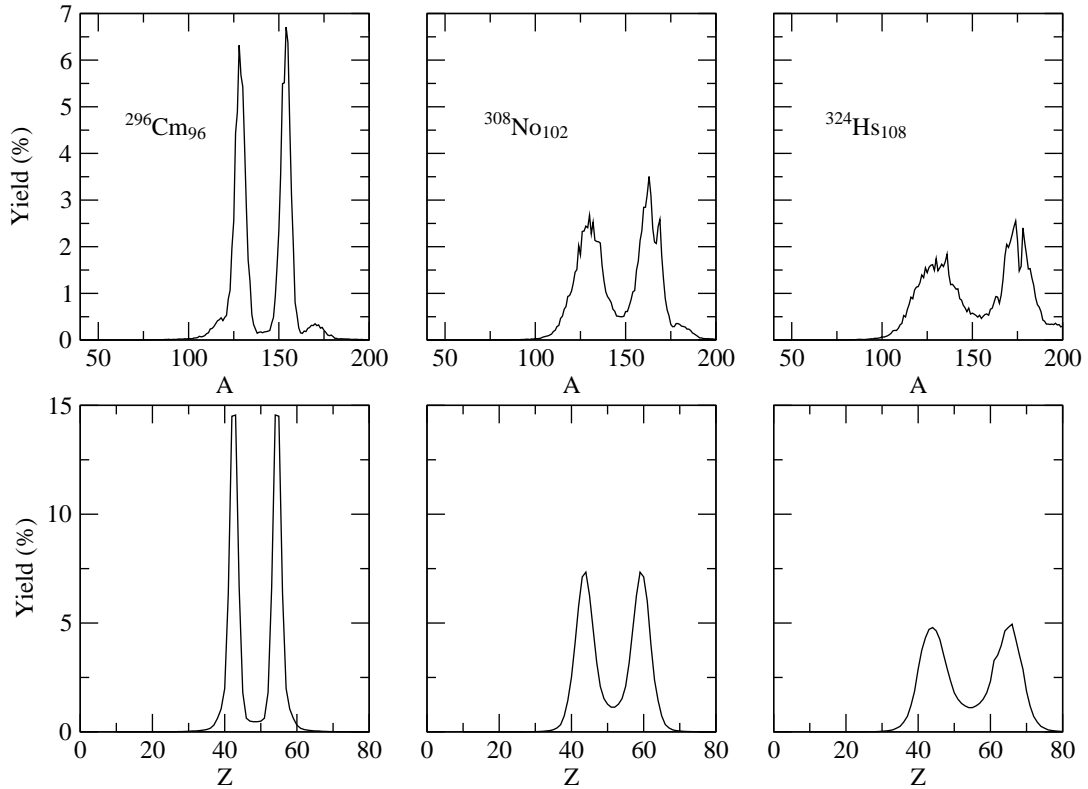
Figure 6.4: *Mass (top) and charge (bottom) distributions of fission fragments produced in (ν_e, e^-) reactions on some selected progenitor nuclei along the r-process path, taken from [KZK$^+$05].*

In case of heavy, very neutron-rich nuclei, neutron emission and fission are the most dominant decay modes, and consequently, they determine the distribution of final residues (branchings into the proton and α channels are negligible due to the relatively high thresholds). The competition between the dominant decay modes (fission, neutron evaporation) in a neutrino capture-excited daughter is governed by the relative values of the fission barrier B_f and the neutron separation energy S_n, which were taken from the compilations of [Sie86] and [MPRT00] respectively.

One of the main results of [KZK$^+$05] is that for r-process nuclei with $Z < 94$ neutrino induced fission is almost negligible. On the contrary, neutrino-induced fission dominates the r-process nuclei with $Z \geq 96$. As mentioned above, the charge and mass distributions of the fission fragments strongly depend on the difference $B_f - S_n$. Figure (6.4 shows the mass and charge distribution for neutrino-induced fission on some selected progenitor nuclei on the r-process path. A pronounced double-hump structure with centers at A_l and A_h was found. The lower peak corresponds to the mass range around $A_l \approx 130$, the second one is centered at mass numbers A_h clearly below $A - A_l$ due to the evaporation of a significant

number of neutrons. In this thesis we will study the effects of neutrino-induced fission in the r-process for the first time. We will discuss its importance in comparison with beta-delayed and neutron-induced fission modes.

Calculation of the neutrino-induced rates

Neutrino-induced reaction rates λ_ν^X can be calculated by

$$\lambda_\nu^X = \mathcal{F}_\nu \langle \sigma \nu^X \rangle \ , \tag{6.1}$$

where $\mathcal{F}_\nu$ denotes the neutrino flux and $\langle \sigma \nu^X \rangle$ is the energy-averaged neutrino cross-section. X stands for one of these reactions:

- $(Z, A) + \nu \rightarrow (Z + 1, A) + e^-$

- $(Z, A) + \nu \rightarrow (Z + 1, A - 1) + e^- + n$

- $(Z, A) + \nu \rightarrow (Z + 1, A - 2) + e^- + 2n$

- $(Z, A) + \nu \rightarrow (Z + 1, A - 3) + e^- + 3n$

- (ν, fiss) .

The neutrino flux is discussed in detail in [TBM01] and is given by

$$\mathcal{F}_\nu = \frac{L_\nu}{4\pi r^2 \langle \mu \rangle} \frac{1}{\langle E_\nu \rangle} \ . \tag{6.2}$$

The neutrino luminosity is given by L_ν, the average neutrino energy by $\langle E_\nu \rangle$, which can be expressed as

$$\langle E_\nu \rangle = \frac{7\pi^4}{180\zeta(3)} = 3.15137 T_\nu \ , \tag{6.3}$$

assuming a Fermi Dirac spectrum f of temperature $T\nu$. The flux factor $\langle \mu \rangle$ in equation (6.2) has the dependence

$$\langle \mu \rangle = \frac{R_\nu^2}{2\Phi^2 \Xi r^2} \ , \tag{6.4}$$

where R_ν is the radius of the neutrino-sphere, r denotes the actual position of the expanding matter, and Ξ is the spherical dilution function which describes the radial dependence of the neutrino energy and number densities. In the vacuum approximation, assuming a sharp neutrino sphere, Ξ can be expressed as

$$\Xi = 1 - \sqrt{1 - (R_\nu/r)^2/\Phi^2} \ . \tag{6.5}$$

The factor Φ^2 accounts for the bending of null geodesics in a curved spacetime and can be expressed as

$$\Phi = \left(\frac{1 - 2GM/(c^2 R_\nu)}{1 - 2GM(c^2 r)}\right)^2 , \qquad (6.6)$$

where M denotes the mass of the protoneutron star. In our calculations the mass of the proton neutron star was assumed to be $1.4\mathrm{M}_\odot$, the neutrino-sphere was assumed to be at a radius of 34 km and the neutrino luminosity was set to $L_\nu = 1.8 \times 10^{52}$ erg/s, in agreement with [TBM01], [WJT94] and [FM95].

The energy-averaged cross sections are given by

$$\langle \sigma_\nu \rangle = \int dE \sigma(E) f(E; T_\nu, \alpha) , \qquad (6.7)$$

where the parameters of the Fermi-Dirac spectrum f are the neutrino temperature T_ν and the chemical potential α, which is set to zero for a typical supernova spectrum [KLF04]. Recent SNIIe simulations indicate that the neutrino temperature spans a range between 3 and 4 MeV. Thus, we have performed two sets of calculations for these two temperatures values.

[Mey95] has shown that neutrino-reactions on free nucleons are also of great importance for r-process calculations in a high entropy scenario. For this reason we have included the reactions

$$\nu + n \to p + e^- \qquad (6.8)$$

in our calculations as well. The reactions rate of (6.8) are given by [Bur01]

$$\lambda_{\nu n} = \mathcal{F}_\nu \times 1.705 \times 10^{-44} \mathrm{cm}^2 \left(\frac{1 + 3g_A^2}{4}\right) \left(\frac{\epsilon_\nu + \Delta_{np}}{m_e c^2}\right)^2 \left[1 - \left(\frac{m_e c^2}{\epsilon_\nu + \Delta_{np}}\right)^2\right]^{1/2} W_M ,$$
$$(6.9)$$

where g_A is the axial-vector coupling constant ($= 1.26$), $\Delta_{np} = m_n c^2 - m_p c^2 = 1.29332$ MeV, and for a collision in which the electron obtains all of the kinetic energy $\epsilon_{e^-} = \epsilon_\nu + \Delta_{np}$. W_M is the correction for weak magnetism and is approximately equal to $(1 + 1.1\epsilon_\nu/m_n c^2)$. The energy-averaged cross-sections were calculated by [KZK$^+$05] for a grid of eight temperatures ($T_\nu = 1.0, 2.8, 3.5, 4.0, 5.0, 6.4, 8.0$ and 10.0 MeV). In between these values a logarithmic-interpolation is performed.

Numerical treatment of the neutrino-induced reactions

Neutrino-induced reaction can be included in the present r-process network code using equation (4.20) which describes the abundance changes of a nucleus over a time-step Δt. This treatment follows neutron-captures, photo-disintegrations, beta-decays, beta-delayed neutron-emission, and neutrino-induced neutron evaporation implicitly, while the neutron number density is assumed to vary slowly
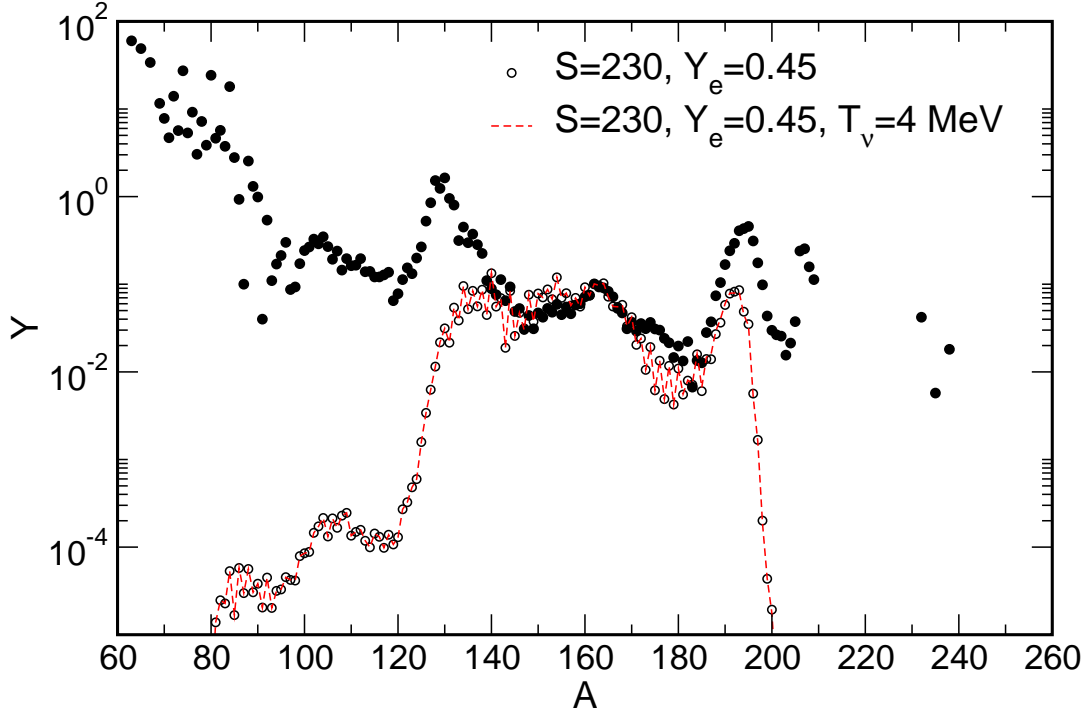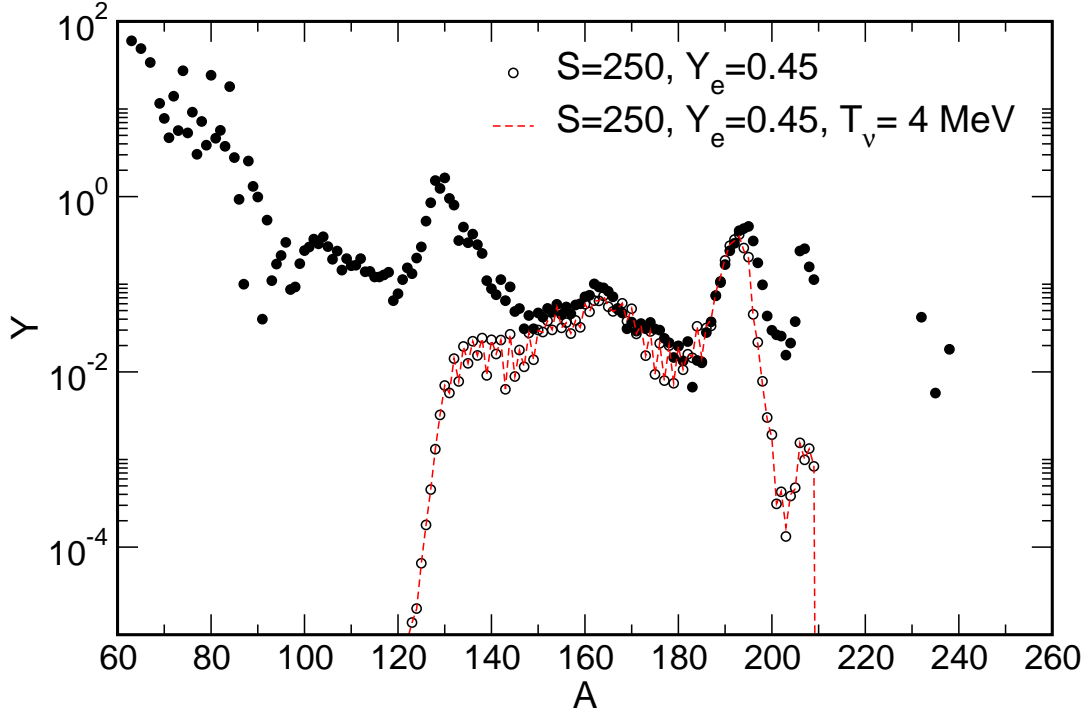
Figure 6.5: *Abundance pattern of r-process nucleosynthesis including neutrino-induced reactions for an entropy of $S = 230$ k_B. Open circles represent the standard r-process calculation without neutrinos.*

during a time Δt and its change is calculated in an explicit way. Neutrino-induced fission is also treated within this approximation in an explicit way, updating the abundances at the end of each timestep, similarly to the neutron abundances. Thus, the time-evolution is decoupled from the other reaction mechanisms. If the time steps are small enough, the time-evolution of the fission process and neutron absorption can be treated in a two-step approach: (1) In the first step, the reaction network (4.20) evolves over a time step Δt and the new abundances at the time $t + \Delta t$ are calculated. (2) In the second step, the abundance change arising solely from fission is calculated in a linearized approach:

$$\Delta Y(Z, A)^{\text{fission}} = \lambda_\nu^{\text{fiss}} Y(Z, A) \Delta t .\qquad (6.10)$$

This abundance then can be distributed among the fission fragments weighted by their individual fission yields [KZK$^+$05]. The data of [KZK$^+$05] provides only one fission fragment - the counterpart has to be reconstructed by applying charge and mass conservation

$$
\begin{aligned}
Z &= Z_1 + Z_2 - 1 & (6.11)\\
A &= A_1 + A_2 + n_{\text{eva}}, & (6.12)
\end{aligned}
$$

Figure 6.6: *Abundance pattern of r-process nucleosynthesis including neutrino-induced reactions for an entropy of $S = 250$ k_B. Open circles represent the standard r-process calculation without neutrinos.*

where n_{eva} is the number of released neutrons during the fission process. The abundance change of one pair of fission fragments is then given by

$$\Delta Y(Z_1, A_1)_1^{\mathrm{frag}} = P(A_1, Z_1)\Delta Y(Z, A)^{\mathrm{fission}} \qquad (6.13)$$
$$\Delta Y(Z_2, A_2)_2^{\mathrm{frag}} = P(A_2, Z_2)\Delta Y(Z, A)^{\mathrm{fission}} . \qquad (6.14)$$

Neutron-decay and the reaction (6.8) have to be treated in the same way as fission, as (4.20) does not follow the individual neutron abundances explicitly. Their contribution can be written as

$$\Delta Y_n = -(\lambda_n + 2\lambda_{\nu n})Y_n \Delta t, \qquad (6.15)$$

where the factor 2 takes into account that two converted protons capture two neutrons and form an α-particle.

In the Figures 6.5 - 6.8 the results of an r-process which includes neutrino-induced reactions, for four entropies ($S_1 = 230, S_2 = 250, S_3 = 270$ and $S_4 = 290k_B$) are shown. We have chosen an electron fraction of $Y_e = 0.45$ and a neutrino temperature of $T_\nu = 4$ MeV for all four runs. As mentioned in [KZK$^+$05], neutrino-induced reactions only become important for $A \geq 200$. Therefore, it is not surprising that there is no effect of neutrino-induced reactions for S_1 and S_2,
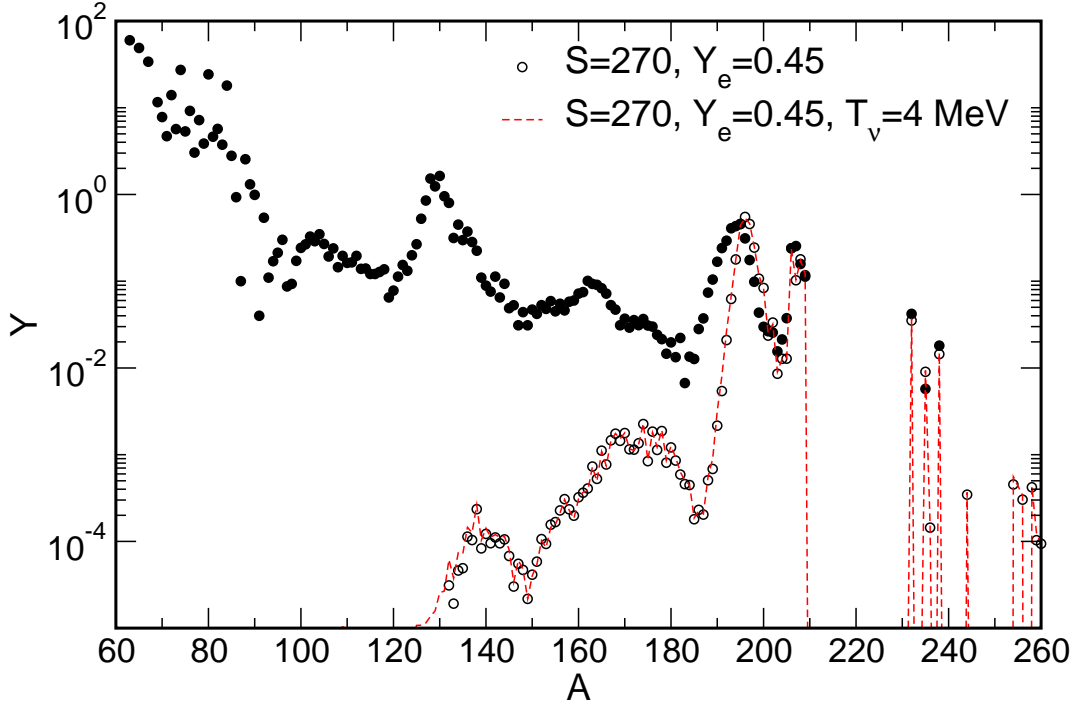
Figure 6.7: *Abundance pattern of r-process nucleosynthesis including neutrino-induced reactions for an entropy of $S = 270$ k_B. Open circles represent the standard r-process calculation without neutrinos.*

as the neutron-to-seed ratio is not high enough to reach the $A = 200$, whereas for S_3 and S_4 the neutron-to-seed ratio is sufficient to reach the A=200 region.

In Figure 6.7 the result for the entropy S_3 is shown. The filled circles represent the observed solar r-process abundances. Our benchmark calculations, the runs without the inclusion of any neutrino-induced reactions, are plotted as open circles scaled to match the observed solar abundances for A=195. The same scaling factor was applied to the abundances which were obtained after including the neutrino-induced reactions (dashed red-line). In the run where neutrinos were included, the abundances in the mass range $130 \leq A \leq 150$ are slightly overproduced compared to the standard run without neutrinos. This enhancement is due to neutrino-induced fission in the mass range $A \approx 230$ when, after the freeze-out of the r-process, nuclei decay back to stability. However, this effect of neutrino-induced neutron evaporation is small for this particular mass-range in comparison to neutrino-induced fission.

Figure 6.8 shows the same data for the higher entropy S_4. This entropy has such a high neutron-to-seed ratio that nuclei in the mass region of A=300 can easily be reached. [KZK+05] have pointed out that neutrino-induced fission becomes the dominating de-excitation mode if the fission barriers B_f and neutron separation energies S_n are of the same order for the neutrino fluxes discussed
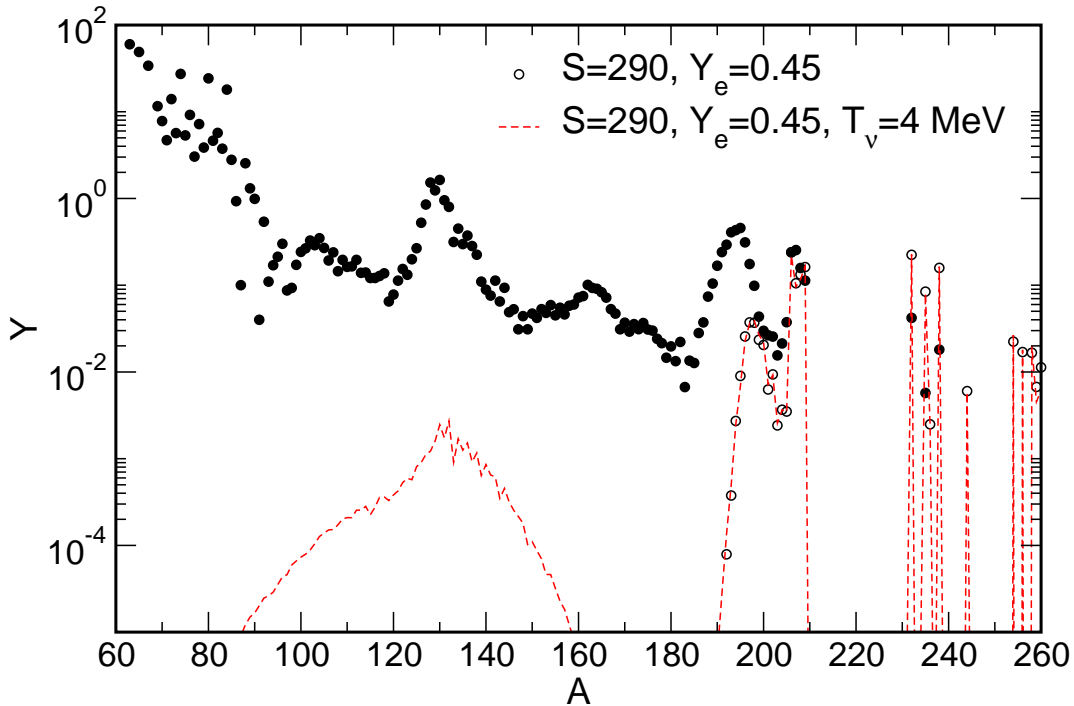
Figure 6.8: *Abundance pattern of r-process nucleosynthesis including neutrino-induced reactions for an entropy of $S = 290$ k_B. Open circles represent the standard r-process calculation without neutrinos.*

here. In the A=245 region neutrino-induced fission dominates for nuclei with $S_n > 4.5$ MeV whereas in the A=275 region fission is the dominating mode even for $S_n > 3$ MeV. The neutron separation energy can roughly be interpreted as a measure of the distance of a nucleus from the valley of stability, approaching $S_n = 0$ at the neutron drip-line. In this high entropy run this means that many nuclei can contribute to the neutrino-induced fission process after the the freeze-out of the r-process and the subsequent decay back to stability. The fragment distributions peak at $A_l \approx 100$ and $A_h \approx 140$ for progenitor masses of $A \approx 245$. Progenitor nuclei in the mass range $A \approx 275$ fission mainly symmetrically and favor therefore $A_l \approx 132$. The final abundance pattern of this high entropy run clearly support this picture of the (at least) two different mass regions contributing to the extremely enhanced abundances in the mass range $80 \leq A \leq 160$. Figure (6.11) shows a snapshot of the r-process path in the N-Z plane for two different times (color coded are the abundances). In the lower panel one can see that the mass range of interest ($A \approx 215 - 300$) is already obtained after 2 sec. At this time, the masses around $A \approx 130$ become populated by neutrino-induced fission of $A \approx 300$ progenitors that are most abundant at this time. However, the abundance maximum is not centered at a certain A - in fact it is smeared out over a mass range between $210 \leq A \leq 280$, supporting the above discussed
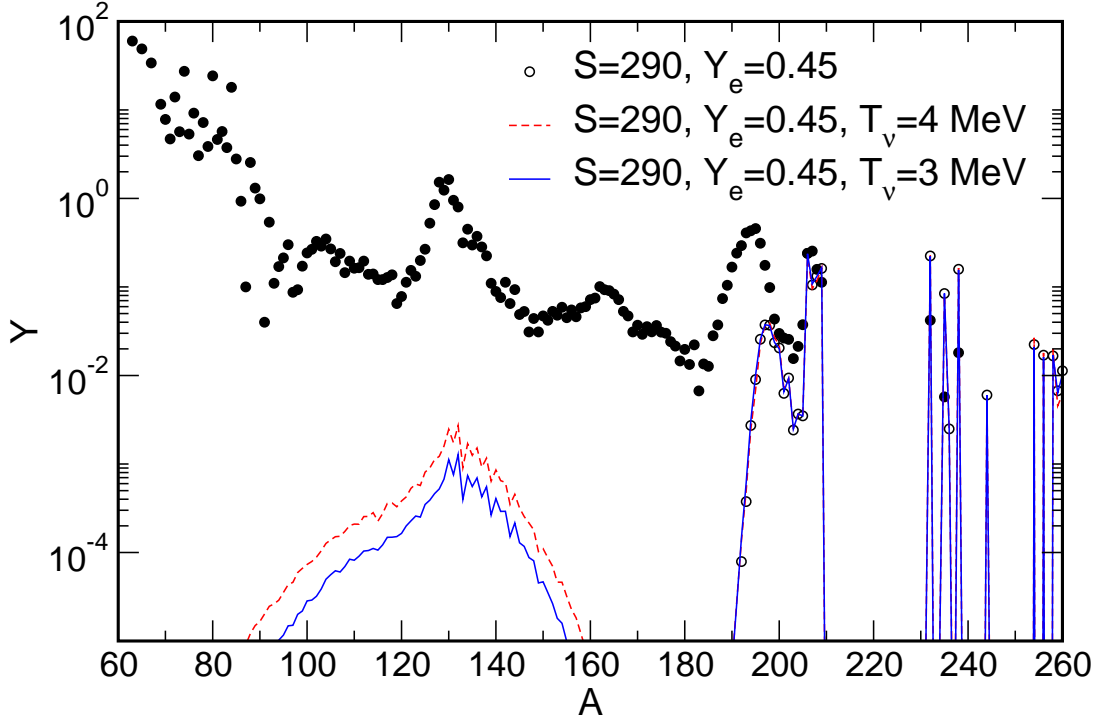
Figure 6.9: *Abundance pattern of r-process nucleosynthesis including neutrino-induced reactions for two different neutrino temperatures. Open circles represent the standard r-process calculations without neutrinos.*

interpretation.

In order to get a better understanding of the fission fragment production for $A \approx 200 - 300$ mass progenitors, we have repeated the calculation for the S_4 entropy, but this time with a lower neutrino temperature. We have set the neutrino temperature to $T_\nu = 3$ MeV following the suggestion of [TBM01]. Due to the T_ν^5 dependence of equation (6.1), the neutrino-flux for this run will be smaller (and therefore the neutrino-induced rates, too). Figure 6.9 compares the abundance distribution for the two neutrino-temperatures. Even for the lower neutrino temperature the low mass abundances are enhanced compared to the scenario without any neutrinos. Due to the smaller fission rates these enhancements are less pronounced, but still indicating that the r-process path (through neutrino-induced neutron evaporation) and the fission-fragment distribution is not sensitive to small neutrino-temperature variations in the $T_\nu = 3 - 4$ MeV regime.

One other possibility to check the sensitivity on the input parameters is to vary the expansion velocity v_{exp} of the expanding hot-bubble. As described in section 7.1, the present r-process calculation is performed in a two-step approach: (1) In the first step the seed distribution of the r-process is calculated in a charged-

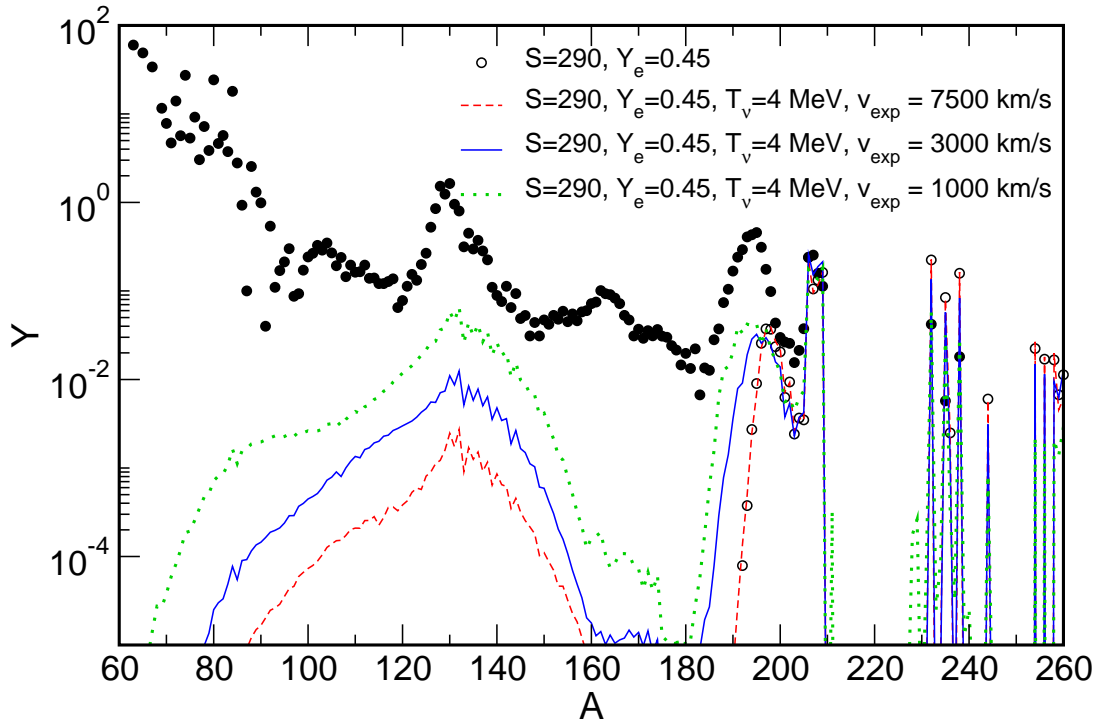**Figure 6.10:** *Influence of the expansion velocity v_{exp} on the final r-process abundance pattern for three different velocities: $v_1 = 7500$ km/s, $v_2 = 3000$ km/s, and $v_3 = 1000$ km/s. Open circles represent the standard r-process calculation without neutrino-induced reactions.*

particle network, where neutrino-induced reactions are not included yet. This is certainly a problem considering the overall consistency of the two coupled codes and has to be included in the future. However, as a first step, in exploring the effects of neutrino-induced reactions this is certainly acceptable.

We have varied the expansion velocity of the r-process network only and left the seed abundances of the charged-particle network untouched. The variation of the expansion velocity is to a certain extend equal to a variation of the initial neutrino luminosity, as the matter, with smaller expansion velocity, will stay closer to the protoneutron star for a longer time. This basically corresponds to an increase of the initial luminosity. Figure 6.10 compares the abundances of the S_4 entropy run for three different expansion velocities: $v_1 = 7500$ km/s (the standard one), $v_2 = 3000$ km/s, and $v_3 = 1000$ km/s.

The expansion velocities have a large influence on the final abundance pattern: the smaller the expansion velocity the more nuclei in the low mass regime ($A \approx 60 - 160$) can be populated by fission - reflecting the increased neutrino flux compared to the standard expansion velocity. The $A \approx 195$ peak is shifted to lower A values with decreasing velocity. The progenitors of these fission products

originate from the mass range $A \approx 240 - 280$, indicating that neutrinos operate more efficient at smaller expansion velocities.

A remarkable result of the $v = 1000$ km/s run is the fact that the second and the third peak of the observed r-process abundances could be almost reproduced with a single entropy-component. This indicates that the abundance enhancement observed in ultra-metal poor stars [CHB01] could be explained by neutrino-induced reactions, as suggested by [Qia02]. Further and certainly more consistent calculations have to verify this result.
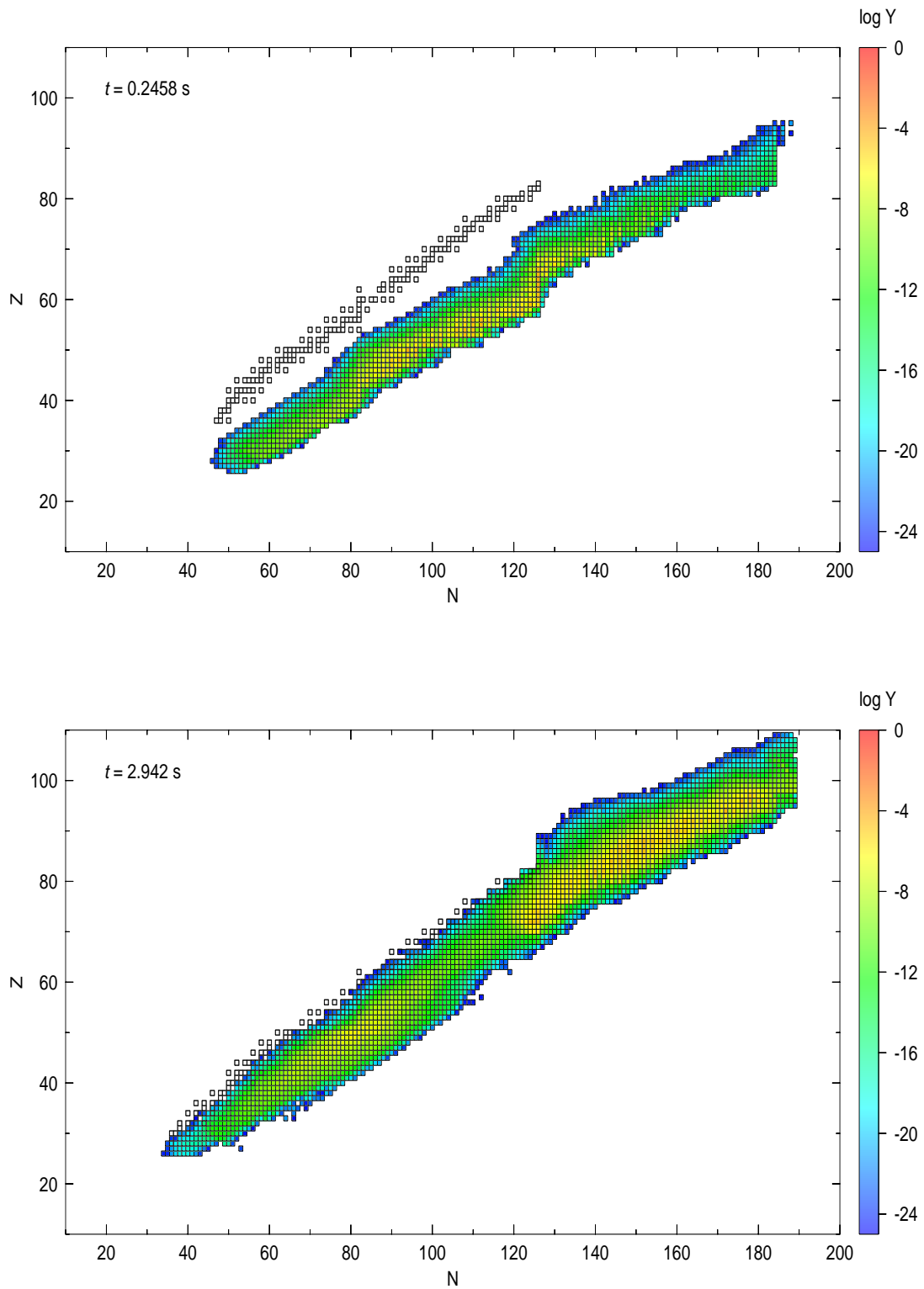
Figure 6.11: *R-process path in the N-Z plane for two different times for the S_4 entropy case. Color-coded are the abundances.*

6.3   The influence of β-delayed and neutron-induced fission

In the previous section we have seen that observations of metal-poor stars strongly support the idea that elements in the mass range of $110 \leq A \leq 130$ could be formed by fission of transuranium isotopes. We have already studied the influence of neutrino-induced fission. To get a consistent picture, neutron-induced and beta-delayed fission have to be included in the r-process calculations, too. Several groups have already performed such calculations [CTT87], [PFT01], but all of them have used the fission barriers of [HM80] which are systematically underestimated and therefore overestimate the various fission rates. Recently, two new sets of fission barriers based on two different nuclear models became available [?] and [MS99], triggering the re-evaluation of beta-delayed and neutron-induced fission rates [PKP$^+$05]. Similar to the calculation of neutrino-induced fission, beta-delayed and neutron-induced fission have to be described in a two step approach: (1) The initial step of the process, i. e. the excitation of compound levels either by beta-decay or neutron capture, has to be described within the (Quasi) Random-Phase-Approximation (QRPA) [MPK03] or within the statistical Hauser-Feshbach formalism [RTK97], respectively. (2) The de-excitation of the compound nucleus is calculated in the second step by the SMOKER code [CTT91] that describes the competition between particle emission and fission. In addition to the rate calculation the charge and mass distributions of fission yields have to be described independently and have usually been treated phenomenologically instead [IOS89]. Recently [Zin] also calculated beta-delayed fission rates utilizing the same method as for neutrino-induced fission: (1) QRPA to describe the excitation of the compound nucleus (2) Track the de-excitation of the compound nucleus with the ABLA code. This provides a global prediction of the mass and charge distributions of the fission fragments. These rates have also been incorporated into our r-process code and the abundances will be compared with the predictions of [PKP$^+$05].

Numerical treatment of neutron-induced and β-delayed fission

As before, abundance changes of individual nuclei due to neutron-captures, photo-disintegrations, beta-decays connecting neighboring isotopic chains, are calculated with implicit methods. The neutron abundance is treated in an explicit scheme. All other reactions, such ass fission for instance, have to be included in an explicit way, too.

The abundance changes due to neutron-induced fission (n,fiss) and beta-delayed fission (bdf) can be described in first order by:

$$\Delta Y(Z, A)^{(\text{n,fiss})} = \langle \sigma v \rangle_{Z,A}^{(\text{n,fiss})} n_n Y(Z, A) \Delta t \qquad (6.16)$$
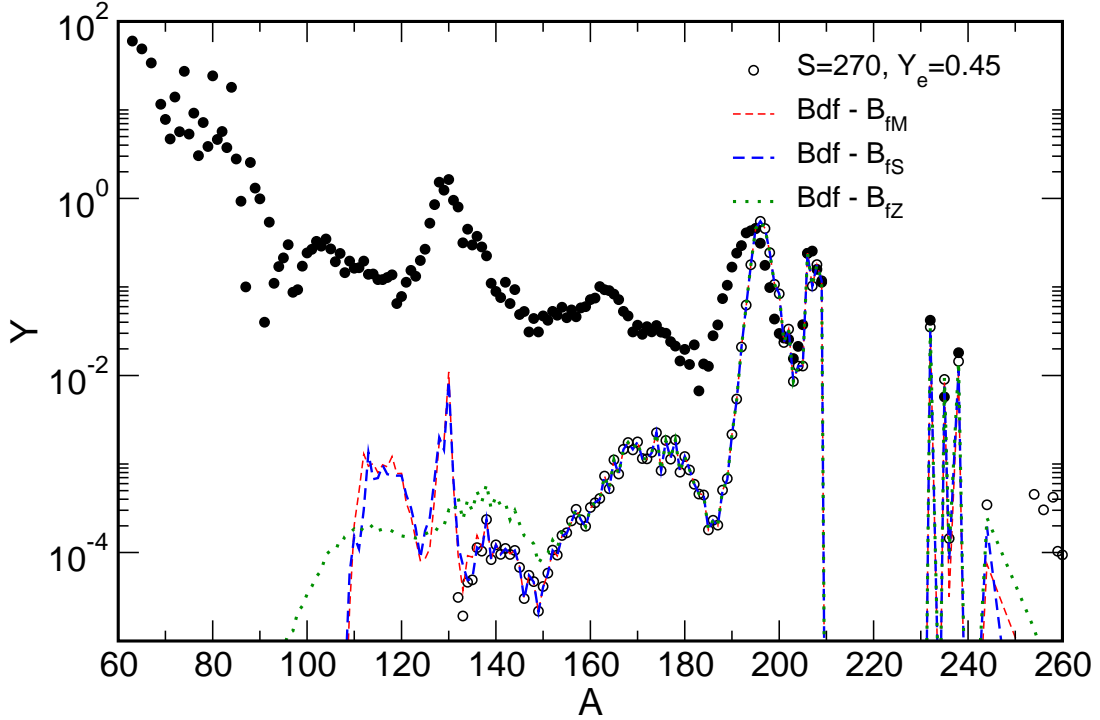
Figure 6.12: *Abundance pattern of r-process nucleosynthesis for an entropy of $S = 270$ k_B including beta-delayed fission. Plotted are the results for three different fission barriers compilations: B_{fM} [MPRT00], B_{fS} [MS99], and B_{fZ} [Zin]. Open circles represent the standard r-process calculation without fission.*

and

$$\Delta Y(Z, A)^{\text{bdf}} = \lambda^{\text{bdf}} Y(Z, A) \Delta t \ , \tag{6.17}$$

where n_n is the neutron number density and $\langle \sigma v \rangle_{Z,A}^{(\text{n,fiss})}$ is the neutron-induced fission reaction rate.

The implementation of the beta-delayed fission rates λ^{bdf} depends on which statistical code, ABLA or SMOKER, is used to calculate the de-excitation of the excited states in the daughter nucleus. If we are using the data of [Zin], where the de-excitation is calculated with the ABLA code, detailed information on the distribution of the fission fragments is available. The abundance change for one pair of fission fragments from the distribution is given by

$$\Delta Y(Z_1, A_1)^{\text{bdf}} = P(A_1, Z_1) \Delta Y(Z, A)^{\text{bdf}} \text{ and} \tag{6.18}$$
$$\Delta Y(Z_2, A_2)^{\text{bdf}} = P(A_2, Z_2) \Delta Y(Z, A)^{\text{bdf}} \ , \tag{6.19}$$

with the requirement that mass- and charge conservation is fulfilled.

If the de-excitation of the excited states of the daughter nucleus is calculated with the SMOKER code, two things have to be considered:
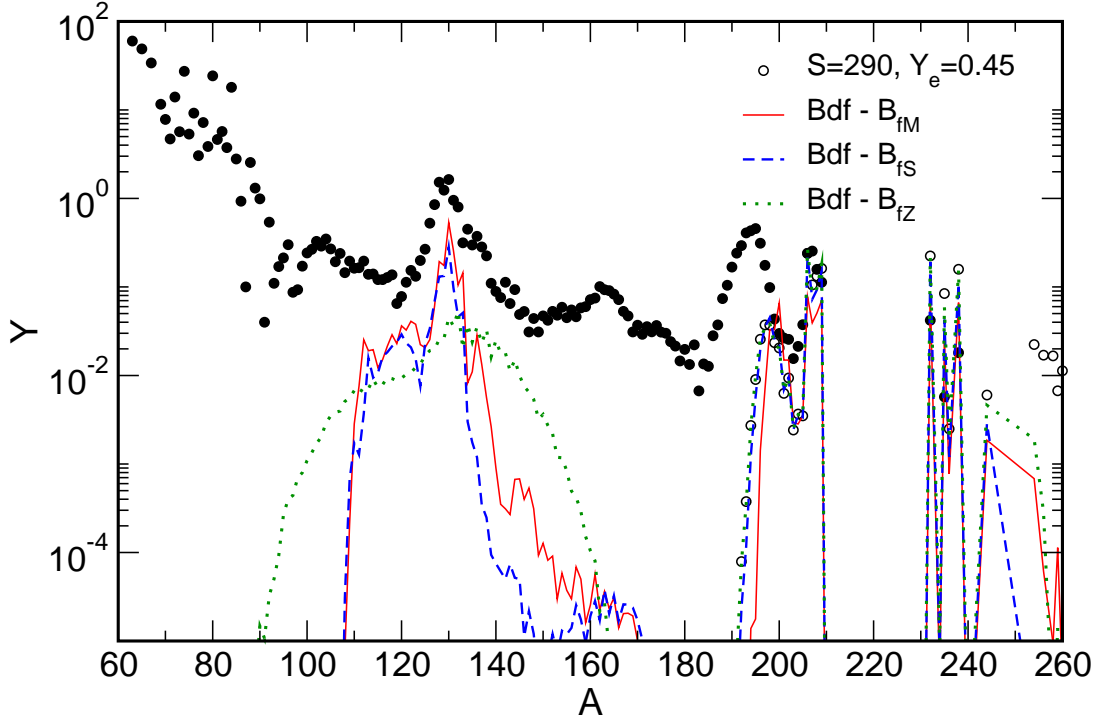
Figure 6.13: *Abundance pattern of r-process nucleosynthesis for an entropy of $S = 290$ k_B including beta-delayed fission. Plotted are the results for three different fission barriers compilations: B_{fM}[MPRT00], B_{fS} [MS99], and B_{fZ} [Zin]. Open circles represent the standard r-process calculation without fission.*

(1) Mass and charge distribution have to be extracted from experimentally known systematics

(2) [PKP+05] is only providing fission probabilities and not individual rates. Therefore, the beta-decay rates have to be redefined. In the case, where beta-delayed fission is not considered, the beta-decay rates were calculated according to

$$\lambda^{\beta} = \lambda^{\text{tot}} p_0 , \qquad (6.20)$$

$$\lambda^{\beta 1n} = \lambda^{\text{tot}} p_1 , \qquad (6.21)$$

$$\lambda^{\beta 2n} = \lambda^{\text{tot}} p_2 , \quad \text{and} \qquad (6.22)$$

$$\lambda^{\beta 3n} = \lambda^{\text{tot}} p_3 , \qquad (6.23)$$

where, p_0, p_1, p_2 and p_3 denote the probabilities for a pure beta-decay and a beta-decay followed by 1, 2, or 3 neutron emissions, respectively. The total reaction rate is defined by $\lambda^{\text{tot}} = \frac{\ln 2}{\tau_{1/2}}$. If one considers beta-delayed fission, where the branching into this channel is given by P_{fiss}, we have to replace
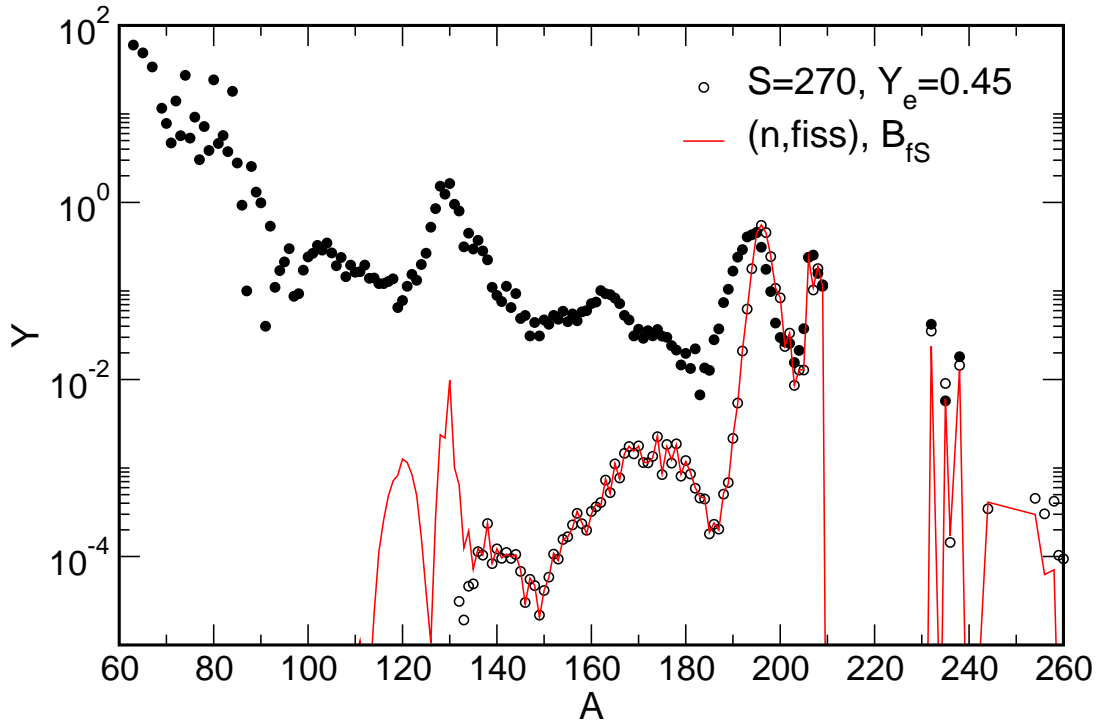
Figure 6.14: *Abundance pattern of r-process nucleosynthesis for an entropy of $S = 270$ k_B including neutron-induced fission for the fission barriers of [MS99]. Open circles represent the standard r-process calculation without fission.*

the total rate by an effective rate, which is defined by

$$\lambda^{\text{eff}} = \lambda^{\text{tot}} - \lambda^{\text{bdf}} , \tag{6.24}$$

with

$$\lambda^{\text{bdf}} = \lambda^{\text{tot}} * P_{\text{fiss}} , \tag{6.25}$$

which leads to an overall reduction of the beta-decay rates (6.20).

The charge and mass distributions can extracted from systematics of experimental information on fission of nuclei in the mass range of $A \approx 300$. Depending on the progenitor mass, the fission distribution will either be symmetric or asymmetric [IOS89]. Nuclei in the mass range $255 \leq A \leq 265$ will fission symmetrically, all other nuclei will fission asymmetrically. In the asymmetric case, the distribution is given by

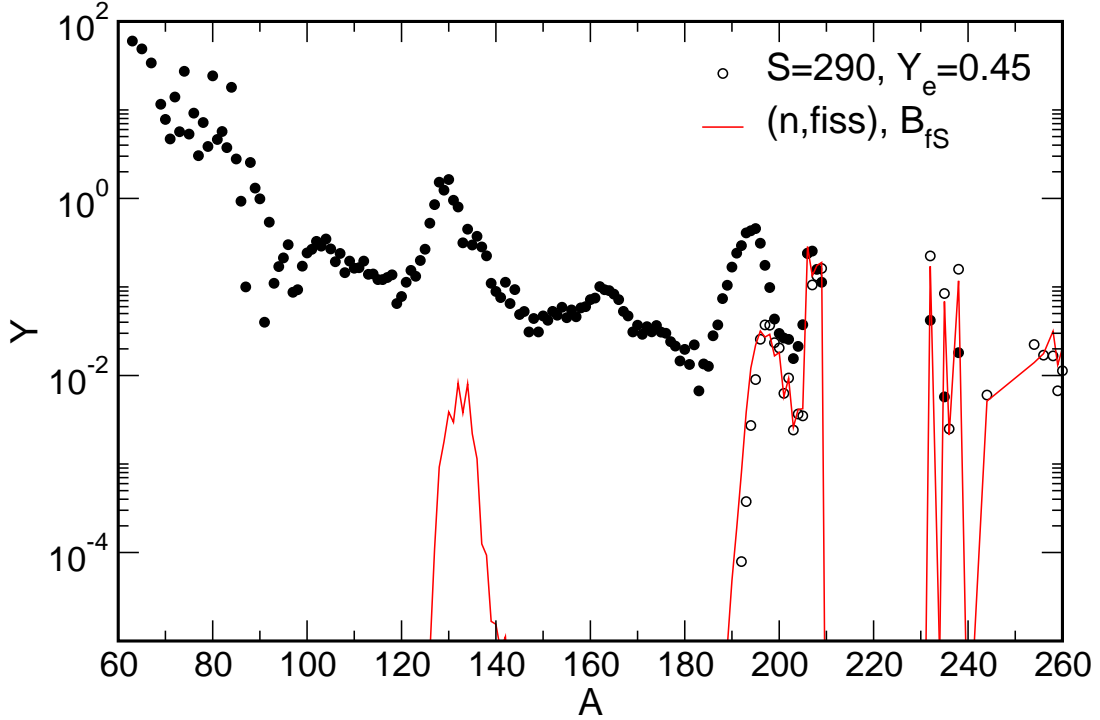$$A_1 \;=\; 130 , \tag{6.26}$$
$$Z_1 \;=\; 50 \tag{6.27}$$

Figure 6.15: *Abundance pattern of r-process nucleosynthesis for an entropy of $S = 290$ k_B including neutron-induced fission for the fission barriers of [MS99]. Open circles represent the standard r-process calculation without fission.*

and

$$A_2 = A - A_1 \, , \qquad (6.28)$$

$$Z_2 = 52 - \frac{2}{20}(Z - 80) \, . \qquad (6.29)$$

The effects of beta-delayed fission on the elemental abundances after freeze-out of the r-process (followed by the decay back to stability) are shown in Figures 6.12 and 6.13. Figure 6.12 shows the result of the moderately high entropy $S_3 = 270k_B$ for three different fission barriers compilations: B_{fM} [MPRT00], B_{fS} [MS99], and B_{fZ} [Zin]. The fission fragment distributions for B_{fM} and B_{fS} were calculated with equation (6.20). In the B_{fZ} case we have applied the calculated distribution of [Zin]. From Figure 6.12 it can be seen that these two distributions have a large influence on the final abundance pattern.

Contrary to the B_{fZ} case, both B_{fM} and B_{fS} show two pronounced peaks in the abundance distribution. These peaks can be attributed to nuclei that fission in the masses region $A^p \leq 255$. As we have seen in equation (6.20) the distribution of fission fragments is asymmetrical for these progenitor masses. It creates

a fragment with $A_1 = 132$ and a lighter one with $A_2 = A - 132$. For progenitor masses $240 \leq A^p \leq 255$ the lighter fission fragment is therefore of the order of $110 \leq A_2 \leq 132$. The fission barriers of [MPRT00] and [MS99] are almost equal in the mass region of interest. As the same fission yield distribution is applied to both calculations the abundance distribution of B_{fM} and B_{fS} does not show any significant difference. Such a pronounced structure in the abundance pattern can not be observed in the B_{fZ} run. This results mainly from a different shape of the fission distribution as all fission barriers are of similar order for masses $240 \leq A^p \leq 255$. The distribution of [Zin] does not show any symmetrical or asymmetrical features, instead it distributes the fission products smoothly over a mass range of $100 \leq A \leq 150$.

With increased entropy heavier masses can be reached by the r-process. The results for the entropy $S_4 = 290 k_B$ are shown in Figure 6.13. The abundance distribution for this high entropy case follows the trends already seen in the moderate entropy scenario. A rather smooth abundance distribution, where the fission fragments populate a fairly broad mass range, is observed for the B_{fZ} run. The B_{fS} and B_{fM} runs show the already observed double-peak structure. For those two runs we can separate the abundances built by fission into three regimes: The elements in the mass range $110 \leq A \leq 125$ are built up by the lighter mass fragment of asymmetric fission of progenitor nuclei with $A^p \leq 255$. The elements in the mass range between $A = 125$ and $A = 135$ are mainly formed by symmetric fission of progenitors with $255 \leq A^p \leq 265$ and by the $A = 130$ mass-fragment of asymmetric fission of the $A \leq 255$ and $A \geq 265$ mass range. Progenitor nuclei with $A^p \geq 265$ populate the mass range $135 \leq A \leq 170$ by asymmetric fission. As we have seen above the fission barriers of [MPRT00] and [MS99] are of the same order for $200 \leq A \leq 265$. Therefore, it is not surprising that there is almost no difference in the abundance distributions for those fission barriers. However, this is in the mass range $135 \leq A \leq 165$, where the B_{fM} run predicts higher elemental abundances. This is somehow surprising, as the [MPRT00] compilation overestimates the fission barriers for nuclei with neutron number $N \geq 184$. Higher fission barriers would lead to lower fission rates and therefore to smaller fission yields in the $135 \leq A \leq 165$ mass region. In Figure (6.13) the opposite behavior can be observed. The run using the higher fission barriers (B_{fM}) predicts higher fission yields! This paradoxon can be understood as follows. Recall how the beta-decay rates were calculated if beta-delayed fission is taken into account:

$$\lambda^\beta = \lambda^{\text{tot}} - \lambda^{\text{fiss}} . \tag{6.30}$$

A non-vanishing fission rate reduces the beta-decay rates. This reduction is higher for bigger fission rates. The fission barriers of [MPRT00] predict too high values for $N \geq 184$, which results in a decrease of the fission rates and consequently in an increase of the effective beta-decay rate.. Higher beta-decay rates push material

more effectively to nuclei with masses $A \geq 265$ which fission asymmetrically and therefore contribute to the fission yields of $135 \leq A \leq 165$. The fission barriers predicted by [MS99] are smaller compared to the ones of [MPRT00]. Hence, the effective beta-decay rates are reduced, as the smaller fission barriers increase the fission rates. Smaller beta-decay rates prevent an effective build-up of high-mass elements and therefore reduce the contribution by fission of $A \geq 265$ nuclei to the $135 \leq A \leq 165$ mass regime. The reduction of the beta-decay rates can also be observed in the mass range $A \approx 190$ where the abundance distribution is shifted towards higher masses by several units. We can see from equation (6.20) that a reduction of the effective beta-decay rates also results in a reduction of the beta-decay rates followed by one, two, or three neutron emission. The abundance distribution is shifted to higher masses as less neutrons are emitted after a successful beta-decay.

Such a behavior cannot be observed for the B_{fZ} run as all rates were calculated simultaneously, and therefore no rescaling of the beta-decay rates was needed. The fission barriers used in B_{fZ} are comparable to [MPRT00] and [MS99] for $A \leq 240$. They are overestimated for $A \geq 240$ and therefore predict higher elemental abundances in this mass range compared to B_{fS} and B_{fM}. As already seen in the moderate entropy scenario, the fission fragments calculated in the B_{fZ} run are smoothly distributed over a broad mass range $90 \leq A \leq 160$ without a pronounced peak structure at $A = 130$ which is observed in the B_{fS} and B_{fM} runs.

In Figures 6.14 and 6.15 the influence of neutron-induced fission on the final r-process abundances is shown. In the work of [PKP+05] it was shown that the nuclear chart, depending on the dominant fission mode, can be divided into three regions. Beta-delayed fission is the dominant fission mode for $Z \leq 87$ and $A \leq 260$. For nuclei with $88 \leq Z \leq 90$, beta-delayed fission and neutron-induced fission are of the same order. Neutron-induced fission is the dominant fission mode for nuclei with $Z \geq 91$. It is also the dominant fission mode even for nuclei $Z \leq 87$ and $A \geq 260$. These nuclei have very large neutron numbers and are only part of the r-process path for conditions of very high initial entropies where the neutron drip line is almost reached. In Figure 6.15 the results of such a high entropy run are shown. As mentioned above the high entropy pushes the r-process path towards the neutron drip line and by-passes the $Z \leq 87$ and $A \leq 260$ region where beta-delayed fission is the dominant fission mode. Moreover, nuclei with $A \geq 260$ are reached which then fission is predominantly of asymmetrically. This effect can be seen clearly in the abundance distribution where the $A \approx 132$ peak is mainly fed by the first fragment of the asymmetrical fission mode and the mass region $A = 132 - 140$ by the second fragment. Elements in the mass region $126 \leq A \leq 132$ are formed during the decay back to stability of progenitor nuclei with $Z \geq 90$ and $A \leq 255$ which then fission asymmetrically.

The result for the entropy S_3 is shown in Figure 6.15. Lower entropies imply a lower neutron-to-seed ratio or in other words a smaller neutron number density.
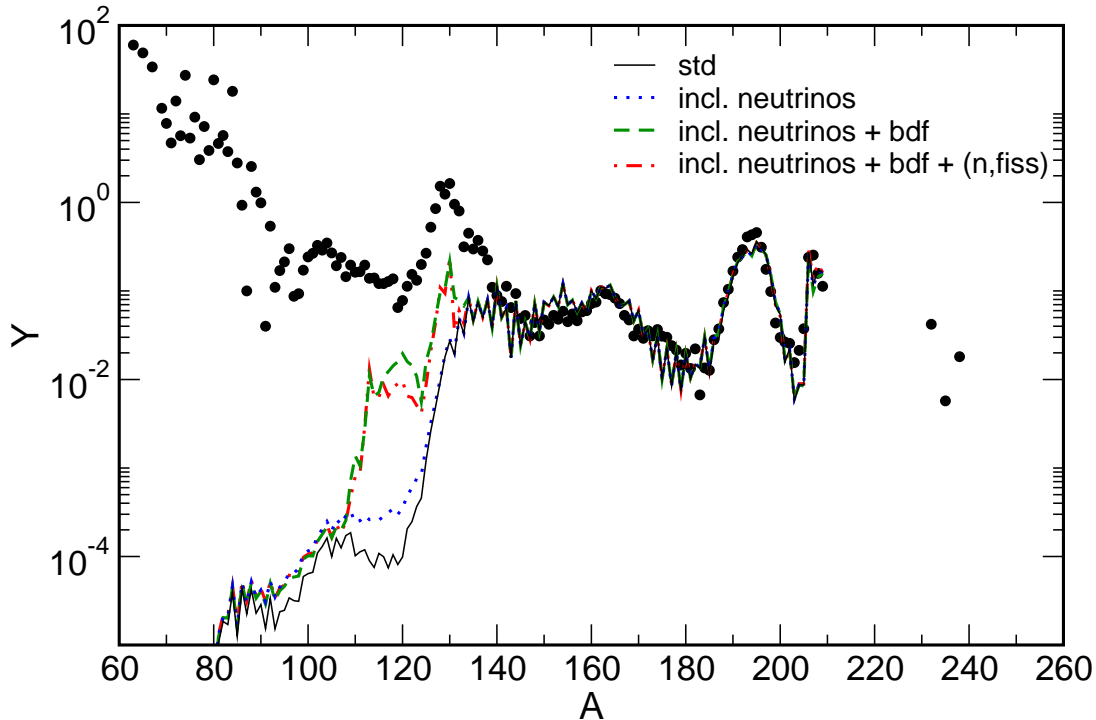
Figure 6.16: *Superpostion of the entropy components S_1-S_4. The mass range between A=140 and A=202 was fitted. The fission barriers of [MS99] were applied.*

The smaller neutron number density prevents the reach of the $Z \leq 87$ and $A \geq 260$ region where the neutron-induced fission is the dominant decay mode. The r-process path is pushed towards the valley of stability where neutron-induced fission competes with beta-delayed fission. The maximum masses reached in the case of initial entropy S_3 are of the order of $A = 260$. The fission distribution consists therefore of two components: (1) Asymmetrical fission for progenitor masses $A^p \leq 255$ which is mainly feeding the elements in the mass region $112 \leq A \leq 130$. (2) Elements in the mass region $130 \leq A \leq 136$ are mainly populated by the symmetrical fission mode of progenitor nuclei in the mass region $A^p \geq 255$.

In the calculation of the final r-process distribution in Figures 6.14 and 6.15 we have only considered the contribution of neutron-induced fission and set the beta-delayed fission rates to zero. Therefore the presented contributions of neutron-induced fission to the final abundance distributions are overestimated.

6.4 Superposition of entropy-components

So far, we have presented the results for single entropy components. However, in realistic supernova explosions the ejected mass will always consist of a superposition of different entropy components, reflecting the fact that matter can be
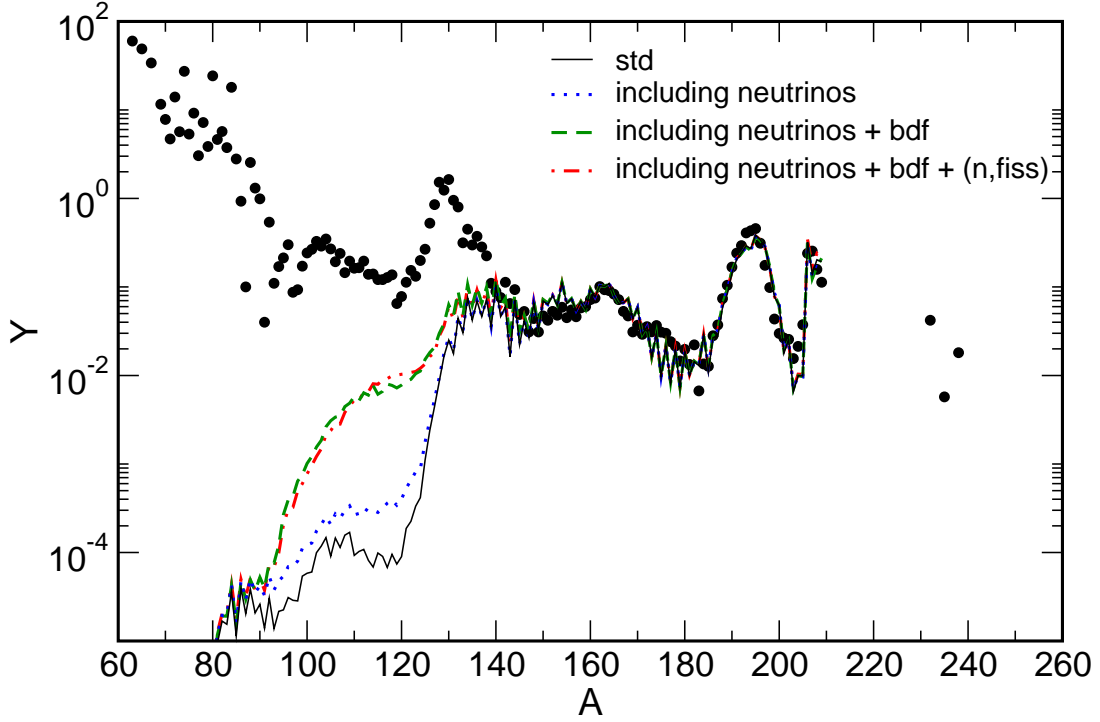
Figure 6.17: *Superpostion of the entropy components $S_1 - S_4$. The mass range between $A=140$ and $A=202$ was fitted. The fission barriers of [Zin] were applied.*

ejected from regions with different physical conditions. The weighting factor g_i of each individual entropy component depends crucially on the mass contribution of each individual entropy component to the total ejected mass. Components with higher entropy contribute less to the total ejected mass. Following the suggestion of [FRT99] we have chosen the individual weighting factors to be of the form

$$g_i = x_1 e^{-x_2 S_i} \ . \tag{6.31}$$

The two fitting coefficients x_1 and x_2 are calculated by the minimization of the difference of the observed r-process abundances and the superposed calculated abundances:

$$\sum_A \left(\log Y_A^{\text{exp}} - \log \left(\sum_{i=1}^{n} x_1 e^{-x_2 S_i} Y_{A,i}^{\text{calc}} \right) \right)^2 = \min \ , \tag{6.32}$$

or

$$\frac{\partial}{\partial x_1} = \sum_A \left(\log Y_A^{\text{exp}} - \log \left(\sum_{i=1}^{n} x_1 e^{-x_2 S_i} Y_{A,i}^{\text{calc}} \right) \right)^2 = 0 \tag{6.33}$$

$$\frac{\partial}{\partial x_2} = \sum_A \left(\log Y_A^{\text{exp}} - \log \left(\sum_{i=1}^{n} x_1 e^{-x_2 S_i} Y_{A,i}^{\text{calc}} \right) \right)^2 = 0 \ . \tag{6.34}$$

Equation (6.33) is solved by an two-dimensional Newton-Raphson scheme. The results of the four component superposition ($S_1 = 230, S_2 = 250, S_3 = 270$ and $S_4 = 290k_B$) are shown in Figures 6.16 and 6.17. The difference between both figures is only the treatment of beta-delayed fission. In Figure 6.16 the fission barriers of [MS99] and the fission distribution of equation (6.20) were applied. In Figure 6.17 we have applied the fission barriers and fission distributions of [Zin]. It can be seen that in both cases beta-delayed fission is the dominant fission mode. Neutrino-induced fission plays a minor, compared to the other fission modes.

Appendix A

The Saddle Point Approximation

The saddle point approximation, also known as stationary phase approximation, is a widely used method in statistical mechanics to evaluate integrals of the form:

$$I = \int_{-\infty}^{\infty} e^{-f(x)} dx \ . \tag{A.1}$$

The saddle point approximation can be applied if the function $f(x)$ satisfies certain conditions. Assume that $f(x)$ has a global minimum $f(x_0) = y_{min}$ at $x = x_0$, which is sufficiently separated from other local minima and whose value is sufficiently smaller than the value for those. An example is give in Figure A.1.
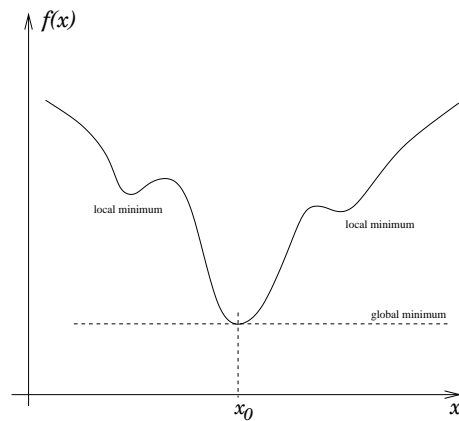

Figure A.1

Consider a Taylor expansion of $f(x)$ around the point x_0:

$$f(x) = f(x_0) + \partial_x f(x)|_{x=x_0}(x - x_0) + \frac{1}{2}\partial_x^2 f(x)|_{x=x_0}(x - x_0)^2 + \mathcal{O}((x - x_0)^3) \ .$$

Since $f(x_0)$ is a global minimum, it is clear that $\partial_x f(x_0) = 0$. Therefore, $f(x)$ may be approximated to quadratic order as

$$f(x) \approx f(x_0) + \frac{1}{2} f''(x_0)(x - x_0)^2.$$

The above assumptions on the minima of $f(x)$ ensure that the dominant contribution to (A.1) will come from the region of integration around x_0:

$$I \quad \approx \quad e^{-f(x_0)} \int_{-\infty}^{\infty} dx e^{-\frac{1}{2} f''(x_0)(x-x_0)^2} \qquad (A.2)$$

$$I \quad \approx \quad e^{-f(x_0)} \left(\frac{2\pi}{f''(x_0)} \right)^{\frac{1}{2}}. \qquad (A.3)$$

In the last step a Gaussian integral was performed. This approximation is only valid for a one dimensional integration.

Higher dimensional integrals can be approximated by the same technique, with the Taylor expansion being replaced by its n-dimensional generalization, see [GC65] for details:

$$I \quad = \quad \int_{-\infty}^{\infty} dx_1 \ldots \int_{-\infty}^{\infty} dx_n e^{-f(x_1,\ldots,x_n)} \qquad (A.4)$$

$$I \quad \approx \quad \frac{e^{-f(x_{10},\ldots,x_{n0})} \left(2\pi \right)^{\frac{n}{2}}}{\sqrt{det|\partial^2 f/\partial_{x_i}\partial_{x_j}|_0}}, \qquad (A.5)$$

where the subscript $|\ldots|_0$ once again denotes the saddle point $(x_{10}, \ldots, x_{n0})$ of the function f.

Appendix B

Pairing in a Nutshell

Following [SJ87], a short derivation of the Bardeen, Cooper and Schrieffer (BCS) equations [BCS57] is presented here.

B.1 BCS Equations

The Hamiltonian of the BCS system can be written as

$$\mathcal{H}_0 = \sum_k \epsilon_k (a_k^\dagger a_k + a_{-k}^\dagger a_{-k}) - \Delta \sum_k (a_{-k}^\dagger a_k^\dagger + a_k a_{-k}) \ , \tag{B.1}$$

where ϵ_k denotes the energy of a single particle state and Δ, called the pairing gap, denotes a quantity proportional to the pairing force.

One advantage of choosing this particular representation of the Hamiltonian is the fact that all terms which appear in equation (B.1) are diagonal and therefore simplify the solution of the problem. However, one has to notice that the particle number conservation is violated and has to be introduced by hand via a Lagrange multiplier μ, called the chemical potential:

$$\mathcal{H} = \mathcal{H}_0 + \mu N \ , \tag{B.2}$$

with N being the number of pairs defined by $N = \sum_k (a_k^\dagger a_k + a_{-k}^\dagger a_{-k})$.

An exact diagonalization of $\mathcal{H}$ is possible. The interaction regime can be divided into two parts: A part inside a certain range around the Fermi level, defined by $|\epsilon_k - \mu|$, and a part outside this regime. The interaction vanishes outside this interval, therefore the Hamiltonian is diagonal there. Inside the interval the Hamiltonian can be diagonalized by the transformation

$$\alpha_k = u_k a_k + v_k a_{-k}^\dagger \ , \quad \alpha_{-k} = u_k a_{-k} - v_k a_k^\dagger \ , \tag{B.3}$$

known as the Bogolyubov transformation. The functions u_k and v_k are at our disposal to minimize $\langle \mathcal{H} \rangle$. To ensure the same commutation relations between

the α operators as those of the a operators, a normalization of u and v is required:

$$u_k^2 + v_k^2 = 1 \ . \tag{B.4}$$

Solving (B.3) for the old operators and inserting them into (B.1) gives

$$\mathcal{H} = \Omega_{gs} + \sum_k H_k^{(1)} \left(\alpha_k^\dagger \alpha_k + \alpha_{-k}^\dagger \alpha_{-k} \right) + \sum_k H_k^{(2)} \left(\alpha_{-k}^\dagger \alpha_k^\dagger + \alpha_k \alpha_{-k} \right) \ , \tag{B.5}$$

where

$$\Omega_{gs} = 2 \sum_k \left[(\epsilon_k - \mu) v_k^2 - \Delta u_k v_k \right] \ , \tag{B.6}$$

$$H_k^{(1)} = (\epsilon_k - \mu)(u_k^2 - v_k^2) + 2u_k v_k \Delta \ , \tag{B.7}$$

$$H_k^{(2)} = 2(\epsilon_k - \mu) u_k v_k - (u_k^2 - v_k^2)\Delta \ . \tag{B.8}$$

If $\mathcal{H}$ is required to be diagonal in the α operators we must have vanishing $H_k^{(2)}$ for all k:

$$2(\epsilon_k - \mu) u_k v_k = (u_k^2 - v_k^2)\Delta \ , \tag{B.9}$$

with the solutions

$$v_k^2 = \frac{1}{2} \left(1 - \frac{\epsilon_k - \mu}{\epsilon_k} \right) \tag{B.10}$$

$$u_k^2 = \frac{1}{2} \left(1 + \frac{\epsilon_k - \mu}{\epsilon_k} \right) \tag{B.11}$$

$$E_k = \sqrt{(\epsilon_k - \mu)^2 + \Delta^2} \ . \tag{B.12}$$

The BCS wave function is given by

$$|gs\rangle = \Pi_k \left(u_k + v_k a_{-k}^\dagger a_k^\dagger \right) |vac\rangle \ . \tag{B.13}$$

This solution does not describe a system with a definite number of particles. The average number of pairs is given by

$$N_0 = \langle gs|N|gs \rangle = \sum_k \left(1 - \frac{\epsilon_k - \mu}{E_k} \right) \tag{B.14}$$

and therefore the number of particles is:

$$n = \frac{1}{2} \sum_k \left(1 - \frac{\epsilon_k - \mu}{E_k} \right) \ . \tag{B.15}$$

The energy of the system is given by

$$E = \langle gs|\mathcal{H} - \mu N|gs \rangle \tag{B.16}$$

$$= 2 \sum_k (\epsilon_k - \mu) v_k^2 - \Delta \left(\sum_k u_k v_k \right)^2 \ . \tag{B.17}$$

Minimizing the energy with respect to the gap parameter Δ yields

$$\frac{2}{\Delta} = \sum_k \frac{\Delta}{E_k} \, , \tag{B.18}$$

which is commonly called the Gap-equation.

So far, the BCS equations were only presented for the $T = 0$ case. The temperature dependent equations can be derived following the same scheme. In the Hamiltonian (B.1) the creation and annihilation operators have to be replaced by the temperature dependent ones. For completeness, the generalized particle number and gap equation are given here:

$$n = \frac{1}{2} \sum_k \left(1 - \frac{\epsilon_k - \mu}{E_k} \tanh\left(\frac{\beta}{2} E_k\right) \right) \, , \tag{B.19}$$

and

$$\frac{2}{\Delta} = g_0 \sum_k \frac{\Delta}{E_k} \tanh\left(\frac{\beta}{2} E_k\right) \, , \tag{B.20}$$

where g_0 is called the pairing strength.

B.2 Derivatives of the BCS Equations

The particle number equation in BCS formalism and the gap equation are numerically solved by a two dimensional Newton-Raphson iteration procedure. Therefore, the partial derivatives of both functions with respect to the two independent variables μ and Δ are needed.

It is convenient to write the BCS equations in the following form:

$$\tilde{g} = \frac{g_0}{2} \sum_k \frac{\Delta}{E_k} \tanh\left(\frac{\beta}{2} E_k\right) - \Delta \tag{B.21}$$

$$\tilde{n} = \frac{1}{2} \sum_k 1 - \frac{\epsilon_k - \mu}{E_k} \tanh\left(\frac{\beta}{2} E_k\right) - n \tag{B.22}$$

where

$$E_k = \sqrt{(\epsilon_k - \mu)^2 + \Delta^2} \, .$$

Then we obtain the following derivatives.

$\partial_\mu \tilde{g}$:

$$
\begin{aligned}
\frac{\partial \tilde{g}}{\partial \mu} &= \frac{g_0}{2} \sum_k \Delta \partial_\mu \frac{1}{E_k} \tanh\left(\frac{\beta}{2} E_k\right) + \frac{\Delta}{E_k} \partial_\mu \tanh\left(\frac{\beta}{2} E_k\right) \\
&= \frac{g_0}{2} \sum_k \Delta \left(-\frac{1}{E_k^2} \partial_\mu E_k\right) \tanh\left(\frac{\beta}{2} E_k\right) + \frac{\Delta}{E_k} \mathrm{sech}^2\left(\frac{\beta}{2} E_k\right) \frac{\beta}{2} \partial_\mu E_k \\
\frac{\partial \tilde{g}}{\partial \mu} &= \frac{g_0}{2} \sum_k \frac{\Delta}{E_k^3} (\epsilon_k - \mu) \tanh\left(\frac{\beta}{2} E_k\right) - \frac{\Delta}{E_k^2} (\epsilon_k - \mu) \frac{\beta}{2} \mathrm{sech}^2\left(\frac{\beta}{2} E_k\right)
\end{aligned}
$$

$\partial_\Delta \tilde{g}$:

$$
\begin{aligned}
\frac{\partial \tilde{g}}{\partial \Delta} &= \frac{g_0}{2} \sum_k \partial_\Delta \left(\frac{\Delta}{E_k}\right) \tanh\left(\frac{\beta}{2} E_k\right) + \frac{\Delta}{E_k} \partial_\Delta \tanh\left(\frac{\beta}{2} E_k\right) - 1 \\
&= \frac{g_0}{2} \sum_k \frac{E_k - (\partial_\Delta E_k)\Delta}{E_k^2} \tanh\left(\frac{\beta}{2} E_k\right) + \frac{\Delta}{E_k} \mathrm{sech}^2\left(\frac{\beta}{2} E_k\right) \frac{\beta}{2} \partial_\Delta E_k - 1 \\
\frac{\partial \tilde{g}}{\partial \Delta} &= \frac{g_0}{2} \sum_k \left(\frac{1}{E_k} - \frac{\Delta^2}{E_k^3}\right) \tanh\left(\frac{\beta}{2} E_k\right) + \left(\frac{\Delta}{E_k}\right)^2 \frac{\beta}{2} \mathrm{sech}^2\left(\frac{\beta}{2} E_k\right) - 1
\end{aligned}
$$

$\partial_\mu \tilde{n}$:

$$
\begin{aligned}
\frac{\partial \tilde{n}}{\partial \mu} &= \frac{1}{2} \sum_k -\left(\partial_\mu \left(\frac{\epsilon_k - \mu}{E_k}\right) \tanh\left(\frac{\beta}{2} E_k\right) + \frac{\epsilon_k - \mu}{E_k} \partial_\Delta \tanh\left(\frac{\beta}{2} E_k\right)\right) \\
&= \frac{1}{2} \sum_k -\left(\frac{E_k^2 - (\epsilon_k - \mu)^2}{E_k^3} \tanh\left(\frac{\beta}{2} E_k\right) + \frac{\epsilon_k - \mu}{E_k} \mathrm{sech}^2\left(\frac{\beta}{2} E_k\right) \frac{\beta}{2} \partial_\mu E_k\right) \\
\frac{\partial \tilde{n}}{\partial \mu} &= \frac{1}{2} \sum_k \frac{E_k^2 - (\epsilon_k - \mu)^2}{E_k^3} \tanh\left(\frac{\beta}{2} E_k\right) + \left(\frac{\epsilon_k - \mu}{E_k}\right)^2 \frac{\beta}{2} \mathrm{sech}^2\left(\frac{\beta}{2} E_k\right)
\end{aligned}
$$

$\partial_\Delta \tilde{n}$:

$$
\begin{aligned}
\frac{\partial \tilde{n}}{\partial \Delta} &= \frac{1}{2} \sum_k -\left((\epsilon_k - \mu)\left(\partial_\Delta \frac{1}{E_k}\right) \tanh\left(\frac{\beta}{2} E_k\right) + \left(\frac{\epsilon_k - \mu}{E_k}\right) \partial_\Delta \tanh\left(\frac{\beta}{2} E_k\right)\right) \\
&= \frac{1}{2} \sum_k -\left((\epsilon_k - \mu)(-\frac{1}{E_k^2} \partial_\Delta E_k) \tanh\left(\frac{\beta}{2} E_k\right) + \left(\frac{\epsilon_k - \mu}{E_k}\right) \mathrm{sech}^2\left(\frac{\beta}{2} E_k\right) \frac{\beta}{2} \partial_\Delta E_k\right) \\
\frac{\partial \tilde{n}}{\partial \Delta} &= \frac{1}{2} \sum_k \frac{(\epsilon_k - \mu)\Delta}{E_k^3} \tanh\left(\frac{\beta}{2} E_k\right) - \frac{(\epsilon_k - \mu)\Delta}{E_k^2} \frac{\beta}{2} \mathrm{sech}^2\left(\frac{\beta}{2} E_k\right)
\end{aligned}
$$

Bibliography

[ABF03]   Y. Alhassid, G. F. Bertsch, and L. Fang. Nuclear level statistics: Extending the shell model theory to higher temperatures. *Phys. Rev. C*, 68:44322, 2003.

[ABLN00]   Y. Alhassid, G. F. Bertsch, S. Liu, and H. Nakada. Parity dependence of nuclear level densities. *Phys. Rev. Lett.*, 84:4313, 2000.

[ADK$^+$94]   Y. Alhassid, D. J. Dean, S. E. Koonin, G. Lang, and W. E. Ormand. Practical solution to the monte carlo sign problem: Realistic calculations of ^{54}fe. *Phys. Rev. Lett.*, 72:613, 1994.

[AG89]   E. Anders and N. Grevesse. Abundances of the elements - Meteoritic and solar. *Geochim. Cosmochmim Acta*, 53:197–214, January 1989.

[AP95]   Y. Aboussir and M. Pearsson. *Atomic Data Nuclear Data Tables*, 61:127, 1995.

[ASTQ04]   D. Argast, M. Samland, F. K. Thielemann, and Y. Z. Qian. *A&A*, 416:997, 2004.

[BBFH57]   E. M. Burbidge, G. R. Burbidge, W. A. Fowler, and F. Hoyle. Synthesis of the Elements in Stars. *Rev. Mod. Phys.*, 29:547–650, 1957.

[BCS57]   J. Bardeen, L. N. Cooper, and J. R. Schrieffer. Theory of superconductivity. *Phys. Rev. Lett.*, 108(1175), 1957.

[Bet36]   H. A. Bethe. An attempt to calculate the number of energy levels of a heavy nucleus. *Phys. Rev.*, 50:332, 1936.

[BM69]   A. Bohr and B. R. Mottelson. *Nuclear Structure Vol. I.* W. A. Benjamin, Inc. , 1969.

[Bur01]   A. Burrows. *Progress in Particle and Nuclear Physics*, 46:59, 2001.

[BW85]   H. H. Bethe and J. R. Wilson. *ApJ*, 14:23, 1985.

[CHB01]   R. Cayrel, V. Hill, and T. Beers. *Nature*, 409:691, 2001.

[CTT87]   J. J. Cowan, F. K. Thielemann, and J. W. Truran. *ApJ*, 323:543, 1987.

[CTT91]   J. J. Cowan, F. K. Thielemann, and J. W. Truran. *Phys. Rep.*, 208:267, 1991.

[CW66]   S. A. Colgate and R. H. White. *ApJ*, 626:681, 1966.

[DKL+95]   D. J. Dean, S. E. Koonin, K. H. Langanke, P. B. Radha, and Y. Alhassid. Shell-model monte carlo studies of fp-shell nuclei. *Phys. Rev. Lett.*, 74:2909, 1995.

[DPPS69]   J. Damgaard, H. C. Pauli, V. V. Pashkevic, and V. M. Sturinski. A method for solving the independent-particle schrdinger equation with a deformed average field. *Nucl. Phys. A*, 135:432, 1969.

[Far05]   K. Farouqi. PhD thesis, Univerity of Mainz, 2005.

[FM95]   G. M. Fuller and B. S. Meyer. Neutrino Capture and Supernova Nucleosynthesis. 453:792–809, November 1995.

[FRR+99]   C. Freiburghaus, J.-F. Rembges, T. Rauscher, E. Kolbe, F.-K. Thielemann, K.-L. Kratz, B. Pfeiffer, and J. J. Cowan. The Astrophysical r-Process: A Comparison of Calculations following Adiabatic Expansion with Classical Calculations Based on Neutron Densities and Temperatures. *ApJ*, 516:381–398, May 1999.

[FRT99]   C. Freiburghaus, S. Rosswog, and F. K. Thielemann. *ApJ*, 525:L121, 1999.

[GC65]   A. Gilbert and A. G. W. Cameron. A composite nuclear level density formula with shell corrections. *Can. Journal of Physics*, 43:1446–1496, 1965.

[GS91]   J. J. Gaimard and K. H. Schmidt. *Nucl. Phys. A*, 531:709, 1991.

[HKT76]   W. Hillebrandt, T. Kodama, and K. Takahashi. R-process nucleosynthesis - A dynamical model. *ApJ*, 52:63–68, October 1976.

[HM80]   W. M. Howard and P. Moeller. *ADNDT*, 25:219, 1980.

[HT99]   W. R. Hix and F. K. Thielemann. *J. Comput. Appl. Math.*, 109:321, 1999.

[HWQ97]   R. D. Hoffman, S. E. Woosley, and Y. Z. Qian. *ApJ*, 951:962, 1997.

[IIS79]   A. V. Ignatyuk, K. K. Istekov, and G. N. Smirenkin. *Sov. J. Nucl. Phys.*, 29:450, 1979.

[IOS89]   M. G. Itkis, V. N. Okolovich, and G. N. Smirenkin. *Nucl. Phys. A*, 502:243c, 1989.

[Isa02]   P. van Isacker. Exact level densities for the harmonic oscillator. *Phys. Rev. Lett.*, 89:26, 2002.

[KBT+93]   K. L. Kratz, J. P. Bitouzet, F. K. Thielemann, P. Moeller, and B. Pfeiffer. *ApJ*, 403:216, 1993.

[KLF04]   E. Kolbe, K. H. Langanke, and G. M. Fuller. *Phys. Rev. Lett.*, 92:111101, 2004.

[Kli52]   P. F. A. Klingenberg. *Rev. Mod. Phys.*, 24:63, 1952.

[Kra]   K. L. Kratz. private communication.

[KZK+05]   A. Kelic, N. Zinner, E. Kolbe, K. H. Langanke, and K. H. Schmidt. *Phys. Lett. B*, 616:48, 2005.

[LDRK96]   K. Langanke, D. J. Dean, P. B. Radha, and S. E. Koonin. Temperature dependence of pair correlations in nuclei in the iron region. *Nucl. Phys. A*, 602:244, 1996.

[LJKO93]   G. H. Lang, C. W Johnson, S. E. Koonin, and W. E. Ormand. Monte carlo evaluation of path integrals for the nuclear shell model. *Phys. Rev. C*, 48:1518, 1993.

[LMT+01]   M. Liebendörfer, A. Mezzacappa, F. K. Thielemann, O. E. Bronson Messer, W. R. Hix, and S. W. Bruenn. Probing the gravitational well: No supernova explosion in spherical symmetry with general relativistic Boltzmann neutrino transport. *Phys. Rev. D*, 63, 2001.

[LW70]   J. M. LeBlanc and J. R. Wilson. A Numerical Example of the Collapse of a Rotating Magnetized Star. *APJ*, 161:541–+, August 1970.

[May94]   T. Mayer-Kuckuk. *Kernphysik*, chapter 7. B. G. Teubner, 1994.

[Mey89]   B. S. Meyer. Decompression of initially cold neutron star matter - A mechanism for the r-process? *ApJ*, 343:254–276, August 1989.

[Mey95]   B. S. Meyer. *ApJL*, 449:55, 1995.

[MPK03]   P. Moeller, B. Pfeiffer, and K. L. Kratz. New calculations of gross
            β-decay properties for astrophysical applications: Speeding-up the
            classical r-process. *Phys. Rev. C*, 67:558027, 2003.

[MPRT00]   A. Mamdouh, J. M. Pearson, M. Rayet, and F. Tondeur. *Nucl.
            Phys. A*, 679:337, 2000.

[MS99]   W. D. Myers and W. J. Swiatecki. *Phys. Rev. C*, 60:014606–1, 1999.

[MZPC97]   G. Martinez-Pinedo, A. P. Zuker, A. Poves, and Courier.E. Full *pf*
            shell study of $a = 47$ and $a = 49$ nuclei. *Phys. Rev. C*, 55:187, 1997.

[NA97]   H. Nakada and Alhassid.Y. Total and parity-projected level densities
            of iron-region nuclei in the auxiliary fields monte carlo shell model.
            Phys. Rev. Lett., 79:2939, 1997.

[NFS$^+$93] R. Nojarov, A. Faessler, P. Sarriguren, E. Moya de Guerra, and
            M. Grigorescu. Orbital and spin m1 excitations in actinide nuclei.
            Nucl. Phys. A, 563:349, 1993.

[NVL97]   A. Novoselsky, M. Vallieres, and O. La'adan. Full *f-p* shell calcula-
            tion of ^{51}ca and ^{51}sc. *Phys. Rev. Lett.*, 79:4341, 1997.

[ORT02]   R. Oechslin, S. Rosswog, and F. K. Thielemann. *Phys. Rev. D*,
            65:3005, 2002.

[PFT01]   I. V. Panov, C. Freiburghaus, and F. K. Thielemann. *Nucl. Phys.
            A*, 688:587, 2001.

[PKP$^+$05] I. V. Panov, E. Kolbe, B. Pfeiffer, T. Rauscher, K. L. Kratz, and
            F. K. Thielemann. *Nucl. Phys. A*, 747:633, 2005.

[PTVF96]   W. H. Press, S. A. Teukolsky, W. T. Vetterling, and B. P. Flannery.
            Numerical Recipes in Fortran 90. Cambridge University Press, 1996.

[Qia02]   Y. Z. Qian. *Astr. J.*, 569:L103, 2002.

[QW96]   Y.-Z. Qian and S. E. Woosley. *ApJ*, 233:337, 1996.

[RT00]   T. Rauscher and F. K. Thielemann. *At. Data Nucl. Data Tables*,
            75:1, 2000.

[RT01]   T. Rauscher and F. K. Thielemann. *At. Data Nucl. Data Tables*,
            79:47, 2001.

[RTK97]   T. Rauscher, F. K. Thielemann, and K. L. Kratz. Nuclear level den-
            sity and the determination of thermonuclear rates for astrophysics.
            Phys. Rev. C, 56:1613, 1997.

[SCL]   C. Sneden, J. J. Cowan, and J. E. Lawler. The extremely metal-poor, neutron capture-rich star cs 22892-052: A comprehensive abundance analysis. *Astrophysical. J.*, 591:936.

[Sie86]   A. J. Sierk. *Phys. Rev. C*, 33:2039, 1986.

[SJ87]   Phillip J. Siemens and Aksel S. Jensen. *Elements of Nuclei*. Allan Wylde, 1987.

[SMNF93]   P. Sarriguren, E Moya de Guerra, R. Nojarov, and A. Faessler. M1 spin strength distribution in ^{154}sm. *J. Phys. G: Nucl. Part. Phys.*, 19:291, 1993.

[SS82]   E. Symbalisty and D. N. Schramm. Neutron star collisions and the r-process. *Astophyics Letters*, 22:143–145, 1982.

[Tam82]   G. A. Tamman. in supernavae: A study of current reaserach. page 371, 1982.

[TBM01]   T. A. Thompson, A. Burrows, and B. S. Meyer. *ApJ*, 562:887, 2001.

[TOPS79]   Y. Tanaka, Y. Oda, F. Petrovich, and R. K. Sheline. Effect of the spin-orbit potential on the single particle levels in the superheavy region. *Phys. Lett. B*, 83:279, 1979.

[TWJ94]   K. Takahashi, J. Witti, and H. Th. Janka. *A&A*, 842:858, 1994.

[WH92]   S. E. Woosley and R. D. Hoffman. *ApJ*, 202:239, 1992.

[WJT94]   J. Witti, H. Th. Janka, and K. Takahashi. *A&A*, 841:856, 1994.

[WKMO01]   S. Wanajo, T. Kajino, G. J. Mathews, and K. Otsuki. The r-Process in Neutrino-driven Winds from Nascent, "Compact" Neutron Stars of Core-Collapse Supernovae. *ApJ*, 554:578–586, June 2001.

[WWMH94]   S. E. Woosley, J. R. Wilson, G. J. Mathewes, and R. D. Hoffman. *ApJ*, 229:246, 1994.

[Zin]   N. Zinner. private communication.

[Zuk01]   A. P. Zuker. Binomial level densities. *Phys. Rev. C*, 64:21303, 2001.

Curriculum Vitae

Lebenslauf

Persönliche Daten

Name	Darko Mocelj
Adresse	Allschwilerstrasse 49 CH-4055 Basel Tel. +41 61 534 62 47 E-Mail darko@mocelj.net
Geburtsdatum	10.01.1977
Geburtsort	Rheinfelden / Baden (Deutschland)
Nationalität	deutsch
Familienstand	ledig

Studium

2001–2006	Doktoratsstudium an der Universität Basel Titel der Arbeit: Neutron- and neutrino-induced reactions: their physical description and influence on r-process calculations Betreuer: Prof. Dr. F. K. Thielemann und Prof. Dr. T. Rauscher
1996–2001	Studium der Physik, Mathematik und Astronomie an der Universität Basel, Basel Abschluss: Diplom in theoretischer Physik

Schulbildung

1993–1996   Technisches Gymnasium, Lörrach

1987–1993   Theodor Heuss Realschule, Lörrach

1983–1987   Grundschule, Hauingen

March 30, 2008

Folgenden DozenteInnen habe ich meine Ausbildung zu verdanken:

C. Bandle, G. Baur, B. Binggeli, C. Bruder, R. Buser, F. -J. Elmer, O. Gerhardt, K. Hencken, H. Kraft, E. Kolbe, D. Loss, D. Masser, E. Meyer, H. Mühry, G. R. Plattner, T. Rauscher, C. Schoenenberger, I. Sick, P. Talkner, A. Tamman, L. Tauscher, F. K. Thielemann, D. Trautmann, C. Ullrich.

Acknowledgments

thanks to the former and the current group members and the "4th floor members" for their support, friendship and kindly atmosphere during the last years. In particular I would like to thank Christian Freiburghaus, Stefan Rosswog, Roland Oechslin, Jacob Lund Fisker, Carla Froehlich, Ute Dreyer, Matthias Liebendoerfer, Tommy Rauscher, Kai Hencken, Dirk Trautmann, Gabriel Martinez-Pinedo and Friedel Thielemann.

A special thanks goes to Carla Froehlich, Ute Dreyer and Oliver Pfeiffer for the coffee break conversations which was an integral part of the daily routine.

I am particularly grateful to everybody who has read the manuscript of my thesis and corrected the English spelling and grammar. Special thanks to Carla Froehlich and Tommy Rauscher.

And last but not least I would like to thank my partner Katrin Lindenberger for her patience during the last weeks of my thesis and the continous support during the last years. I also would like to thank my parents for supporting me during my studies.

Basel   Darko Mocelj
April, 2006.